

AMERICAN UNIVERSITY OF BEIRUT

OPTIMIZATION OF THE PERFORMANCE OF A SOLAR
STILL ASSISTED BY A ROTATING DRUM WITH A ROUGH
SURFACE

by
MANAR FAWZI YOUNIS

A dissertation
submitted in partial fulfillment of the requirements
for the degree of Doctor of Philosophy
to the Department of Mechanical Engineering
of the Maroun Semaan Faculty of Engineering and Architecture
at the American University of Beirut

Beirut, Lebanon
March 2021

AMERICAN UNIVERSITY OF BEIRUT

OPTIMIZATION OF THE PERFORMANCE OF A SOLAR
STILL ASSISTED BY A ROTATING DRUM WITH A ROUGH
SURFACE

by
MANAR FAWZI YOUNIS

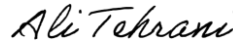
Approved by:



Dr. Mohammad N. Ahmad, Professor Advisor
Bahaa and Walid Bassatne Department of Chemical and Environmental Engineering,
AUB



Dr. Kamel Ghali, Professor Member of Committee
Department of Mechanical Engineering, AUB



Dr. Ali Tehrani, Associate Professor Member of Committee
Bahaa and Walid Bassatne Department of Chemical and Environmental Engineering,
AUB



Dr. Carine Habchi, Assistant Professor Member of Committee
Mechanical Engineering Department, AUB



Dr. Khalil El Khoury, Professor Member of Committee
Mechanical Engineering Department, Lebanese University



Dr. Ala'a H. Al Muhtaseb, Associate Professor Member of Committee
Department of Petroleum and Chemical Engineering, Sultan Qaboos University

Date of dissertation defense: March 26, 2021

AMERICAN UNIVERSITY OF BEIRUT

DISSERTATION RELEASE FORM

Student Name: _____ Younis _____ Manar _____ Fawzi _____
Last First Middle

I authorize the American University of Beirut, to: (a) reproduce hard or electronic copies of my dissertation; (b) include such copies in the archives and digital repositories of the University; and (c) make freely available such copies to third parties for research or educational purposes:

- As of the date of submission
- One year from the date of submission of my dissertation.
- Two years from the date of submission of my dissertation.
- Three years from the date of submission of my dissertation.

_____  _____ 07-04-2021 _____

Signature

Date

ACKNOWLEDGEMENTS

I would like to deeply thank my advisor, Professor Mohammad N. Ahmad, for his continual guidance throughout this research journey. I had the chance to benefit from his research experience and critical thinking. I would like also to thank the members of my dissertation committee Prof. Ali Tehrani, Prof. Khalil Houry, Prof. Alaa Al- Muhtaseb and Dr. Carine Habchi for their valuable comments and recommendations.

I also gratefully acknowledge the efforts and valuable intervention and feedback of my co- advisor Dr. Kamel Ghali. You really know that this work wouldn't have been accomplished without your guidance and interference from the very first day. No words can describe how grateful I am for giving me this opportunity to finish my PhD journey.

Dr. Carine, thanks a lot for every comment and observation you have put in this work. Your help is much appreciated and your feedback really widened my way of thinking scientifically.

I would like to thank Dr. Samir Mustapha for his cooperation in guidance in material selection and sandblasting process. The efforts of the faculty members and staff of the Mechanical Engineering Department at the American University of Beirut are much appreciated in achieving this work: Mr. Hisham Ghlayini, Mr. Ghassan Dib, Mr. Roger Souaid, Mr. Dori Rouhana and Mrs. Rita Khalil. Mr. Joseph Nassif's amazing efforts are highly appreciated throughout all the manufacturing and experimental phase of this research.

I would also like to express my cordial gratitude to my colleagues and friends who provided me with stimulating environment to achieve my goals: Mariam Itani, Carine Habchi, Nagham Ismail, Asma Jrad, Doaa Asaad, Safaa Khalil, Jinan Charara, Mohammad Hout, Racha Siblani, Ghadeer Awada, Mohammad Nasser, and Nicolas Aramouni.

Hussein Daoud, my dear friend, your help is really acknowledged and appreciated to the maximum. You did not hesitate to help me whenever you had the chance, and your contribution is not less than mine in this work, especially in the experimental part. I wish you nothing but the best.

At the end, I would like to express my appreciation to my big family. Mama, you were number one supporter for me in every little tiny step. I wouldn't have finished without your prayers and continuous help. You have always loved me unconditionally and your good examples have taught me to work hard for the things that I aspire to achieve. My dearest sister, Manoula, I owe you nothing but gratefulness and deep gratitude for your forever understanding and help in whatever I needed. My dad, thanks for everything. My parents in law, Uncle Imad and Tante Lina, your presence has always been a source of joy and encouragement. My bestie, Bisan, I hope you all the best. Your presence itself was a great support for me.

The last word goes to my loving husband.

This work is dedicated to you. Your efforts were not less than mine at all. You have been a constant source of support and encouragement during the challenges of graduate studies and life. I wouldn't have imagined this step without you. Your presence was the first and

final support for me. You were always there and always supported me to finish this long journey together. You always stood by me when things got dark and discouraging. We have faced a lot together, but the best is yet to come, by your love, support and being around. My sweetest daughters, Lina and Maha, and, my coming baby boy Imad: everything I do is for you; to be proud of your mama and to be the best mom I can ever be. You were my companions in this journey. You were patient and handled well, you were the most amazing daughters one can ever have. Thanks a lot and I hope that one day, you be better than your mama...

ABSTRACT

OF THE DISSERTATION OF

Manar Fawzi Younis for Doctor of Philosophy
Major: Mechanical Engineering

Title: Optimization of the Performance of a Solar Still Assisted by a Rotating Drum with a Rough Surface

Solar still desalination system is a passive technology used to convert saline water into a fresh one. This technology is characterized by its simplicity and low cost, however it has low water yields. In this study, a rough surface rotating drum is integrated within the conventional solar still system to enhance its productivity. A mathematical model is developed to predict the water film thickness created around the rotating drum and to calculate the daily water yield of the still system taking into consideration the roughness effect. In addition, experiments were conducted in order to validate the developed model. Good agreement was obtained between the modeled and experimental results, where the maximum error obtained was less than 10%, validating the ability of the model in capturing the physics behind the operation of a solar still. Also, it was found that upon increasing the roughness ratio from 1 in the case of smooth surface to 2.2 in the case of rough surface, an enhancement of 78% was obtained in terms of the water yield production. On the other hand, an enhancement of 198% was obtained when comparing a no drum system with a system with smooth surface, and 431.1% when comparing a no drum system to a solar still system with a rough drum.

A parametric study was conducted to investigate the main factors affecting the system's performance, where it was found that the increase in roughness ratio and practical radius to length ratio leads to an increase in the productivity of the system. Furthermore, the speed of rotation and the contact angle between the drum and water should be optimized for enhanced performance. A significant increase in the optimal angular speed is observed for contact angles higher than 150°. Finally, it was found that for the same contact angle, higher the radius to length ratio is, lower the optimal angular speed, which will consequently save energy.

TABLE OF CONTENTS

ACKNOWLEDGEMENTS	1
ABSTRACT	3
ILLUSTRATIONS	6
TABLES	9
ABBREVIATIONS	10
Chapter	
I. ENHANCED SOLAR STILL DESALINATION SYSTEMS ..	12
A. Introduction	12
B. Solar stills: principle and state of the art	13
C. Further enhancement of solar stills	16
D. Objectives	34
II. SIMPLIFIED MODELING AND MATHEMATICAL FORMULATION	35
A. Thermal Modeling of the Solar Still.....	35
1. Heat and Mass Transfer Phenomena	35
2. General Energy Balance Equations	37
3. Modeling of Heat Flows	38
4. Summary of the Model.....	42
B. Roughness Modeling	44
1. Modeling of the Rough Surface	45
2. Pressure Gradient Due to Roughness	46
C. Driven Flow Rate Calculation	47

1. Flow zones.....	47
2. Momentum equations	49
3. Film Thickness over the Drum and Flow Rate Calculation	51
D. Design Parameters	56
III. EXPERIMENTAL PROCEDURE	60
A. Experimental Set Up	60
B. Methods for the Creation of Uniformly Rough Surfaces	66
C. Roughening Process	67
D. Measurement Apparatus and Data Acquisition.....	71
IV. VALIDATION OF THE SIMPLIFIED MODEL	76
A. Validation with Literature	76
B. Validation with Experiments.....	79
C. Uncertainty Analysis	86
V. PARAMETRIC STUDY	90
A. Effect of Surface Roughness	90
B. Effect of Angular Speed	93
C. Effect of Contact Angle.....	96
D. Effect of Drum's Radius to Length Ratio	99
VI. OPTIMIZATION OF THE DESIGN PARAMETERS.....	103
VII. CONCLUSION.....	108
BIBLIOGRAPHY	111

ILLUSTRATIONS

Figure

1. Conventional single slope solar still	14
2. Modified solar still set- up (a) Front view (b) 2D view	15
3. Basin solar still with internal and external reflectors (19).....	16
4. Basin-type still with a double-slope glass roof (16)	18
5. Double effect active solar still coupled with a compound parabolic concentration (26)	19
6. Single effect solar still (20).....	19
7. Passive solar still with a separate condenser (23).....	20
8. Solar still coupled with external condenser (28)	21
9. Floating wick type solar still (55)	22
10. Weir type solar still (37)	23
11. Weir type cascade solar still (51).....	24
12. Vertical multiple effect diffusion solar still coupled with a reflector (39)	25
13. Solar still coupled with PCM (44)	27
14. Black granite utilization (52)	28
15. Solar still with Nano- fluids along with external condenser (53).....	28
16. Glass balls (6)	30
17. Enhanced solar still with rotating drum with (a) Triangular cover, (b) Circular cover, (c) Single sloped cover (14)	31
18. Heat and mass transfer phenomena	36
19. Roughness pattern with illustration of the fluid–air interface (14).....	45
20. Film thickness variation over the rotating drum (7)	48
21. Flowchart of solution methodology	59
22. De- assembled parts of the set up (a): Smooth drum with basin, (b) Basin, (c) Rough drums, (d): Triangular glass cover.....	62
23. Opening for shaft placement.....	63
24. (a) Inclined plexy channels with (b) Ball type valves	64
25. Motor used for shaft operation.....	64
26. Power supply used to maintain power needs	65

27. Final assembled set up	65
28. Sandblasting process equipment	67
29. Manual sand blasting process	68
30. Particle sand size.....	68
31. MIRA 3 TESKAN system	69
32. SEM images of the sand particles.....	69
33. DektakXT stylus profiler	70
34. B- Type stylus of 2 μm size	70
35. Settings of roughness measurement.....	71
36. Set ups under operation.....	73
37. Water droplets formed of the walls of the cover	73
38. Sensors used in the experiment; (a) Anemometer, (b) Pyranometer, (c): Infrared thermometer, (d) OM-EL-USB-2, (e) K-Type thermocouple, (f) OM- DaqPro data logger	75
39. Comparison of the model results with experimental results of Malaeb et al. (5): a) water temperature variation with time; b) solar still productivity with time..	79
40. Comparison of model and experimental results of: (a): glass, (b): drum, (c): water temperatures and (d) hourly productivity with time for a set up with a drum with smooth surface	82
41. Comparison of model and experimental results of: (a): glass, (b): drum, (c): water temperatures and (d) hourly productivity with time for a set up with a drum with rough surface	84
42. Comparison between no drum, smooth and rough systems productivity: (a): Model and (b): Experimental values	85
43. Variation with time of temperature difference between the drum and the glass cover for variable roughness ratios	91
44. Variation with time of water vapor pressure difference between the drum and the glass cover for variable roughness ratios	92
45. Variation with time of hourly productivity of the solar still for variable roughness ratios	92
46. Variation with time of total productivity of the solar still for variable roughness ratios	93

47. Variation with time of temperature difference between the drum and the glass cover for variable angular speeds	94
48. Variation with time of water vapor pressure difference between the drum and the glass cover for variable angular speeds	95
49. Variation with time of hourly productivity for variable angular speeds.....	95
50. Variation with time of total productivity for variable angular speeds	96
51. Variation with time of temperature difference between the drum and the glass cover for variable contact angles.....	97
52. Variation with time of water vapor difference between the drum and the glass cover for variable contact angles.....	98
53. Variation with time of hourly productivity for variable contact angles.	98
54. Variation with time of total productivity for variable contact angles.....	99
55. Variation with time of average drum temperature for variable drum's radius to length ratios.	101
56. Variation with time of temperature difference between the drum and the glass cover for variable drum's radius to length ratios.	101
57. Variation with time of hourly productivity for variable drum's radius to length ratios.....	102
58. Variation with time of total productivity for variable drum's radius to length ratios.....	102
59. Optimization of the angular speed (using the MADS algorithm which is a direct search optimization method) for different contact angles and different roughness ratios.....	105
60. Variation of productivity (computed from Equation 5) with contact angle for variable roughness ratios for optimal angular speed.....	105
61. Optimization of the angular speed (using the MADS algorithm which is a direct search optimization method)for variable contact angles for different radius to length ratios	106
62. Variation of productivity (computed from Equation 5) with contact angle for variable radius to length ratios for optimal angular speed	107

TABLES

Table

1. Numerical constants.....	57
2. Hourly variation of weather conditions	76
3. Sample calculation of error for a system with rough drum	77
4. Sample calculation of internal uncertainty	87
5. Accuracy, range and % error of equipment	89

ABBREVIATIONS

A	Evaporative surface area (m^2)
C_p	Specific heat (J/kg/K)
D	Diameter (m)
D_h	Hydraulic diameter (m)
F	View factor
h	Convective heat transfer coefficient
I	Intensity of solar radiation (W/m^2)
k	Thermal conductivity (W/m/K)
L	Characteristic length scale of convection (m)
p	Partial vapor pressure (N/m^2)
P	Pressure (N/m^2)
PV	Photovoltaic
Pr	Prandtl number
q	Heat transfer rate (W/m^2)
R	Radius (m)
Re	Reynolds's number
T	Temperature (K)
t_k	Thickness of the drum sheet (m)
t_f	Water film thickness (m)
V	Velocity of air (m/s)

Subscripts

a	Ambient
---	---------

b	Brine water
b ₁	Water on one side of the system
b ₂	Water on the other side of the system
c	Cover
d	Drum
f ₁	Fiberglass on one vertical side of the system
f ₂	Fiberglass on the other vertical side of the system
i	Inner
o	Outer

Greek Letters

α	Thermal diffusivity (m ² /s)
β	Numerical constant
l	Height of the cylinders (m)
γ	Contact angle
ε	Emissivity
μ	Dynamic viscosity (kg/m s)
ξ	Liquid – gas surface tension
ρ	Density
σ	Stephan-Boltzmann constant
σ_s	Surface tension
τ	Tangential stress at free surface
ϕ	Distance between cylinder edges (m)
Λ	Non- Dimensional variable

CHAPTER I

ENHANCED SOLAR STILL DESALINATION SYSTEMS

A. Introduction

Water is distributed on the earth as sea water and fresh water at percentages of 96.54% and 2.53%, respectively (1), and only 0.36% of the fresh water is directly available for people (2). The high population number accompanied by modern lifestyles, resulting in high energy consumption rates has caused further critical issues, such as environmental pollution and fuel shortages (3). In addition to human consumption, water is also needed for industrial and agricultural applications (4) especially in the arid areas which imposed a strong need to maintain new sources especially when water is not always offered in the appropriate quantity and quality when needed for specific purposes. Moreover, fossil fuel resources are fixed, non-renewable, and finite resources, and their use is a main contributor to global warming so that their consumption in fuel- based desalination systems leads to environmental pollution problems (5). Hence, the huge shortages of fossil fuel and energy resources have imposed a need to replace the finite expensive energy sources with free and renewable ones (4). Therefore, desalination systems are considered a promising method to obtain fresh water from the seas and oceans (6), so that this industry has been extensively growing (7). According to the 22nd GWI/ IDA Worldwide Desalting Plant Inventory, there are 14,451 desalination plants on-line and their global total capacity is close to 60 million m³/d (8) including also thermal technologies. Thermal technologies include Multi- Stage Flash (MSF), Multi- Effect Distillation (MED), Vapor Compression (VC), and membrane technologies include Microfiltration (MF), Ultrafiltration (UF), Nanofiltration (NF), and Reverse Osmosis (RO). Among them,

MSF, MED, and RO are commercially applied in large capacities in cities and always have high efficiencies based on electrical power consumption (9). However, these technologies are not suitable for remote villages, since electrical energy is rather scarce and any electrical facilities are hard to be applied. However, there is often plenty of solar energy. For example, Lebanon is geographically well situated to get benefit of the free solar energy, since there is a sunny period of 3,000 hours yearly, a yearly average solar radiation of 2,200 KWh/m² and a daily global sunny period of 4.8 KWh/m² (10), which makes it a very suitable place for solar energy utilization. Also, solar stills are easy and cheap to build and operate. Moreover, when there is a small population and fresh water requirement, as in the case of remote villages, water needs could be satisfied by solar stills, although their productivity is much lower than those of electricity-driven desalination technologies. In addition, considering that more and more photovoltaic and thermal plants are applied in these areas, it is likely for solar still to combine with photovoltaic & thermal (PV/T) systems (11) or concentrated solar power (CSP) plants. Therefore, for a rural area where fresh water is needed, and solar radiation is pretty available, solar stills are considered an appropriate solution for making use of free solar energy for water desalination purposes. In fact, solar stills were the first method used on a small scale to convert impure saline water to potable water (13).

B. Solar stills: principle and state of the art

Solar still is a device that mimics the natural hydrologic cycle to produce fresh water based on the sustainable and renewable solar energy (14). The conventional system consists mainly of a basin, where saline or brackish water is placed, and a transparent cover that allows the penetration of the sunlight and thus enhances the

evaporation process. The distillate is then collected to be used in different applications as shown in Figure 1.

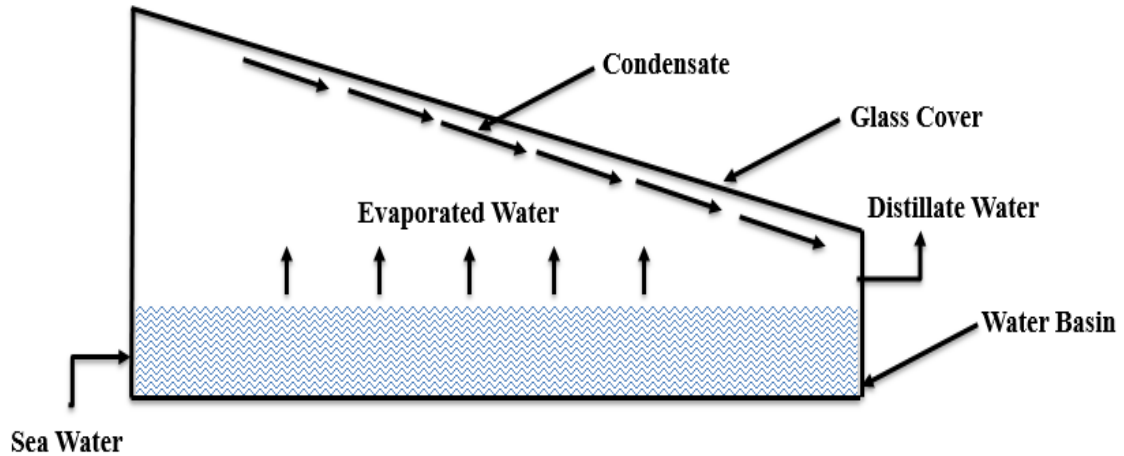
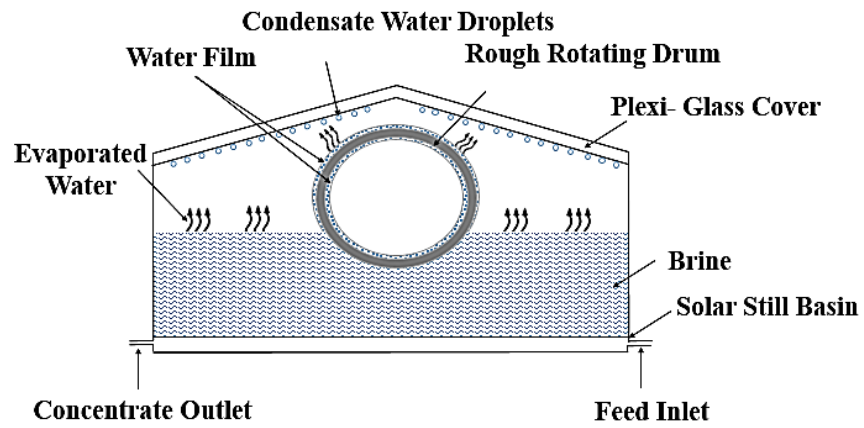


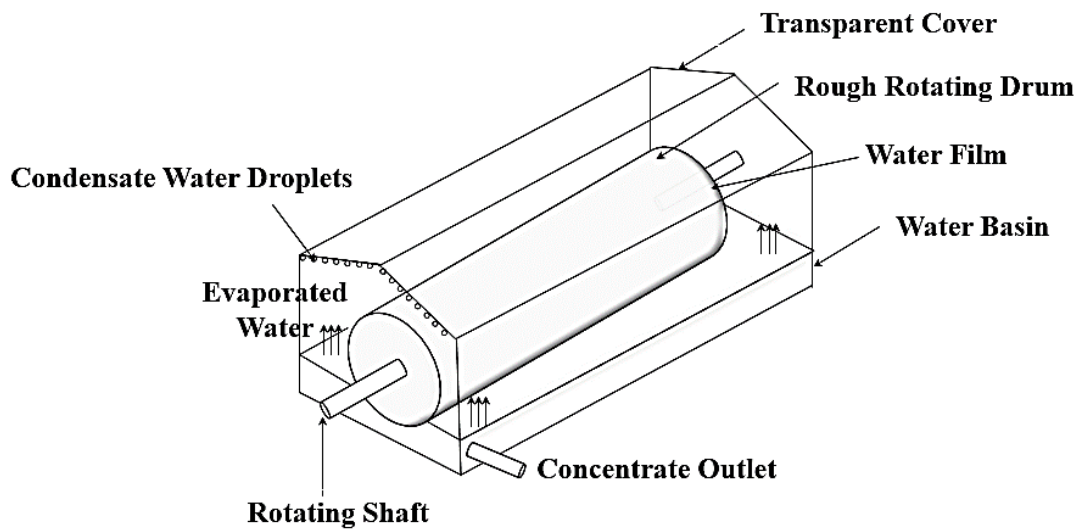
Figure 1: Conventional single slope solar still

However, solar stills are characterized by their low productivity compared to other conventional desalination techniques. This is related to the fact that the latent heat of condensation is rejected to the atmosphere and thus lost, and there is a difficulty in raising the evaporating temperature and decreasing the condensation temperature, since all the thermal processes (heating, evaporation, condensation) are taking place in one container (15). In this work, the proposed solar still device is mainly made of three parts: a water basin, a transparent glass cover and a rotating drum characterized by a rough surface as shown in Figure 2(a, b). The drum is connected to a shaft allowing its rotation and the formation of a thin water film around it. The cover transmits solar radiation to the water initiating the evaporation process followed by water condensation on the glass cover. An inlet supplies water to the still basin while outlets are used for distillate collection and brine discharge. The roughness of the drum presents a high

potential in enhancing the heat transfer process and increasing the solar still productivity.



(a)



(b)

Figure 2: Modified solar still set- up (a) Front view (b) 2D view

C. Further enhancement of solar stills

The first solar distillation device in the world was built in Chile with a total area of 4700 m², with multiple basic basin solar still units (2). From that time, extensive research has been carried out to enhance the productivity and water yield of the solar still systems, while maintaining economic feasibility and simplicity in design and operation. For example, external reflectors were used in many studies, such as in the work of Tanaka (16), where a basin still with internal and external reflectors was installed as shown in Figure (3). The system consisted of a basin liner with internal reflectors, a glass cover, and an external reflector, which caused an increase in the introduced solar radiation in the still, compared to a conventional still. Experimental results showed that there was an enhancement of about 70–100% in daily productivity (16), whereas theoretical results showed an increase of 48% in the daily productivity for the entire year (17). Tanaka et al. (18) also emphasized on the importance of the installation angle of the vertical external reflector, which should be optimized according to the season of operation to enhance the productivity all the year around.

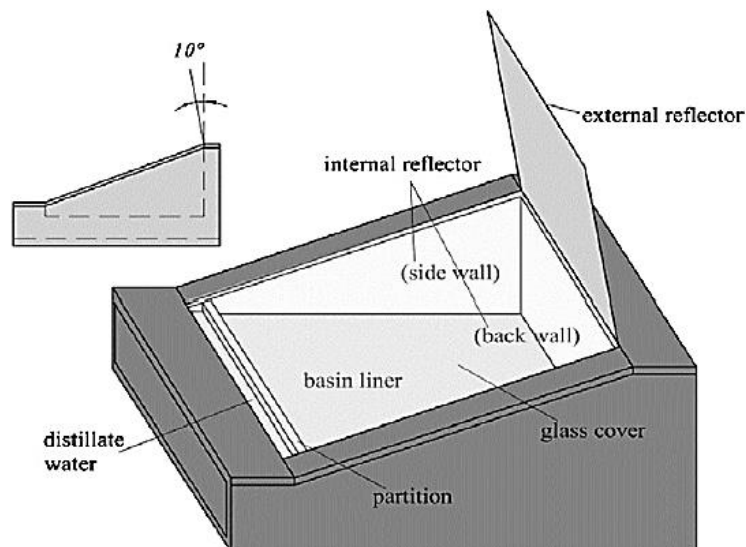


Figure 3: Basin solar still with internal and external reflectors (19)

Another study was conducted by Dev et al. (20), where results showed that the daily yields obtained from the basin solar still combined with a curved reflector were 6.3, 5.6 and 4.3 kg/m²/d at water depths 0.01, 0.02 and 0.03 m respectively. At same respective water depths, the daily yield obtained from the basin solar still were 2.1, 1.9, and 0.8 kg/m²/d respectively. This is directly related to the fact that internal reflectors are useful in concentrating solar radiation, which is very helpful when weak sunlight is available, or the local temperature is low, whereas external reflectors main role is to change the direction of solar beams to improve the flexibility of configuration of the absorber plate.

Moreover, some modifications were investigated regarding the cover shape and geometry. For example, in the work of Kabeel et al. (21), a comparative experimental analysis was conducted on different designs of solar stills. A standalone Conventional Solar Still (CSS), Inclined Solar Still (ISS) and Integrated Conventional and Inclined Solar Still (CSS-ISS) were experimented under different parameters that affect the fresh water yield, mainly the water depth and the mass flow rate of water in the solar still. The results showed that the fresh water yield from CSS-ISS, ISS, and CSS were 6.2, 5.04 and 4.24 kg respectively (21). In addition, in the work of Manokar et al. (22), the performance of two different designs was studied represented by an Inclined Solar Panel Basin (ISPB) still integrated with (active mode) and without (passive mode) Flat Plat Collector (FPC). Results showed that water yield production was 4.3 and 7.9 kg/day from the passive and active mode respectively.

Another major enhancement was introducing solar collectors along with the solatr still systems, where solar collectors introduce extra solar radiation into the solar still and increase the productivity. For example, in the work of Badran et al. (23), a

basin solar still coupled with a flat-plate solar collector was used, as shown in Figure(4), which consisted of a basin-type still with a double-slope glass roof, a conventional fin-tube flat-plate collector, a constant head tank and a feeding tank. The productivity of the modified still was found to be $2.3 \text{ kg/m}^2/\text{d}$ compared to a productivity of $1.5 \text{ kg/m}^2/\text{d}$ for a conventional still without solar collector.

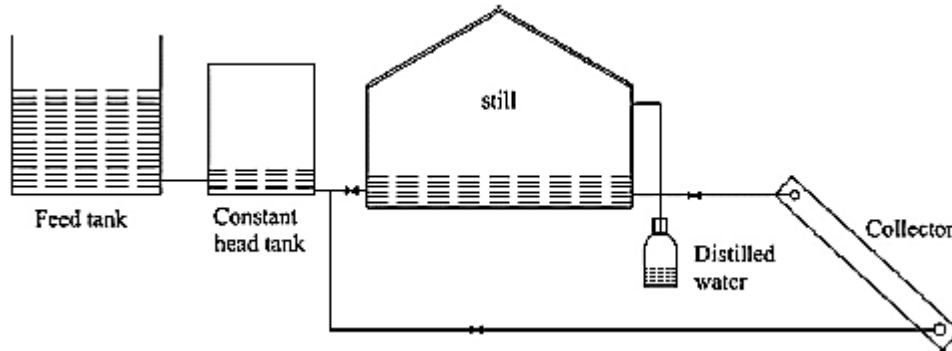


Figure 4: Basin-type still with a double-slope glass roof (16)

Also, Prasad and Tiwari (24) proposed a double effect active solar still coupled with a compound parabolic concentration (CPC) collector, as shown in Figure (5). This caused water in the still basin to be heated and evaporated, and the vapor condensed on the inner side of a glass cover. Thus, the latent heat was transferred to flowing water, and secondary vapor condensed on the inner side of the upper glass cover. It was also found that the brine temperature was much higher in the modified still compared to a conventional solar still.

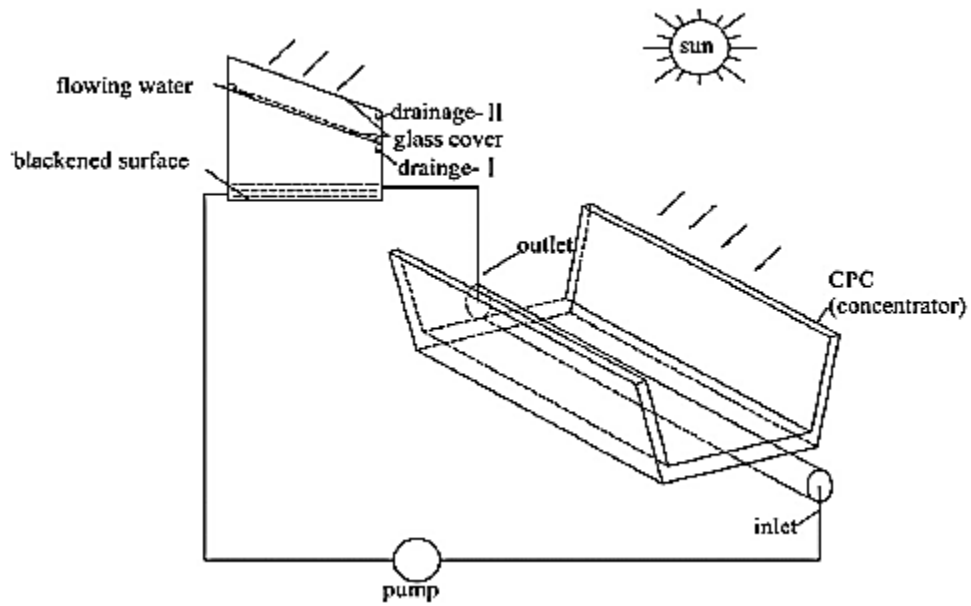


Figure 5: Double effect active solar still coupled with a compound parabolic concentration (26)

On the other hand, Voropoulos et al. (25) coupled a solar collector field with a solar still, in addition to a heat storage tank in order to prolong working time. The modified system is described in Figure (6), and composed of an asymmetric, single-effect solar still, an integrated storage tank and a flat-plate solar collector field. The enhanced system's water yield was approximately twice of that without a solar collector field.

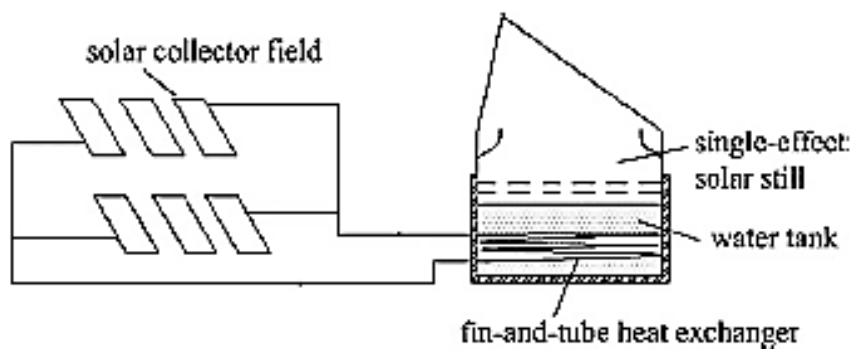


Figure 6: Single effect solar still (20)

In addition, many researches worked on enhancing condensation conditions to facilitate the evaporation of brine in the solar still system. For example, Madhlopa and Johnstone (27) investigated a passive solar still with a separate condenser as shown in Figure (7). Their system consisted of a horizontal basin (1) with an evaporator chamber (first effect), a basin (2) (second effect), a basin (3) (third effect), a condensing cover and an opaque insulation shield over the condensing cover. Theoretical results showed an enhancement of 62% in productivity compared with a conventional still.

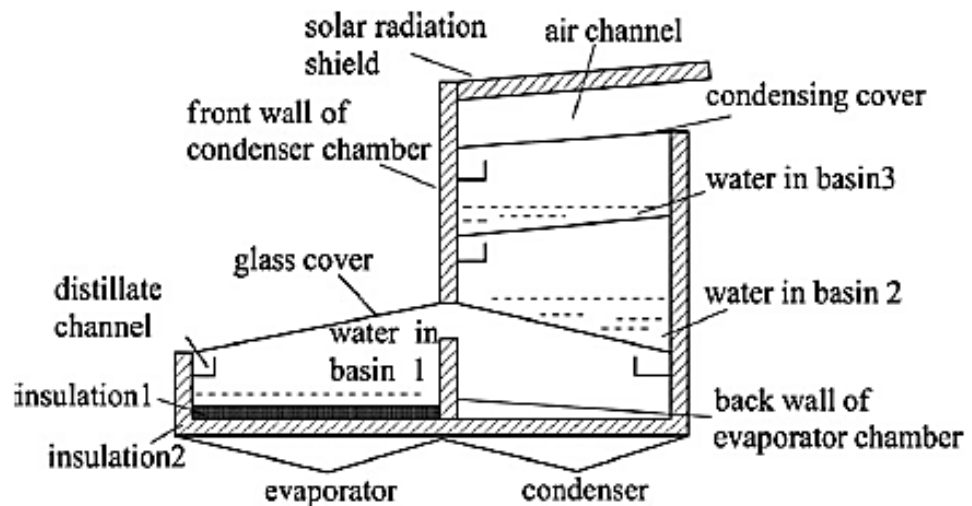


Figure 7: Passive solar still with a separate condenser (23)

E1-Bahi and Inan (28) studied a solar still coupled with an outside condenser, as shown in Figure (8). A stainless steel reflector was added to collect more solar radiation and to provide a shadow for the condenser, where productivity was found to be 7 kg/m²/d from June to August, which was confirmed by the findings of Kumar and Bai (29). It was also reported that a thinner glass cover (30) and condenser material with high conductivity (31) could enhance the productivity.

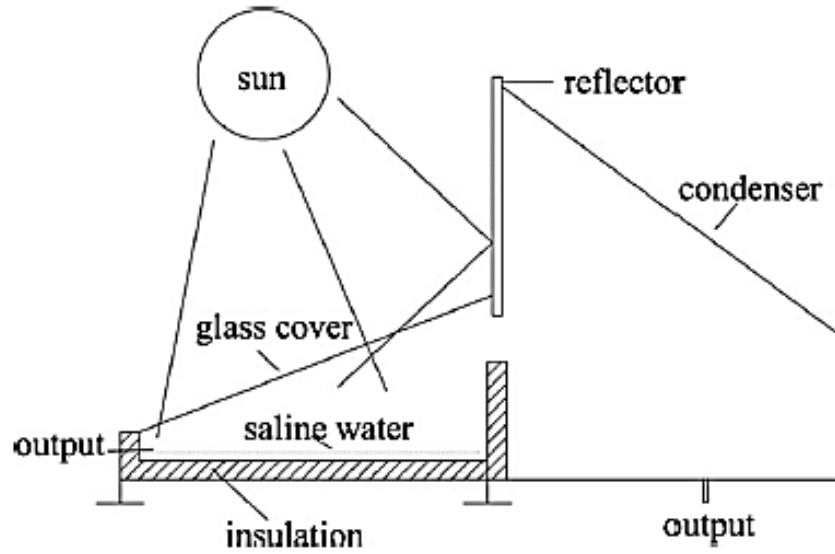


Figure 8: Solar still coupled with external condenser (28)

Bassam and Abu-Hijleh (32) and Rahim (33) on the other hand suggested that a properly designed condensation process of passing cooling water over the glass cover could increase the efficiency, whereas a poor design would likely lead to a significant drop in efficiency (32), which is due to the fact that the cooling water reduced solar radiation to the basin.

Other researchers studied the possibility of increasing the surface area. The productivity of a solar still increases with increase in absorber plate area (cover) and free surface area of water. Velmurugan et al. (34) enlarged the areas by integrating fins with the solar still and found that the average daily productivity increased by 30%. The productivity was increased by 58%, 67%, 69% or 70% in a fin type solar still with black rubber, sand, pebble or sponge immersed in brine, respectively (35). Bassam et al. (36) placed sponge cubes in a basin solar still to increase the brine free surface and the evaporation rate. Results showed an increase in distillate production up to 273% compared with the still without sponge cubes under the same conditions. Nafey et al.

(37) used a floating perforated black plate to maintain thin film evaporation, where productivity increased by 15% when the original brine depth was 3 cm. Janarthanan et al. (38) designed a floating tilted-wick type solar still, as shown in Figure (9), wherein the brine flowed slowly over an inclined surface, under the effect of gravity, paved with wicks in a thin layer. Due to the thin layer's small heat capacity, the brine evaporated quickly. Compared to a conventional solar still, less time was needed to get fresh water in a tilted wick type solar still, where productivity was increased by 16–50% (2).

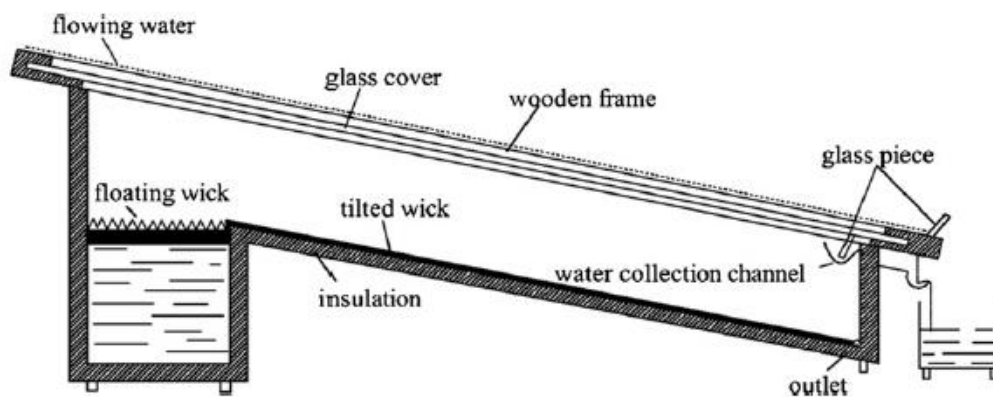


Figure 9: Floating wick type solar still (55)

Sadineni et al. (39) proposed a weir-type solar still, as shown in Figure (10). An inclined type solar still that was composed of a weir-shaped absorber plate, a condensing glass, a distillate collection trough and a water circulation system. Hot brine at the outlet was redirected into the still and mixed with feed brine to allow for an increase in the inlet temperature. For a single-pane glass cover, the average distillate productivity was 5.5 kg/m²/d during August and September, and it was approximately 20% higher than that of the conventional stills under the same conditions.

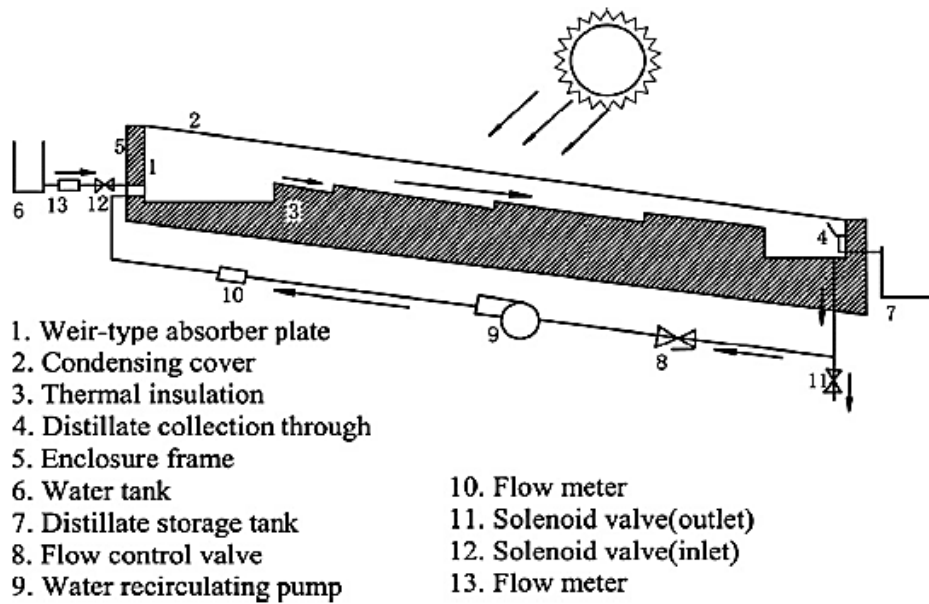


Figure 10: Weir type solar still (37)

Tabrizi et al. (40) investigated a weir-type cascade solar still, as shown in Figure (11), in which a 15-step absorber was covered by matte black paint. Each step was equipped with a weir 5 mm in height and 59 cm in length to force the flowing water to pass through the evaporation surface, which led to the increase of the residence time of the water in the still. A glass cover formed an enclosure space with a 2.5 cm air gap. Distilled water was guided to a collection channel, and the concentrated brine was discharged from the outlet. Their results showed a decrease in the daily productivity with an increase in feed water flow rate.

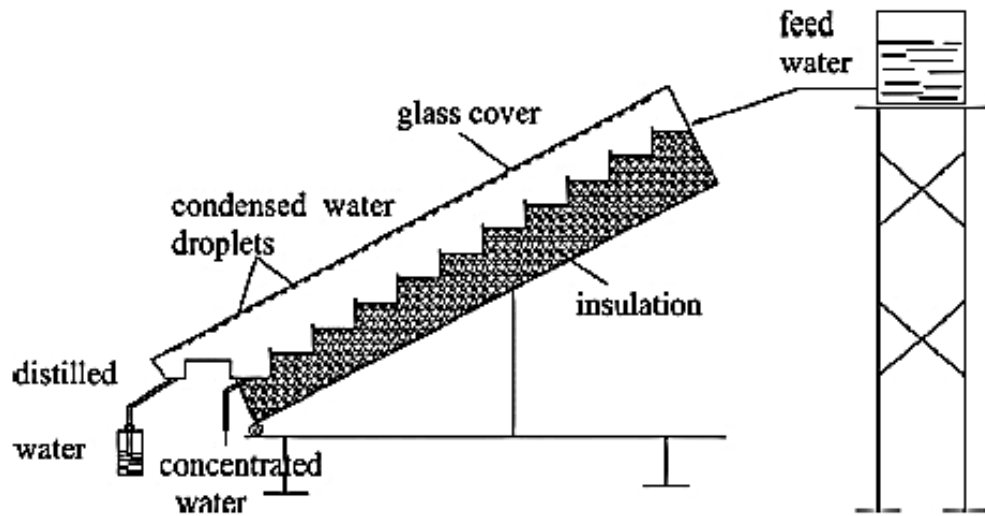


Figure 11: Weir type cascade solar still (51)

Regarding increasing free surface area, such as in the work of Bassam et al.'s (36), black sponge cubes with sponge-to-water volume ratio of 20% were recommended for a basin solar still, while the optimized size of a cube side differs with water depth in the basin. However, it was not recommended to increase free surface area by flowing brine because a lot of sensible heat would loss with hot brine being drained out (36). Moreover, recovering vapor latent heat can enhance both distillate productivity and thermal efficiency. Tanaka et al. (16) (41) investigated a multiple-effect solar still with a triangle cross-section, which consisted of a horizontal basin liner, a tilted double glass cover and vertical parallel partitions covering saline-soaked wicks. Their experimental results showed that a still with 5-mm diffusion gap between 11 partitions produced distillate at a rate of 14.8–18.7 kg/m²/d when incident solar radiation on the glass cover ranged from 20.9 to 22.4 MJ/m²/d and ambient air temperatures in the range of 19- 30 °C. In addition, Tanaka et al. (42) (43) proposed a vertical multiple- effect diffusion (VMED) solar still coupled with a heat-pipe solar collector. According to their

theoretical analysis, a productivity of 21.8 kg/m²/d was attained under a daily cumulative solar radiation of 22.4 MJ/m². Another VMED structure that was studied outdoors is shown in Figure (12) (44).

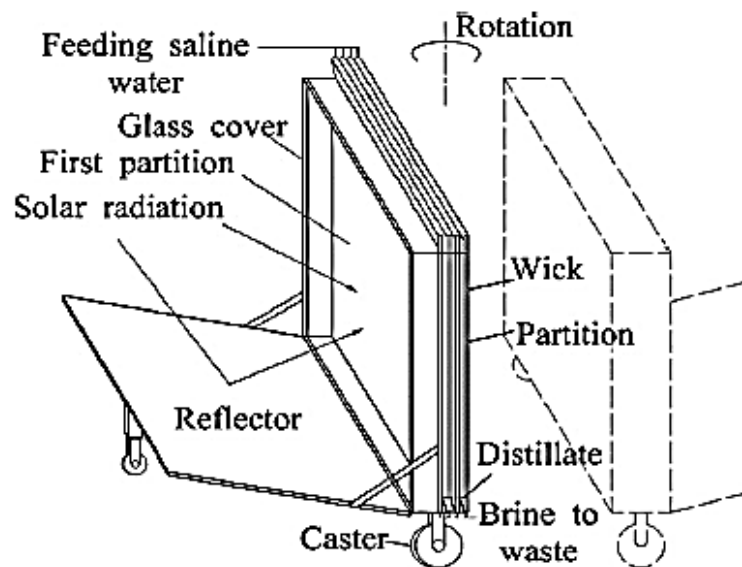


Figure 12: Vertical multiple effect diffusion solar still coupled with a reflector (39)

The maximum productivity was 13.4 kg/m²/d for a still with six effects and 5 mm diffusion gaps when the global solar radiation on the horizontal surface and on the glass cover ranged from 13.4 to 15.7 MJ/m²/d and from 20.2 to 22.9 MJ/m²/d, respectively. Among the mentioned stills, the VMED type still had the highest productivity experimentally because it had a high efficiency of heat recovery. The distance between two neighboring effects should be carefully designed. If they are too close, brine will easily mix with distilled water, while if they are too far, low efficiency will be obtained.

In the other hand, in the work of Al- Hinai et al. (45), a single effect and a double effect solar stills' productivity was assessed using mathematical modeling under

different climatic, design and operational parameters in Oman. The average annual productivity varied between 4.15 and 6 kg/m²/day for single and double effect solar stills respectively, with savings of about 15.7 % in the total cost. Schwarzer et al. (46), however, investigated a system employing a solar collector and a six-stage desalination tower with heat recovery. The hot brine in the first stage transferred energy by evaporation, radiation, and convection to the second stage and also lost some energy to the environment. The energy transferred from the first stage heated up the brine in the second stage, and the heat recovery process was repeated until the sixth stage. The last stage did not produce fresh water and was used as the salty water inlet to the unit. The total productivity was the sum of the productivity of the first five stages. According to the theoretical simulation results, the system had a production rate of 25 kg/m²/d, which was five times greater than that of the basin type solar desalination unit. The disadvantage of such system is the higher installation and operating costs compared to the conventional unit.

Solar stills may also be coupled with heat storage, due to the fact that solar energy is intermittent in nature, and its intensity depends on the hour of the day and local weather conditions, so maximum benefit should be taken from it. One of the solutions to utilize fluctuating solar energy on a continuous basis is to incorporate heat storage systems (47). Tabrizi and Sharak (48) investigated a basin solar still integrated with a sandy heat reservoir. In a 14-h test, the productivity was 3 kg/m², while that of a conventional basin solar still was 1.7 kg/m². El-Sebaai et al. (49) investigated a single basin solar still coupled with a phase change material (PCM) storage, as shown in Figure (13).

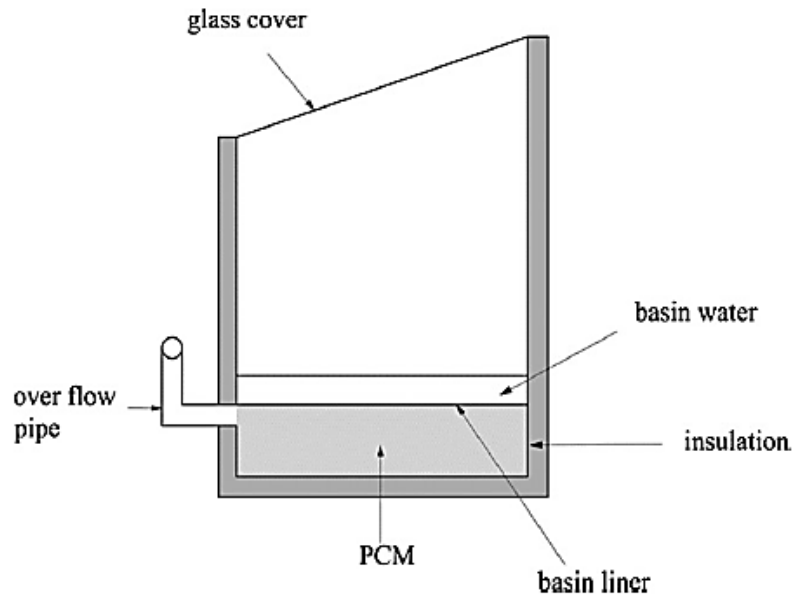


Figure 13: Solar still coupled with PCM (44)

A considerable amount of heat would be stored in the PCM during sunshine hours. After sunset, the PCM acted as a heat source for the basin water to evaporate. In addition, the temperature difference between brine and glass cover became greater because the ambient temperature of night was lower than that of daylight. The productivity of the system increased from $5 \text{ kg/m}^2/\text{d}$ to $9 \text{ kg/m}^2/\text{d}$ on sunny summer days. In addition, El-Sebaili et al. (50) studied a single-slope basin solar still integrated with a shallow solar pond (SSP) and found that the average productivity and thermal efficiency were higher than those obtained without the SSP by 52.4% and 43.8%, respectively, over a year. Black granite gravel was used in the basin by Sakthivel and Shanmugasundaram (52), as shown in Figure (14) where an increase of 17-20 % in water yield was observed.

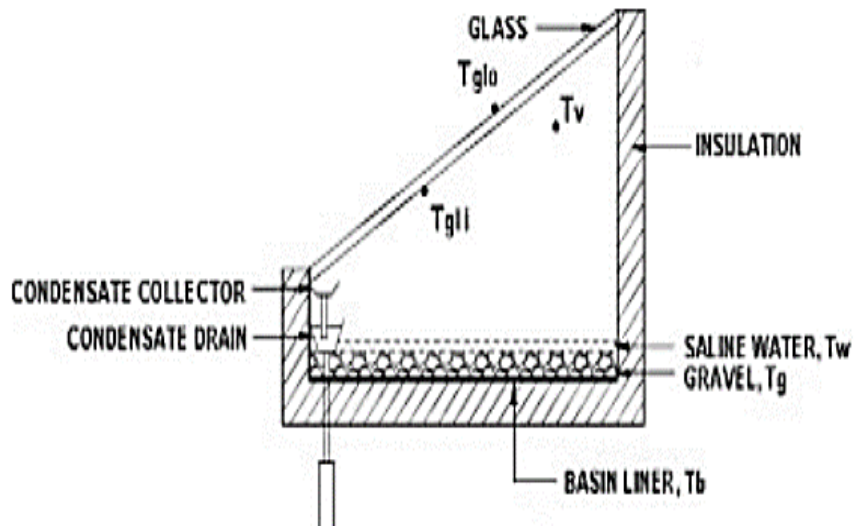


Figure 14: Black granite utilization (52)

Another method for enhancing the productivity was experimental attempts by using Nano fluids and integrating the still basin with an external condenser as shown in Figure (15) (53).

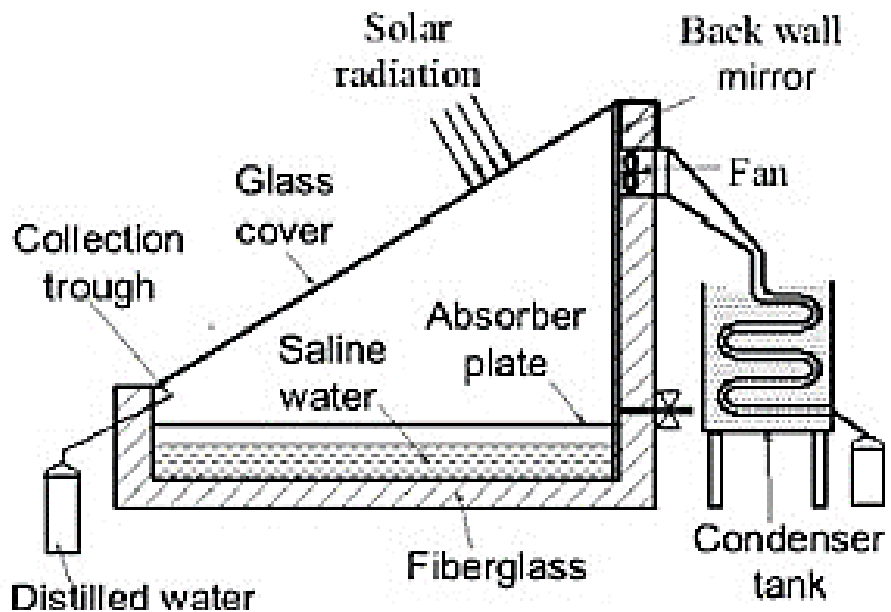


Figure 15: Solar still with Nano- fluids along with external condenser (53).

Results showed that integrating the solar still with external condenser increased the distillate water yield by about 53.2%, whereas the use of Nano fluids improved the solar still water productivity by about 116% (53).

Wick materials were also found to increase the water yield, where the wick basin type solar still studied by Velmurugan et al (34) integrated with fins in the basin of the still presented higher production rate. Also, for the purpose of increasing the exposure area, sponges were used. Results were compared experimentally and numerically, where 29.6% increase in productivity was observed when wick type solar still was used, 15.3% increase in productivity was noticed when sponges were used and 45.5% increase was noticed when fins were used (34).

Murugavel et al. (54) reported that a single basin double slope solar still with energy storing materials like quartzite rock, red brick pieces, cement concrete pieces, washed stones and iron scraps was able to store the excess energy and to increase the night time production. This is related to that heat storage prolongs the working time overnight, which will increase the total productivity. It is recommended in practical application although the installation and operating costs would increase a little. Among the materials used in their experiments, 3/4 in. sized quartzite rock was the most effective one, obtaining a productivity of 2.1 kg/m²/d with an enhancement of 6.2% compared to still with same amount of water, without any energy storing material. Finally, in the work of Abdel- Rehim and Lasheen (6), two modifications were made to the conventional solar still. First, a packed layer consisting of glass balls was installed in the bottom of the basin as shown in Figure (16) to increase the efficiency of the still by increasing the thermal storage of the system. Second, a rotating shaft was installed near the basin water surface. The results of their work showed that the efficiency of the

modified solar desalination system using the packed layer was increased from 2.5 to 7.5 % depending on the month of operation, while it was increased from 2.5 to 5.5 % when using a rotating shaft along with a PV-system.

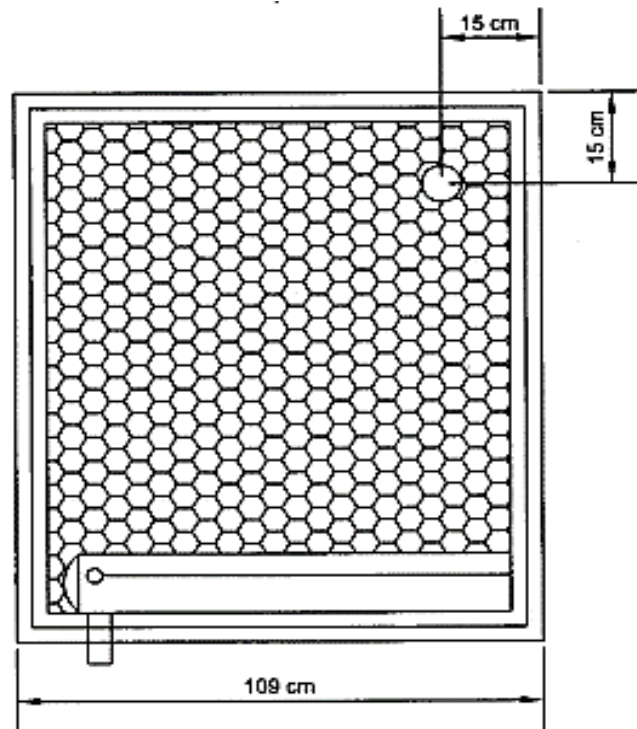


Figure 16: Glass balls (6)

Based on what was previously mentioned, it was noticed that most of the enhancement techniques did not increase the solar still productivity beyond 100% except when using the Nano fluids. On the other hand, the work of Malaeb et al. (14) introduced a simple yet very effective method for a notable enhancement in the water yield of a solar still. A lightweight, black-finished, slowly rotating aluminum drum was integrated within the still as shown in Figures (17(a, b, c)), which leads to the formation of a thin water film around the drum that evaporates rapidly.

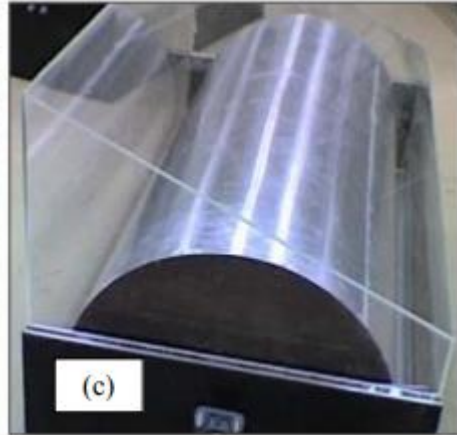
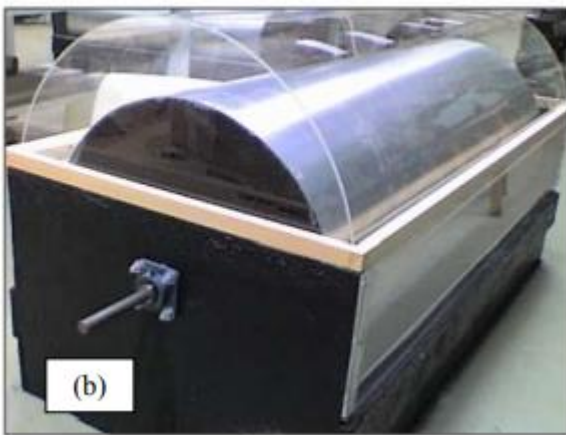
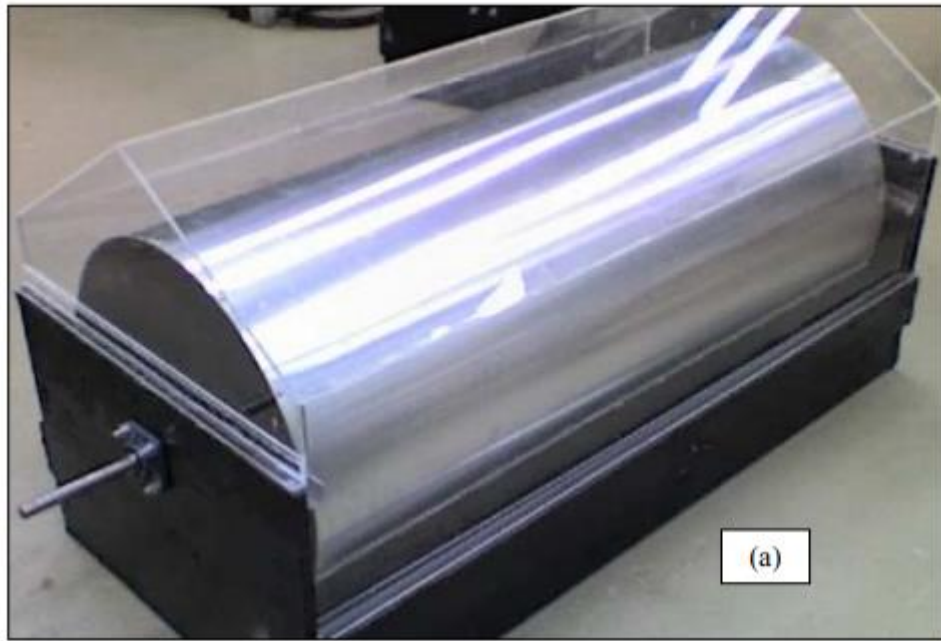


Figure 17: Enhanced solar still with rotating drum with (a) Triangular cover, (b) Circular cover, (c) Single sloped cover (14)

This modification notably increased productivity, where the average percent improvement varied between 200 and 300% compared to a conventional solar still without the drum under different operating and design conditions, while maintaining the advantages of using the solar still such as ease of handling, low-tech requirements, material availability, safe water quality, sustainability and space conservation (56) (57).

Moreover, this design allowed overcoming the problem of salt and algae formation in addition to stagnation issues, since the growth of algae and other particles on the surface of the brine and in the basin generally reduces heat transfer to the brine (58). This was solved in the modified still, since the introduced drum constantly renewed the evaporating water film and shattered the brine surface layer, thereby preventing the shielding layer that normally develops in conventional stills (57). On average, solar stills without a rotating drum yield 1.1 l/day/m^2 , whereas solar stills with rotating drums yield around 3.5 l/day/m^2 (14). However, Malaeb et al. (14) only studied the performance of rotating drums with smooth surfaces.

The performance of Malaeb et al. (14) system can be enhanced further. For instance, rough surfaces and corrugations, defined as surface structures that may present in some geometries, enhanced the heat transfer process in several heat exchange applications. In fact, rough elements cause disturbances on the surface, resulting in disturbances in the boundary layer and thus turbulence will take place at lower Reynolds's numbers increasing the heat transfer rate (59). In addition, the surface area of the rough drum will significantly increase compared to a smooth one, so the heat transfer rate will increase too, and the area on which the water film will be formed on will also augment leading to higher expected total water yield. For this reason, it is important to understand the physics behind the effect of roughness on the behavior of the spreading of the fluid above the rough surface. In the work of Dragila et al. (60), a fluid dragged into roughness by capillarity was studied, using an analytical diffusion-type law that describes and quantifies the physics behind driving fluid invasion into roughness. When balancing capillary, fluid and surface frictional resistive forces, results indicated that a hydraulic diameter approach can be used because of its simplicity in

representing complex shapes taking into consideration the free surface's shape. Another study by Andelman et al. (61) was designed to study the effect of surface roughness on the formation of thin films using X-ray diffraction and Ellipsometry. Also, in the work of Malijevsky et al. (62) roughness was extensively studied to investigate its effect on the wetting properties of hydrophilic substrates taking into consideration that any surface is found to be rough in real life. Results showed that microscopic surface corrugations increase the wetting temperature and makes the surface hydrophobic. Moreover, in the work of Zwol et al. (63) capillary forces were studied due to their important role in the micro- and Nano- electromechanical systems. In their study, it was found that at very low relative humidity values ($2 \pm 1\%$), capillary forces were still present largely, taking into consideration that their study was done under ambient conditions. Furthermore, in the work of Du et al. (64), a new empirical correlation was suggested for the film thickness formation of free falling water on a large-scale ellipsoidal surface, while constantly varying the inclined and extend angle and considering the inlet water temperature is equal to the ambient temperature.

Surface roughness is also well known for enhancing the effects of hydrophobic or hydrophilic behavior, as well as allowing for faster spreading of a hydrophilic fluid (65). Therefore, surface roughness can increase the driven flow rate by drum rotation hence it is expected to improve the solar still productivity. In the work of Hay et al. (65), the authors studied the spreading rate of a liquid, knowing its properties and the geometry of the surface roughness. Since roughness is considered as a difficult and random nature to understand, many assumptions were introduced to model its effect, mainly that a rough surface can be modeled by repetitive rough elements creating a curved liquid-air boundary resulting from capillarity (65). Capillarity may be defined as

the ability of a liquid to flow in narrow spaces without the assist of outside forces like gravity. It arises due to the intermolecular forces between the liquid and the nearby solid surfaces. At very small scales, where gravity is not considered, capillarity can be the reason for driving fluid movement (8). Therefore, using a rotating drum with rough surface presents a high potential in enhancing the performance of the system proposed by Malaeb et al. (14) by improving thermal performance, and creating a driving potential for fluid motion (20, 21).

D. Objectives

The objectives of this study are mainly to increase the solar still system productivity while maintain economic feasibility and simplicity in design. Roughness of the surface of the drum plays an important role in this process. Therefore, a model was developed to account for the effect of roughness on the formation of the film thickness over the rotating drum. The developed simplified model should predict the driven flow rate by the rotating drum and account for heat and mass transfer between the different components of the solar system through heat and mass balance equations computing temperatures of the system components and water evaporation rates. Experiments were conducted for validation of the simplified model. The validated model was used to conduct a parametric study investigating the main factors affecting the solar still productivity, where the design parameters were optimized for best performance.

CHAPTER II

SIMPLIFIED MODELING AND MATHEMATICAL FORMULATION

A simplified model is developed to study the performance of a solar still assisted by a rotating drum characterised by a rough surface. The model accounts for the roughness effect on improving performance through increasing drum exposed area to heat and mass transfer, and creating a driving potential for fluid motion. Heat and mass transfer between the different components of the solar system should be considered. A set of heat and mass balance equations are solved to compute temperatures of the system components and water evaporation rates. However, these equations require as input the driven flow rate by the rotating drum including the effect of surface roughness and the variation of film thickness over the drum. This can be done by solving the Navier- Stokes equations in the region where water is driven out of the basin by the rotating drum and considering the main forces driving the flow motion. The following section represents the governing equations of the model. It includes all the heat balance equations for the cover, the basin and the rotating drum, in addition to the modeling of the drum surface roughness' effect.

A. Thermal Modeling of the Solar Still

1. Heat and Mass Transfer Phenomena

Figure (18) represents the different heat exchange processes that take place in the solar still set up with a rough rotating drum. The cover part is mainly affected by the incident solar radiation, which represents the main factor that initiates the heat exchange

process in the entire system. Part of this radiation is absorbed by the glass cover, and the other part is transmitted through the glass. It then affects the brine water in the bottom of the setup which initiates the evaporation process, and evaporation from the drum surface is also initiated as it rotates and water film is formed. Meanwhile, heat exchange also occurs between the brine and the cover which stimulates the condensation process on the inclined walls of the cover and the vertical walls of the set up. Convective heat transfer occurs between the brine and the drum, and the drum and the cover of the solar still. Also, part of the heat is absorbed by the brine water at the bottom of the set up. At the same time, part of the solar radiation is incident on the rotating drum, which enhances evaporation and radiation between drum and the cover. Convection also occurs between the drum and the air inside its hole, and finally conduction takes place between the elements of the drum itself as shown in Figure (18).

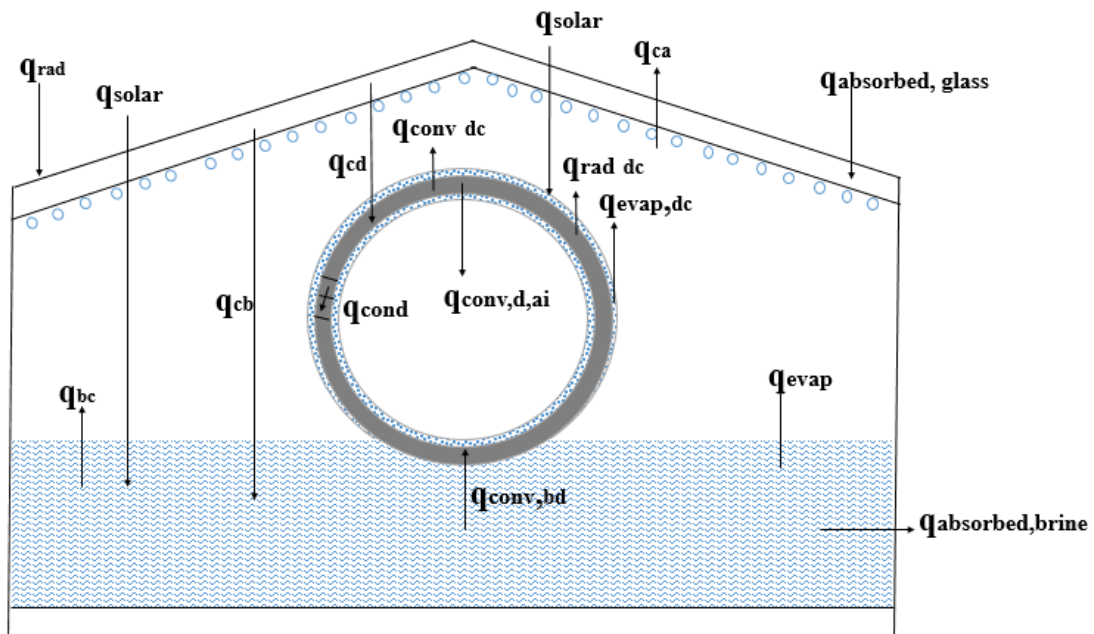


Figure 18: Heat and mass transfer phenomena

2. General Energy Balance Equations

The cover of the still is considered as one single part including the upper curved part and the two vertical sides, whereas the drum is discretized to get the temperature at each element of it. The heat balance for the still cover, denoted as symbol c , can be written as in Equation (1):

$$m_c C_{p_c} \frac{dT_c}{dt} = q_{rad} A_c - q_{cd} A_{cd} - q_{cb} A_{cb} - q_{ca} A_{ca} \quad (1)$$

Where m_c refers to the mass of the cover, C_{p_c} the heat capacity of the cover, T_c the cover temperature, q_{rad} is the radiative heat transfer, A_c the cover area, q_{cd} the heat transfer between the cover and the drum (denoted as symbol d), A_{cd} the area of the cover that interacts with the drum, q_{cb} the heat transfer between the brine water surface and the cover, A_{cb} the exposed area of the brine water surface i.e. excluding the brine diameter, q_{ca} the heat transfer between the cover and the ambient, and A_{ca} the area of the cover exposed to the ambient as shown in the Figure (18).

The transient energy equation for a drum element outside the water basin is given by Equation (2.a):

$$\frac{d}{dt} (m_d C_{p_d} T + m_b C_{p_b} T) = \frac{(q_{cond_x} - q_{cond_{x+\Delta x}})}{\Delta x} + q_{solar} - q_{conv_{dc}} - q_{rad_{dc}} - q_{evap_{dc}} - q_{conv_{dai}} \quad (2.a)$$

For a drum element just coming into/leaving the water in the basin, the heat balance equation is written as follows in Equation (2.b):

$$\rho_d t k_d C_{pd} \frac{T_{di2} - T_{di1}}{dt} = q_{solar} + q_{conv_{bd}} - \frac{(q_{cond_x} - q_{cond_{x+\Delta x}})}{\Delta x} + \frac{(q_{conv_x} - q_{conv_{x+\Delta x}})}{\Delta x} \quad (2.b)$$

For the water in the basin, the heat balance equation can be written as in Equation (3):

$$\frac{d}{dt} [m_b C_{pb} T] = q_{solar} A_{bc} - q_{bc} A_{bc} - q_{conv_{bd}} \quad (3)$$

3. Modeling of Heat Flows

The radiative heat transfer is defined as in Equation (4):

$$q_{rad} = \alpha_c I A_c \quad (4)$$

Where α_c is the cover absorptivity and I is the solar radiation.

The heat transfer q_{cd} between the cover and each element i of the n drum elements of width dx and length L_d each is given by Equation (5):

$$q_{cd} = \sum_{i=1}^n dx h_{cd} (T_{di} - T_{ci}) L_d \quad (5)$$

Where h_{cd} is the heat transfer coefficient between the cover and the drum.

The heat transfer q_{cb} between the cover and the brine water surface (denoted as symbol b) that is of width S_b on each side of the drum is given by Equation (6):

$$q_{cb} = h_{cb} (T_c - T_b) A_{cb} = h_{cb} (T_c - T_b) (2S_b L) \quad (6)$$

Where h_{cb} is the heat transfer coefficient between the cover and the water, T_b is the brine water temperature and L the length of the basin.

The heat transfer q_{ca} between the cover and ambient (denoted as symbol a) is given by Equation (7):

$$q_{ca} = h_{ca}(T_c - T_a)A_g = h_{ca}(T_c - T_a)(2S_cL) \quad (7)$$

Where h_{ca} is the heat transfer between the cover and the ambient is, T_a is the ambient temperature, and S_c is the length of the vertical side of the cover.

The heat transfer coefficient h_{ca} is the summation of the radiation (h_{rad}) and convection terms between the still cover and the ambient as shown in Equations (8) and (9), which were developed by Dunkle (66) who proposed a group of complete set of heat and mass transfer correlations based on a modified Grashof number, and used by Duffie and Beckman (67) and Wattmuf et al. (68).

$$h_{rad} = \varepsilon\sigma(T_c^2 + T_{sky}^2)(T_c + T_{sky}) \quad (8)$$

$$h_{ca} = 2.8 + 3v \quad \text{when } v \leq 5 \text{ m/s} \quad (9)$$

Where (9):

$$\varepsilon = \frac{1}{\varepsilon_b} + \frac{1}{\varepsilon_c} - 1 \quad (10)$$

$$T_{sky} = 0.0552T_a^4 \quad (11)$$

where σ is the Stephan-Boltzmann constant, T_{sky} is the sky temperature, v is the wind speed, ε_b and ε_c are the emissivity of water and glass cover.

The heat transfer coefficient between the still cover and the water in the basin (h_{cb}) is the summation of the radiation, evaporation and convection terms as following in Equation (12):

$$h_{cb} = h_{rad_{cb}} + h_{evap_{cb}} + h_{conv_{cb}} \quad (12)$$

The radiation term between water and cover is given by (66) Equation (13):

$$h_{rad_{cb}} = \varepsilon\sigma(T_c^2 + T_b^2)(T_c + T_b) \quad (13)$$

The evaporation and convection terms are given by (66) Equation (14) and (15) respectively:

$$h_{evap_{cb}} = 0.016273h_{conv_{cb}}(p_c - p_b) \quad (14)$$

$$h_{conv_{cb}} = 0.884 \left[(T_c - T_b) + \frac{(p_c - p_b)T_c}{268.9 \times 10^3 - p_c} \right]^{\frac{1}{3}} \quad (15)$$

Where p_c and p_b represent the partial vapor pressure at condensation and evaporation surface temperatures respectively.

The total heat transfer coefficient between the drum and cover (h_{dc}) is the summation of the individual coefficients representing radiation, evaporation and convection as in Equation (16):

$$h_{dc} = h_{rad_{dc}} + h_{evap_{dc}} + h_{conv_{dc}} \quad (16)$$

The radiation term between the drum element and the cover ($h_{rad_{dc}}$) is given by Equation (17):

$$h_{rad_{dc}} = \varepsilon\sigma(T_c^2 + T_{di}^2)(T_c + T_{di}) \quad (17)$$

The evaporation term ($h_{evap_{dc}}$) is given by (66) Equation (18):

$$h_{evap_{dc}} = 0.016273h_{conv_{cdi}}(p_c - p_{cdi}) \quad (18)$$

The convection term ($h_{conv_{cb}}$) is given by (66) Equation (19):

$$h_{conv_{cb}} = 0.884 \left[(T_c - T_{di}) + \frac{(p_c - p_{di})T_c}{268.9 \times 10^3 - p_c} \right]^{\frac{1}{3}} \quad (19)$$

In addition to the above equations, the heat transfer $q_{conv_{dai}}$ has to be included in order to account for the convection between the drum surface and the air inside the hollow drum, which is at temperature T_{ai} . This term is given by Equation (20):

$$h_{conv_{dai}} = 0.884 \left[(T_{ai} - T_{di}) + \frac{(p_{ai} - p_{di})T_{ai}}{268.9 \times 10^3 - p_{ai}} \right]^{\frac{1}{3}} \quad (20)$$

Regarding the radiative heat transfer between the surfaces, the view factor (F) should be taken into consideration. It is defined as the fraction of radiation that is leaving surface i and intercepted by surface j. The involved surfaces in calculating their view factors are: cover (c); drum (d); water on one side of the system (b1); water on the other side of the system (b2); fiberglass on one vertical side of the system (f1) and fiberglass on the other vertical side of the system (f2). Using the summation rule, the view factors of the different parts of the system can be related as the following in Equations (21-26):

$$\text{Glass Cover: } F_{cc} + F_{cd} + F_{cf1} + F_{cf2} + F_{cb1} + F_{cb2} = 1 \quad (21)$$

$$\text{Drum: } F_{dc} + F_{dd} + F_{df1} + F_{df2} + F_{db1} + F_{db2} = 1 \quad (22)$$

$$\text{Fiberglass side 1: } F_{f1c} + F_{f1d} + F_{f1f1} + F_{f1f2} + F_{f1b1} + F_{f1b2} = 1 \quad (23)$$

$$\text{Fiberglass side 2: } F_{f2c} + F_{f2d} + F_{f2f1} + F_{f2f2} + F_{f2b1} + F_{f2b2} = 1 \quad (24)$$

$$\text{Water surface 1: } F_{b1c} + F_{b1d} + F_{b1f1} + F_{b1f2} + F_{b1b1} + F_{b1b2} = 1 \quad (25)$$

$$\text{Water surface 2: } F_{b2c} + F_{b2d} + F_{b2f1} + F_{b2f2} + F_{b2b1} + F_{b2b2} = 1 \quad (26)$$

$$\text{By inspection: } F_{dd} = F_{f1f1} = F_{f1f2} = F_{f2f1} = F_{f2f2} = F_{b1b1} = F_{b1b2} = F_{b2b1} = F_{b2b2} = 0.$$

In order to obtain the view factor between the water and the still cover, the total view factor (F_{bc_total}) of one side of the system is obtained. The still cover is divided into 2 parts: cover 1, which is the upper part of the cover and cover 2, which is the vertical side of the cover.

The total view factor F_{bc_total} is the sum of view factors for the water-system side and water-glass1 (g1): $F_{bf_total} = F_{bf} + F_{bg2}$.

F_{bf} is calculated from (68), whereby $X = 1.5$, $Y = 0.035$ and $Z_{bf} = 0.12$, which gives: $F_{bf} = 0.45$.

Similarly, $F_{bf_total} = 0.48$ is found using $Z_{bf_total} = 0.42$. Therefore, $F_{bg2} = 0.03$.

4. Summary of the Model

By substituting the terms defined in the previous section in Equation (1) we get the energy balance equation of the cover:

$$\left[\rho_c (\pi r_c + 2S_c) t k_c L C_{pc} \frac{T_{g2} - T_{g1}}{dt} \right] = \alpha_c I_1 (2S_c L) + \alpha_c I_2 (2S_c L) + h_{bc} (T_b - T_{c2}) (2S_b L) - h_{ba} (T_{c2} - T_a) (2S_c) L + \sum_{i=1}^n dx h_{cd} (T_{di} - T_{c1}) L_d \quad (27)$$

The left hand side term (LHS) of Equation (27) represents the cover thermal storage, the first term of the right hand side (RHS) accounts for solar absorption by the inclined sides of the cover, the second term of the RHS considers solar absorption by the vertical sides of the cover, the third and fourth terms of the RHS models heat exchange between the cover and the brine and ambient air respectively. The last term of the RHS computes heat transfer between the cover and the different drum elements.

By substituting the terms defined in the previous section in Equation (2.a) we get the energy balance equation for a drum element outside the water:

$$\left[\rho_d t k_d C_{pd} \frac{T_{di2} - T_{di1}}{dt} + \rho_b t k_{b1} C_{pb} \frac{T_{di2} - T_{di1}}{dt} + \rho_b T_{di1} C_{pb} \frac{t k_{b2} - t k_{b1}}{dt} \right] = r \varepsilon_c \alpha_d I - r h_{dc} (T_{di1} - T_c) - r h_{conv_{dai}} (T_{di1} - T_{ai}) - k_d dx \frac{T_{di1} - T_{dibefore}}{t k_d} - k_d dx \frac{T_{di1} - T_{diafter}}{t k_d} - k_b dx \frac{T_{di1} - T_{dibefore}}{t k_{b1}} - k_b dx \frac{T_{di1} - T_{diafter}}{t k_{b1}} + \rho_d C_{pd} U T_{d(i-1)} \frac{dx}{t k_d} - \rho_d C_{pd} U T_{di} + \rho_b C_{pb} U T_{d(i-1)} \frac{dx}{t k_d} - \rho_b C_{pb} U T_{di} \frac{dx}{t k_d} \quad (28)$$

Where ε_c refers to the transmissivity of the cover, α_d the drum absorptivity, and k_d the drum conductivity.

The left hand side term (LHS) of Equation (28) represents the thermal storage term of the drum element and the thin water film on it, the first term of the right hand side (RHS) accounts for solar radiation absorption by the drum element, the second term of the RHS models heat exchange between the cover and the drum, the third term of the RHS considers the convective heat transfer between the air inside the hollow drum and the drum element surface, the fourth and fifth term of the RHS compute conduction between each drum element and the adjacent elements, the sixth and seventh term of the RHS compute conduction between brine elements, the eighth and the ninth terms of the RHS compute convection to and from each drum element, the tenth and the eleventh terms of the RHS compute convection to and from each brine element

By substituting the terms defined in the previous section in Equation (2.b) we get the energy balance equation for a drum element just coming into/ leaving the water:

$$\frac{d}{dt} [m_d C_{p_d} T] = h_{bd}(T_b - T_d) - k \frac{T_{d2} - T_{d_{before}}}{tk_d} - k \frac{T_{d2} - T_{d_{after}}}{tk_d} \quad (29)$$

Where h_{bd} is the convection heat transfer coefficient between the drum element and the water or:

$$\begin{aligned} & \rho_d t k_d C_{p_d} \frac{T_{di2} - T_{di1}}{dt} \\ & = r \varepsilon_c \varepsilon_w \alpha_d I + r h_{ab}(T_b - T_{di}) - k \frac{T_{di1} - T_{di_{before}}}{tk_d} - k \frac{T_{di1} - T_{di_{after}}}{tk_d} \\ & + \rho_d C_{p_d} U T_{d(i-1)} \frac{dx}{tk_d} - \rho_d C_{p_d} U T_{di} \frac{dx}{tk_d} \end{aligned} \quad (30)$$

The left hand side term (LHS) of Equation (30) represents the thermal storage term of the drum element, the first term of the right hand side (RHS) accounts for solar radiation absorption by the drum element, the second term of the RHS models heat

exchange between the brine water and the drum, the third and the fourth terms of the RHS compute conduction between each drum element and the adjacent elements, the fifth and the sixth terms of the RHS compute convection to and from each drum element or by substituting the terms defined in the previous section in Equation (3) we get the energy balance equation for water:

$$\rho_b H_b S_t L C_{pb} \frac{T_{b2} - T_{b1}}{dt} = \varepsilon_c \alpha_b I (2S_b L) - h_{bc} (T_b - T_{c1}) (2S_b L) - \sum_{i=1}^{n_i} r dx L h_{bd} (T_b - T_{di}) \quad (31)$$

Where H_b is the water basin height, S_t is the width of the brine water surface.

The left hand side term (LHS) of Equation (31) represents the thermal storage term of the water basin, the first term of the right hand side (RHS) accounts for solar radiation absorption by the water, the second term of the RHS models heat exchange between the brine water and the cover, the third term of the RHS computes heat exchange between the brine water and the drum.

In order to calculate the film thickness variation over the rough corrugated rotating drum, the work of Hay et al. (65) as well as White et al. (66) was integrated within the model as represented in the following section.

B. Roughness Modeling

A simplified model is developed to predict the combined effect of drum rotation, capillary effects and the additional surface roughness on the driven flow rate from the water basin. This model allows the calculation of the film thickness variation over the rotating drum.

1. Modeling of the Rough Surface

The rough surface is modeled as a surface with repetitive roughness elements. The roughness model considered under study is shown in Figure (19), which illustrates a flat plate on which rough elements are present. These elements are characterized by a cylindrical shape of uniform pattern (same height denoted by l), with an equal distance separating elements (denoted by d).

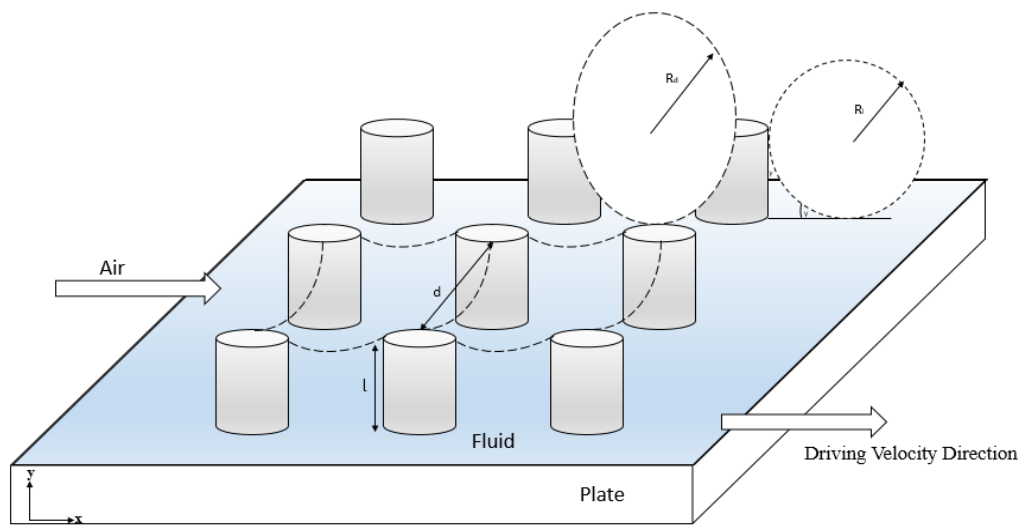


Figure 19: Roughness pattern with illustration of the fluid–air interface (14)

When considering rough surfaces, rough elements impose a driving flow potential through capillary effects in addition to capillary forces that are already present in case of a smooth surface to create a force balance at the air-fluid interface leading to the formation of a curved surface, affecting the water film flowing between the rough elements.

2. Pressure Gradient Due to Roughness

The calculation of pressure gradient created by the presence of the rough elements denoted by $\left(\frac{\partial P}{\partial x}\right)_{roughness}$, where P represents the pressure and x the coordinate of flow direction, was performed using the approach developed by Hay et al. (65).

In order to calculate the pressure difference created by the capillary forces resulting from the presence of rough elements, Young–Laplace equation was applied. As shown in Figure (19), the application of Young- Laplace equation strongly depends on the radii of curvatures R_l and R_d formed due to existence of the rough elements by capillarity effects. Therefore the moving fluid through the rough elements and their vertices will create these radii of curvatures which are calculated as shown in Equations (32):

$$R_l = \frac{l}{\cos \gamma - \sin \gamma} \quad (32.a)$$

$$R_d = \frac{d}{2\cos \gamma} \quad (32.b)$$

The liquid's pressure along the front decreases due to the curvature of the front edge of the scattering liquid. This creates a pressure difference between the liquid reservoir which is dragged due to the drum rotation, and the invasion front which initiates the invasion process. By modeling the surface roughness as cylindrical elements that are normal to the surface, the capillary pressure drop over a roughness pattern is given by Equation (33):

$$\Delta P = \sigma_s \left(\frac{1}{R_l} + \frac{1}{R_d} \right) \quad (33)$$

where ΔP is the pressure difference across the liquid–air interface triggered by capillarity, and σ_s is the liquid-gas surface tension. Substituting Equations (32) into Equation (33), and assuming that the pressure in the bulk macroscopic fluid is equal to the gas- phase pressure, then the pressure drop and the average pressure gradient across the repetitive roughness pattern is given by Equations (34.a-b) respectively:

$$\Delta P = \sigma_s \left(\frac{(2d+l) \cos \gamma - l \sin \gamma}{d_l} \right) \quad (34.a)$$

$$\left(\frac{\partial P}{\partial x} \right)_{roughness} = -\frac{\Delta P}{d} = -\sigma_s \left(\frac{(2d+l) \cos \gamma - l \sin \gamma}{d^2 l} \right) \quad (34.b)$$

C. Driven Flow Rate Calculation

1. Flow zones

In order to calculate the driven flow rate by rough drum rotation, an approach that divides the liquid film formation into three regions is followed. In each region the dominant forces are considered. It is first assumed that at the location at which the rotating cylinder leaves the water in the basin, the drum is approximated to be a flat surface withdrawn at the contact angle (γ) which is a reasonable assumption since the drum radius is not small as shown in Figure (20).

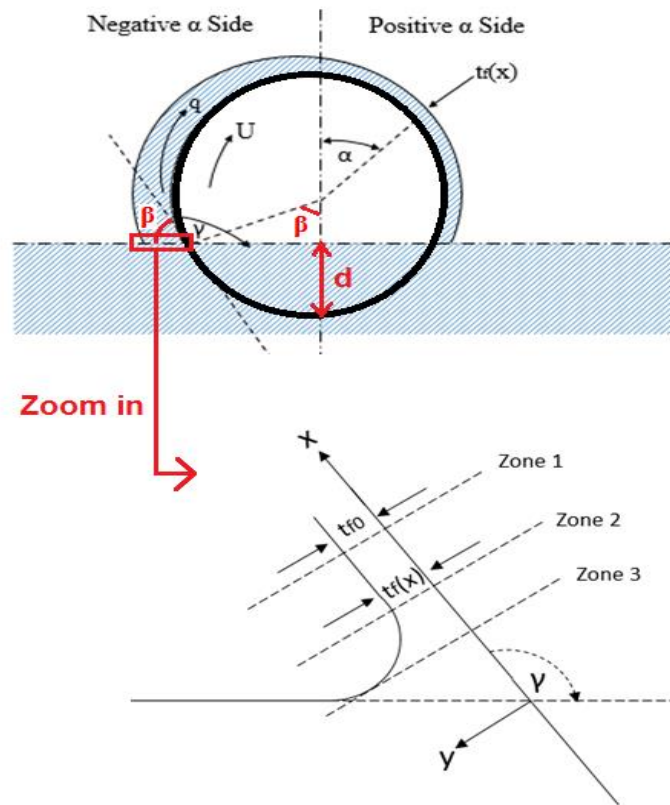


Figure 20: Film thickness variation over the rotating drum (7)

The contact angle depends on the water level in the solar still and is given by:

$$\sin \gamma = \sin (\pi - \gamma) = \sin \beta = \frac{R - d}{R} \quad (35)$$

where R represents the drum radius, d the drum depth in water, β the angle between the water surface and tangent to the drum at the contact point which is equal to the angle between the radius and the vertical.

It is also assumed that the water film formed is laminar and free from waves. Moreover, the problem is treated as one dimensional, since the velocities that are normal to the surface are neglected compared to parallel ones. Finally, the inertia forces

will be neglected too, since low speeds are used in the work. Thus, the liquid film is considered to be distributed in three zones as follows:

Zone 1: In this area, far from the surface of the water basin, the film thickness is constant at t_{f0} , and only viscous and gravity forces are considered in addition to driving roughness effects.

Zone 2: In this area, named as the dynamic meniscus area, the film thickness, t_f , varies with distance x . Here, surface tension as well as viscous, gravity forces and roughness effects are considered.

Zone 3: In this area, near to the surface of the water in the basin, named as the static meniscus area, only surface tension and roughness effects are considered, whereas flow effects are neglected. Writing the Navier Stokes equations for the three zones and applying the curvature continuity principle, the withdrawn flow rate can be calculated.

2. Momentum equations

For zone 1, starting by Navier Stoke Equation:

$$\mu \frac{\partial^2 u}{\partial y^2} - \rho g \sin \gamma - \left(\frac{\partial P}{\partial x} \right)_1 = \frac{\partial^2 u}{\partial y^2} - \rho g \sin \gamma + \frac{\Delta P}{d} = 0 \quad (36)$$

Where μ and ρ are the fluid's viscosity and density respectively, u represents the velocity and y represents the direction perpendicular to motion of fluid.

The boundary conditions needed to solve the previous equation are as follows:

$$\text{At } y = 0; u = U \text{ and at } y = t_{f0}; \frac{\partial u}{\partial y} = 0 \quad (37)$$

Where t_{f0} represents the constant film thickness.

Thus, integrating Equation (36) twice and applying to it the boundary conditions, the velocity profile is given by Equation (38.a):

$$u = \frac{(\rho g \sin \gamma - \frac{\Delta P}{d})}{2\mu} y^2 - \frac{(\rho g \sin \gamma - \frac{\Delta P}{d}) t_{f0}}{\mu} y + U \quad (38.a)$$

The flow rate q driven by the rotating cylinder is defined as in Equation (38.b):

$$q = \int_0^{t_{f0}} u dy = U t_{f0} \left(1 + \frac{\frac{\Delta P}{d} t_{f0}^2}{3\mu U} - \frac{\rho g \sin \gamma t_{f0}^2}{3\mu U} \right) \quad (38.b)$$

It should be noted that this equation cannot be solved, since it includes two unknown variables q and t_{f0} . Thus, Navier- Stoke Equation should be applied to Zone 2, where both capillary forces and roughness effect are considered. The equation becomes as follows:

$$\frac{\partial^2 u}{\partial y^2} = \frac{1}{\mu} \left(\rho g \sin \gamma + \left(\frac{\partial P}{\partial x} \right)_2 \right) \quad (39)$$

Using the following boundary conditions:

$$\text{At } y = 0 ; u = U \text{ and at } y = t_f ; \frac{\partial u}{\partial y} = 0 \quad (40)$$

The velocity profile becomes as in Equation (41):

$$u = \left(\frac{\rho g \sin \gamma + \left(\frac{\partial P}{\partial x} \right)_2}{2\mu} \right) y^2 - \left(\frac{\rho g \sin \gamma + \left(\frac{\partial P}{\partial x} \right)_2}{\mu} \right) t_f y + U \quad (41)$$

The flow rate can be calculated as in Equation (42):

$$q = \int_0^{t_f} u dy = Ut_f \left[1 - \frac{(\rho g \sin \gamma + \left(\frac{\partial P}{\partial x}\right)_2) t_f^2}{3\mu U} \right] \quad (42)$$

Using Equation (42), the velocity profile can be obtained as a function of the flow rate as in Equation (43):

$$u = \frac{3}{2t_f^2} \left(U - \frac{q}{t_f} \right) y^2 - \frac{3}{2t_f^2} \left(U - \frac{q}{t_f} \right) t_f y + U \quad (43)$$

3. Film Thickness over the Drum and Flow Rate Calculation

Pressure variation created over a roughness pattern is inversely proportional to the two principal radii of curvature. On the other hand, pressure drop created by capillary effects for the flow between rough elements is inversely proportional to the radius of curvature of the propagating film. Therefore, in presence of these two effects, the total film thickness can be modelled as the superposition of two functions as shown in Equation (44.a):

$$t_f(x) = t_{f1}(x) + t_{f2}(x) \quad (44.a)$$

The resulting radius of curvature can be calculated using a mathematical formulation as shown below:

$$\rho = \frac{\left[1 + \left(\frac{dt_f}{dx} \right)^2 \right]^{3/2}}{\left| \frac{d^2 t_f}{dx^2} \right|} = \frac{\left[1 + \left(\frac{d(t_{f1} + t_{f2})}{dx} \right)^2 \right]^{3/2}}{\left| \frac{d^2 (t_{f1} + t_{f2})}{dx^2} \right|} \quad (44.b)$$

It was shown that the variation of film thickness with x is so small compared to one, therefore:

$$\rho \approx \frac{1}{\left| \frac{d^2 t_{f1}}{dx^2} + \frac{d^2 t_{f2}}{dx^2} \right|} \Rightarrow \frac{1}{\rho} = \frac{1}{\rho_1} + \frac{1}{\rho_2} \quad (44.c)$$

Since the pressure drop is proportional to the inverse of the radius of curvature, then the total pressure drop is obtained from superposition of capillary effects, and the boundary condition for the free surface of Zone 2 is given in equation (44.d):

$$p_2 + \tau_{yy} = p_2 + 2\mu \frac{\partial u}{\partial x}(x, t_f) = -\sigma_s \frac{d^2 t_f}{dx^2} - \frac{\Delta P}{d} x \quad (44.d)$$

Where τ_{yy} represents the tangential stress at the free surface, and σ_s represents the surface tension.

Deriving equation (43) with respect to x we obtain:

$$\frac{\partial u}{\partial x}(x, t_f) = \frac{-3q}{2t_f^2} \frac{dt_f}{dx} \quad (45)$$

Deriving Equation (44.d) with respect to x we obtain:

$$\sigma_s \frac{d^3 t_f}{dx^3} = -\frac{3\mu}{t_f^3} \left(U t_f - q - \frac{(\rho g \sin \gamma - \frac{\Delta P}{d}) t_f^3}{3\mu} \right) + 3\mu q \frac{d}{dx} \left(\frac{1}{t_f^2} \frac{dt_f}{dx} \right) \quad (46)$$

With $q = U t_{f0} - \frac{(\rho g \sin \gamma - \frac{\Delta P}{d}) t_{f0}^3}{3\mu}$ from Equation (38.b)

At this stage, a third order differential equation is obtained which needs an approach to be solved. Thus, new dimensionless variables can be introduced which are Λ , λ and T_0 such that:

$$t_f = \Lambda t_{f0} \quad (47.a)$$

$$x = t_{f0} \lambda \left(\frac{\sigma_s}{3\mu U} \right)^{\frac{1}{3}} \quad (47.b)$$

$$\rho g s \sin \gamma - \frac{\Delta P}{d} = \frac{T_0^2 \mu U}{t_{f0}^2} \quad \text{if } \rho g s \sin \gamma > \frac{\Delta P}{d} \quad (47.c)$$

Since the right term of Equation (47.c) is always positive if $\rho g s \sin \gamma < \frac{\Delta P}{d}$, the dimensionless variables, T_0 is defined by Equation (47.d):

$$-\rho g s \sin \gamma + \frac{\Delta P}{d} = \frac{T_0^2 \mu U}{t_{f0}^2} \quad \text{if } \rho g s \sin \gamma < \frac{\Delta P}{d} \quad (47.d)$$

Using the defined dimensionless numbers in Equations (47) we obtain:

$$\frac{d^3 \Lambda}{d\lambda^3} = -\frac{1}{\Lambda^2} + \frac{1}{\Lambda^3} - \frac{T_0^2}{3} \left(\frac{1}{\Lambda^3} - 1 \right) + \left(-\frac{T_0^2}{3} + 1 \right) \left(\frac{3\mu U}{\sigma_s} \right)^{2/3} \frac{d}{d\lambda} \left(\frac{1}{\Lambda^2} \frac{d\Lambda}{d\lambda} \right) \quad \text{if } \rho g s \sin \gamma > \frac{\Delta P}{d} \quad (48.a)$$

$$\frac{d^3 \Lambda}{d\lambda^3} = -\frac{1}{\Lambda^2} + \frac{1}{\Lambda^3} + \frac{T_0^2}{3} \left(\frac{1}{\Lambda^3} - 1 \right) + \left(\frac{T_0^2}{3} + 1 \right) \left(\frac{3\mu U}{\sigma_s} \right)^{2/3} \frac{d}{d\lambda} \left(\frac{1}{\Lambda^2} \frac{d\Lambda}{d\lambda} \right) \quad \text{if } \rho g s \sin \gamma < \frac{\Delta P}{d} \quad (48.b)$$

By introducing the change in variable given by Equations (48) in the differential Equations (49), differential Equations (50) are obtained

$$X = (1 - T_0^2)^{\frac{1}{3}} \lambda, \text{ thus } \frac{d^3 \Lambda}{d\lambda^3} = \frac{d^3 \Lambda}{dX^3} (1 - T_0^2) \quad \text{if } \rho g s \sin \gamma > \frac{\Delta P}{d} \quad (49.a)$$

$$X = (1 + T_0^2)^{\frac{1}{3}} \lambda, \text{ thus } \frac{d^3 \Lambda}{d\lambda^3} = \frac{d^3 \Lambda}{dX^3} (1 + T_0^2) \quad \text{if } \rho g s \sin \gamma < \frac{\Delta P}{d} \quad (49.b)$$

$$\frac{d^3 \Lambda}{dX^3} - (1 - T_0^2)^{-\frac{1}{3}} \left(-\frac{T_0^2}{3} + 1 \right) \left(\frac{3\mu U}{\sigma_s} \right)^{\frac{2}{3}} \frac{d}{dX} \left(\frac{1}{\Lambda^2} \frac{d\Lambda}{dX} \right) - \frac{1 - \Lambda}{\Lambda^3} = 0 \quad \text{if } \rho g s \sin \gamma > \frac{\Delta P}{d} \quad (50.a)$$

$$\frac{d^3 \Lambda}{dX^3} - (1 + T_0^2)^{-\frac{1}{3}} \left(\frac{T_0^2}{3} + 1 \right) \left(\frac{3\mu U}{\sigma_s} \right)^{\frac{2}{3}} \frac{d}{dX} \left(\frac{1}{\Lambda^2} \frac{d\Lambda}{dX} \right) - \frac{1-\Lambda}{\Lambda^3} = 0 \quad \text{if } \rho g s \sin \gamma < \frac{\Delta P}{d} \quad (50.b)$$

The continuity of curvature of the free surface from Zone 1 to 3 provides the boundary conditions for the solution of the differential equation:

$$x = 0; \quad \Lambda \rightarrow \infty; \quad \frac{d^3 \Lambda}{d\lambda^3} \rightarrow \infty \quad \text{and} \quad \frac{d^2 \Lambda}{d\lambda^2} \rightarrow f(T_0; Ca) \quad (51.a)$$

where $Ca = \frac{3\mu U}{\sigma_s}$ is the capillary dimensionless number

$$\text{for } x = \infty; \quad \Lambda = 1; \quad \frac{d\Lambda}{d\lambda} = 0 \quad (51.b)$$

At the limit of the static meniscus zone, capillary statics gives:

$$\frac{d^2 t_f}{dx^2} \left(1 + \left(\frac{dt_f}{dx} \right)^2 \right)^{1.5} = \frac{\rho g x}{\sigma_s} \quad (52)$$

Integrating this equation using the boundary condition $x \rightarrow \infty; \frac{dt_f}{dx} \rightarrow \infty$ and using Landau and Levich (4) approach we obtain:

$$\Lambda \rightarrow 1; \quad \frac{d^2 \Lambda}{dX^2} = \frac{2^{1/2}}{3^{2/3}} T_0 (1 - T_0^2)^{\frac{2}{3}} Ca^{1/6} \quad \text{if } \rho g s \sin \gamma > \frac{\Delta P}{d} \quad (53.a)$$

$$\Lambda \rightarrow 1; \quad \frac{d^2 \Lambda}{dX^2} = \frac{2^{1/2}}{3^{2/3}} T_0 (1 + T_0^2)^{\frac{2}{3}} Ca^{1/6} \quad \text{if } \rho g s \sin \gamma > \frac{\Delta P}{d} \quad (53.b)$$

Applying continuity of the second derivative resulting from the continuity of curvature of the free surface from Zone 1 to 3 gives:

$$T_0 = \frac{3^{2/3}}{2^{1/2}} f(T_0; Ca) (1 - T_0^2)^{\frac{2}{3}} Ca^{\frac{1}{6}} \quad \text{if } \rho g s \sin \gamma > \frac{\Delta P}{d} \quad (54.a)$$

$$T_0 = \frac{3^{2/3}}{2^{1/2}} f(T_0; Ca) (1 + T_0^2)^{\frac{2}{3}} Ca^{\frac{1}{6}} \quad \text{if } \rho g \sin \gamma < \frac{\Delta P}{d} \quad (54.b)$$

Tharmalingam and Wilkinson (3) included the inertia effects by replacing function h_1 by function h_2 which is function of the fluid property number $Fp = \mu \left(\frac{g}{\rho \sigma_s^3} \right)^{\frac{1}{4}}$ in addition to the dimensionless groups T_0 and Ca :

$$T_0 = \frac{\frac{2}{3^{\frac{2}{3}}}}{\frac{1}{2^{\frac{2}{2}}}} h_2(T_0; Ca; Fp) (1 - T_0^2)^{\frac{2}{3}} Ca^{\frac{1}{6}} \left(\frac{\sin \gamma}{1 - \cos \gamma} \right)^{\frac{1}{2}} \quad \text{if } \rho g \sin \gamma > \frac{\Delta P}{d} \quad (55.a)$$

$$T_0 = \frac{\frac{2}{3^{\frac{2}{3}}}}{\frac{1}{2^{\frac{2}{2}}}} h_2(T_0; Ca; Fp) (1 + T_0^2)^{\frac{2}{3}} Ca^{\frac{1}{6}} \left(\frac{\sin \gamma}{1 - \cos \gamma} \right)^{\frac{1}{2}} \quad \text{if } \rho g \sin \gamma < \frac{\Delta P}{d} \quad (55.b)$$

T_0 allows the calculation of t_{f0} and therefore the calculation of the flow rate (q). From flow continuity, the obtained flow rate is constant over the rotating drum. Since the radius of the drum is not small, the flat plate theory can be extended to calculate the film thickness with variable angle (α) as shown in Figure (20) using the following relation (7):

$$q = Ut_{f0} - \frac{(\rho g \sin \gamma - \frac{\Delta P}{d}) t_{f0}^3}{3\mu} = Ut_f - \frac{(\rho g \sin \gamma - \frac{\Delta P}{d}) t_f^3}{3\mu} \quad (56)$$

From this formula, it is clear that pressure gradient due to surface roughness increases the driven flow rate. But this increase is not significant since it is multiplied by the cube of the film thickness which is in the order of nanometers.

D. Design Parameters

First of all, the properties of humid air are calculated using the improved relations by Tsilingris et al (67) according to the following equations:

The density of the saturated mixture for the temperature range between 0 and 100 °C was fitted by the following third degree polynomial as in Equation (57):

$$\rho_m = SD_0 + SD_1 \cdot t + SD_2 \cdot t^2 + SD_3 \cdot t^3 \quad (57)$$

Where t is the temperature range $0 < t < 100^\circ\text{C}$ and SD_0 , SD_1 , SD_2 and SD_3 are numerical constants and can be found in Table 1.

The saturated mixture viscosity (μ_m) for the temperature range between 0 and 100 °C was fitted by the following fourth degree polynomial as in Equation (58):

$$\mu_m = SV_0 + SV_1 \cdot t + SV_2 \cdot t^2 + SV_3 \cdot t^3 + SV_4 \cdot t^4 \quad (58)$$

Where SV_0 , SV_1 , SV_2 , SV_3 and SV_4 are numerical constants and can be found in Table 1.

The thermal conductivity (C_{pm}) of the saturated mixture for the temperature range of interest was fitted by the following fourth degree polynomial as in Equation (59):

$$C_{pm} = SC_0 + SC_1 \cdot t + SC_2 \cdot t^2 + SC_3 \cdot t^3 + SC_4 \cdot t^4 + SC_5 \cdot t^5 \quad (59)$$

Where SC_0 , SC_1 , SC_2 , SC_3 , SC_4 and SC_5 are numerical constants and can be found in Table 1.

The thermal diffusivity (α_m) of the saturated mixture for the temperature range of interest was fitted by the following fourth degree polynomial as in Equation (60):

$$\alpha_m = SA_0 + SA_1 \cdot t + SA_2 \cdot t^2 + SA_3 \cdot t^3 + SA_4 \cdot t^4 \quad (60)$$

Where SA_0, SA_1, SA_2, SA_3 and SA_4 are numerical constants and can be found in Table 1.

Finally, the Prandtl number (Pr_m) for the saturated mixture for the same temperature range was fitted by the following fourth degree polynomial as in equation (61):

$$Pr_m = SP_0 + SP_1.t + SP_2.t^2 + SP_3.t^3 + SP_4.t^4 \quad (61)$$

Where SP_0, SP_1, SP_2, SP_3 and SP_4 are numerical constants and can be found in Table 1.

Table 1: Numerical constants

Density (kg/m ³) COD = 0.999954	Viscosity (Ns/m ²) COD = 0.999997	Thermal conductivity (W/m K) COD = 0.999985	Specific heat capacity (kJ/kg K) COD = 0.999905	Thermal diffusivity (m ² /s) COD = 0.999	Prandtl number COD = 0.9999
SD0 = 1.293	SV0 = 1.715E-5	SK0 = 2.400E-2	SC0 = 1.004571427	SA0 = 1.847E-5	SP0 = 0.721
SD1 = -5.538E-3	SV1 = 4.722E-8	SK1 = 7.278E-5	SC1 = 2.050E-3	SA1 = 1.161E-7	SP1 = - 3.703E-4
SD2 = 3.860E-5	SV2 = -3.663E- 10	SK2 = -1.788E-2	SC2 = -1.631E-4	SA2 = 2.373E-10	SP2 = 2.240E- 5
SD3 = -5.253E-7	SV3 = 1.873E-12	SK3 = -1.351E-9	SC3 = 6.212E-6	SA3 = -5.769E-12	SP3 = - 4.162E-7
	SV4 = -8.050E- 14	SK4 = -3.322E-11	SC4 = -8.830E-8	SA4 = -6.369E-14	SP4 = 4.969E- 9
			SC5 = 5.071E-10		

Other design parameters are used in the system equations, such as the transmissivity and emissivity of glass and water, the conductivity, specific heat, thickness and density of the aluminum (or copper) foil used, the Stefan- Boltzmann constant, the specific heat of glass, and the dimensions of the basin, drum and the cover

used in the set up. In addition, the initial conditions include the water, cover, and drum initial temperatures. Having the system's geometry, operating and weather conditions (solar radiation, wind speed, and air temperature) and initial temperatures initially known (at time=0, T_{d0} , T_{c0} , T_{b0}), the heat balance equations will then be used in order to calculate the temperatures at the next time step using the explicit method.

Regarding the boundary conditions of the system, the brine water's temperature is assumed to be the same as the first drum element leaving the water.

All presented equations were implemented into a numerical code using the Matlab software which was used to solve for the different variables of interest: hourly temperatures of the different elements of the solar still and water yield production. The inputs to the code are the system's geometry, operating and weather conditions (solar radiation, wind speed, and air temperature) and initial temperatures of the solar still elements. The heat balance equations will then be used in order to calculate the temperatures at the next time step using the explicit method with a time step of 1 s. The brine water's temperature is assumed to be the same as the first drum element leaving the water. The following flowchart represents the solution methodology:

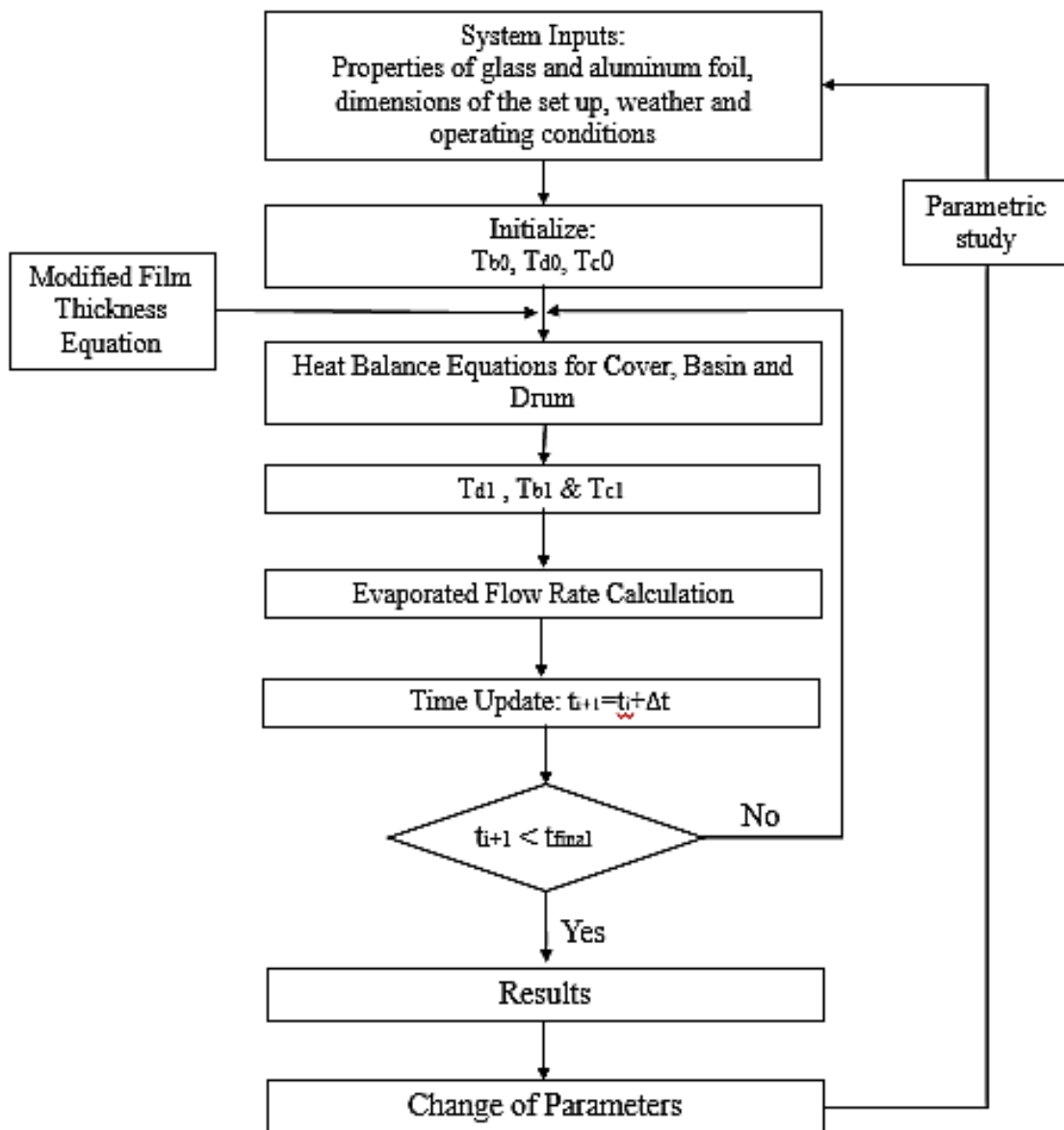


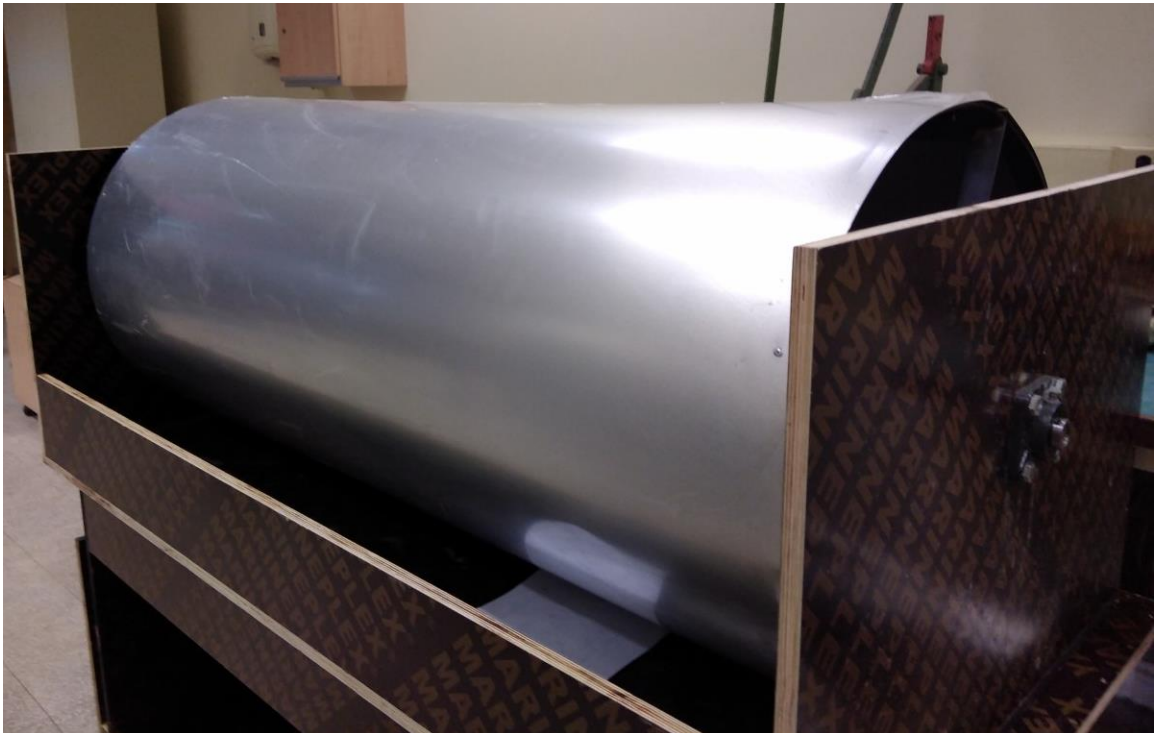
Figure 21: Flowchart of solution methodology

CHAPTER III

EXPERIMENTAL PROCEDURE

A. Experimental Set Up

An experimental set-up was constructed to validate the simplified mathematical model. Three set ups were manufactured: the first one is considered a control, without a drum, while the other two set ups are made of a smooth drum and a rough drum respectively. The water basin is made of plywood of 18 mm thickness and an area of 1 m² (0.67 m × 1.5 m) coated with black fiberglass material, while the cover is made of plexi- glass as shown in Figures (22), which represent the de-assembled parts of the set up.



(a)



(b)



(c)



Figure 22: De- assembled parts of the set up (a): Smooth drum with basin, (b) Basin, (c) Rough drums, (d): Triangular glass cover

The drum in Figure (22. c) is constructed from a folded rough aluminum sheet of 1 mm thickness, 0.6 m diameter and 1.4 m length. The drums (one smooth and two rough) are mounted on a low- carbon (20 mm diameter and 1.7 m length) steel shaft and fixed on 20 mm ball bearings to hold in place as shown in Figure (23).

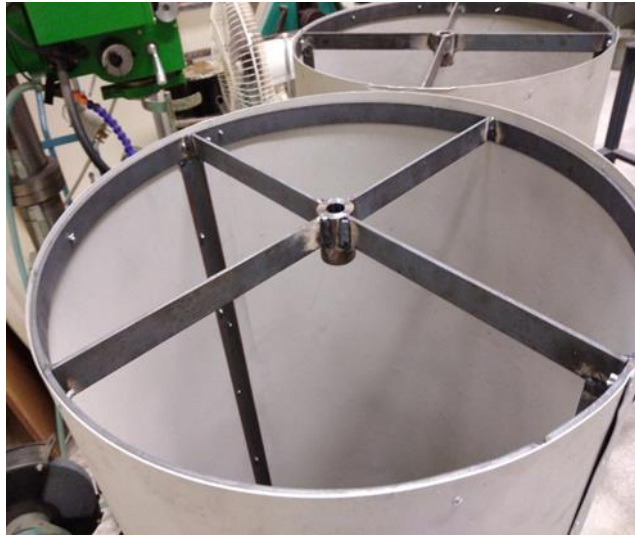


Figure 23: Opening for shaft placement

Inclined plexi channels, as shown in Figures (24), were constructed in order to collect the water distillate through a round outlet. Outlets with ball-type valves were connected to these channels for distillate collection and other outlets were also installed at the bottom of the basin for brine discharge as shown in Figures (24).



(a)



(b)

Figure 24: (a) Inclined plexy channels with (b) Ball type valves

The shaft was operated by a 12 V DC motor, as shown in Figure (25), of 80% efficiency, and rated power of 2 Watts. A current of 0.1 Amp was used, while a voltage of 6 V was maintained to reduce its speed.



Figure 25: Motor used for shaft operation

Power was maintained directly from a power supply, as shown in Figure (26), connected to a grid, but the solar panels option is also possible, which will save energy.



Figure 26: Power supply used to maintain power needs

The final assembled set up including the cover, the basin and the rough rotating drum with all the additional parts is shown in Figure (27).

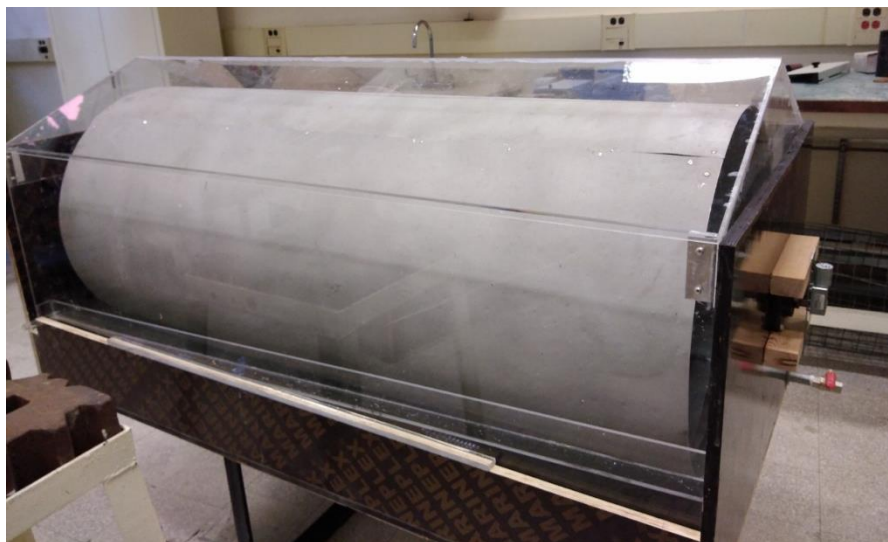


Figure 27: Final assembled set up

B. Methods for the Creation of Uniformly Rough Surfaces

It is of high importance to investigate the methods used in order to create uniformly rough surfaces. Soft molding is considered a promising method used for meso- scale- area manufacture, which consists of putting an elastomeric mold on the external of a spin-coated polymer film under the effect of a light pressure, enabling the mold to captivate the solvent. Then, the pressure is removed, and both the mold and the substrate are left to rest for a while. The obtained structure is powerful and protected with no bending or imperfections (68). Another method is laser texturing. This method is also characterized by its high precision like soft molding method. Many studies adopted this method in their work, such as Yunfeng et al. (69), where an Nd: YAG laser was used to create surface roughness on rolled surfaces, for reducing friction and improving precision on steel surfaces. Etching is also a method used for roughness creation, especially for micro-chips and boards. However, these methods are mostly effective on small scale applications and even micro- scale ones, unlike the application targeted in this study. Sandblasting, on the other hand, is another method used to roughen surfaces especially on large scales with minimal cost. It is defined as the activity of persuasively impelling a stream of abrasive material over a surface under high pressure for many purposes including smoothing, roughening or shaping a surface, to expel surface impurities. The sandblasting machine includes a mixing chamber where air and sand are mixed, then the resultant goes into a hand held nozzle, where particles are exhausted to the desired surface as shown in Figure (28). The operator should be well trained, and safety measurements should be taken, in order to obtain a well finished uniform surface (70).

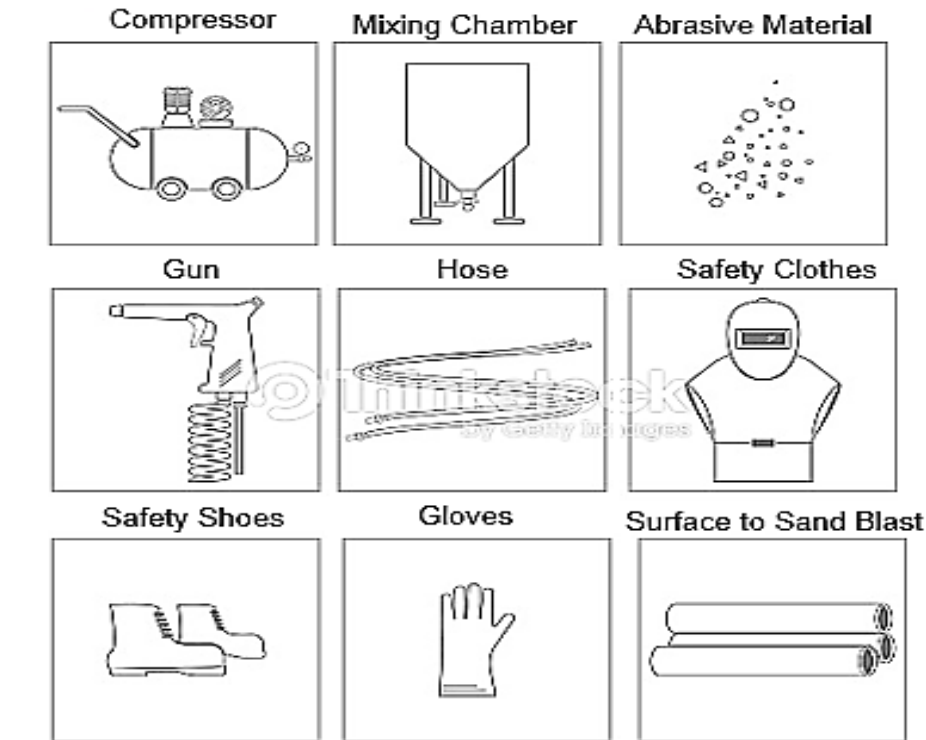


Figure 28: Sandblasting process equipment

Many studies have adopted this method to create rough surfaces. For example, in the work of Flanagan et al. (71), sandblasting method was utilized to create different surface roughness grades in automotive applications. Another study (72) adopted the sandblasting technique in order to create rough surfaces and relate it to wettability. Sandblasting is also widely used in dentistry, where in the study of Tonello et al. (73), sandblasting was performed to enhance the bonding strength of veneering ceramic.

C. Roughening Process

Regarding the roughening process, the smooth aluminum sheets purchased were sandblasted manually using jet of 7 bars pressure and air flow rate of $10.3 \text{ m}^3/\text{min}$ as shown in Figure (29) . This high flow rate allows the swirling effect to take place inside the nozzle of the jet and discharge the sand particles at high velocity, therefore safety

precautions should be taken by the worker such as wearing a special safety coat as shown in Figure (29). Sand is fed from a vertical sand reservoir connected to a duct, where a venturi nozzle is available at the end of it.

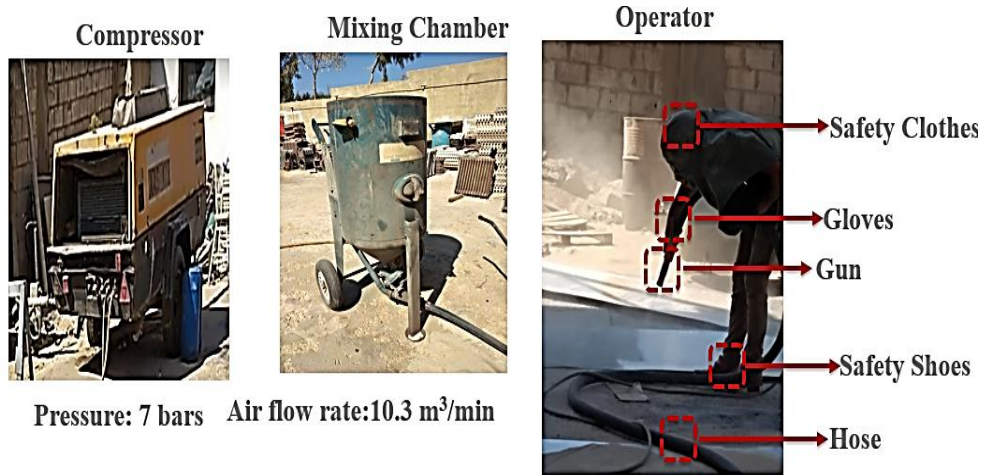


Figure 29: Manual sand blasting process

The sand particle size used to create different grades of roughness is shown in Figure (30).



Figure 30: Particle sand size

The particles used were examined and SEM images were taken using MIRA 3 TESKAN system available at the American University of Beirut, which provides images of high resolution and low noise as shown in Figures (31) and (32).



Figure 31: MIRA 3 TESKAN system

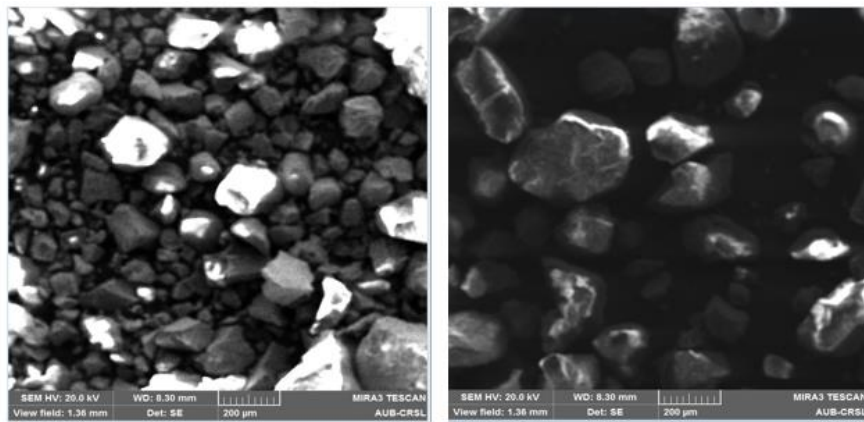


Figure 32: SEM images of the sand particles

The roughness created was further measured in order to calculate the ration of the enhanced area of the rough surface compared to the smooth one. This was done using DektakXT stylus profiler with a stylus size of 2 μm B- type, which also allows for the measurement of the surface area as shown in Figure (33) and (34), where Figure (35) represents the settings used in the measuring process.

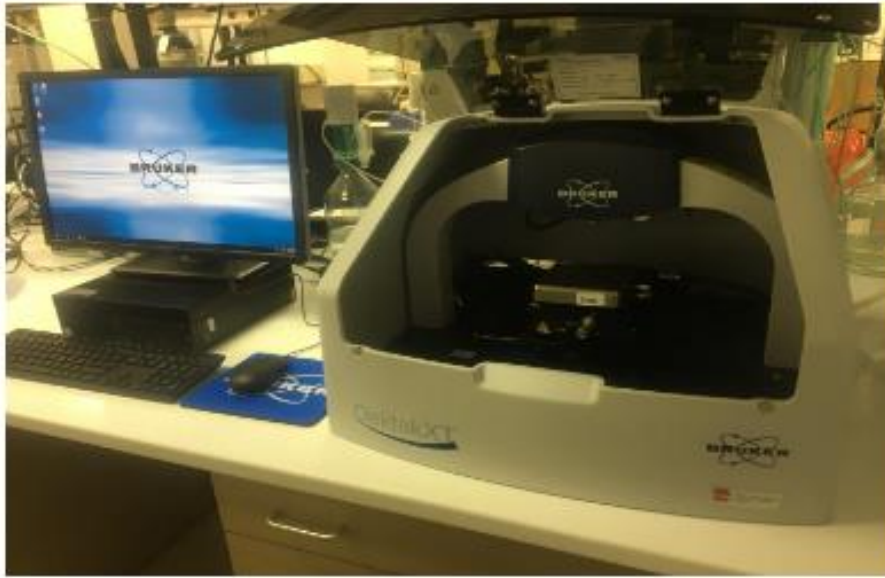


Figure 33: DektakXT stylus profiler



Figure 34: B- Type stylus of 2 μm size

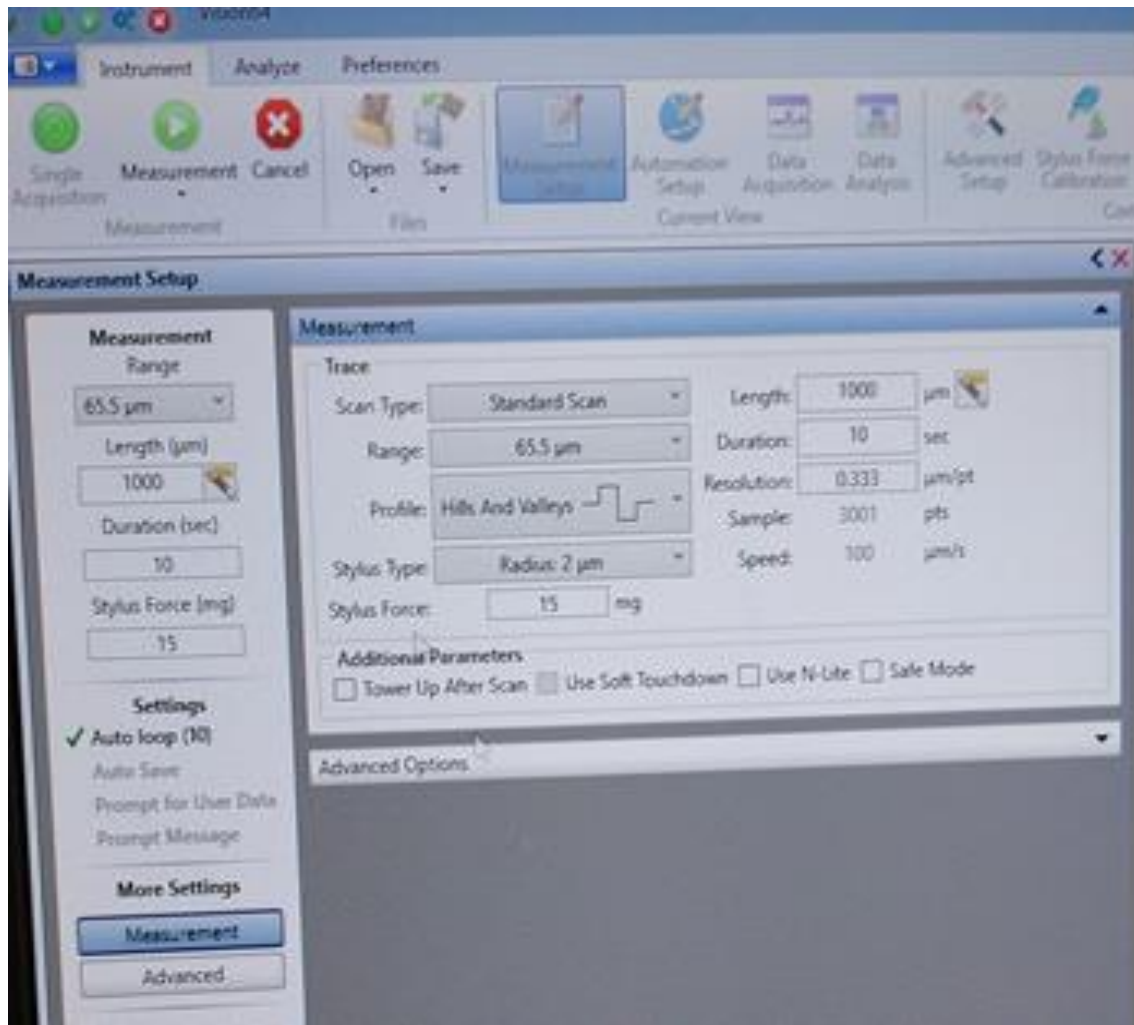


Figure 35: Settings of roughness measurement

D. Measurement Apparatus and Data Acquisition

Data is recorded daily starting from the early morning of March. Once the DC motors are operated, the shafts will start rotating as well, inducing the rotational motion of the drums too. As the drums rotate, a water film will be created on their surface, which will evaporate as sunlight hits the set ups. This will also stimulate the evaporation process from the water basin. Feed water is supplied to the still basin through an inlet up to the desired level based on the brine depth required for the particular experiment. A graduated cylinder is mounted at the bottom level of all constructed stills to allow the

measurement of the water level in the basins and the collection of the distillate. Temperatures inside and outside the still cover, inside the still cavity and within the water of the basin were recorded using K- type thermocouples (accuracy ± 0.5 °C) connected to an OM- DaqPro Data Logger . In addition, the initial drums temperature and its variation with time were measured using infrared thermometer (accuracy ± 0.1 °C). Also, ambient weather conditions such as solar radiation, humidity and ambient temperature, wind direction and wind speed were recorded every minute using pyranometer of accuracy ± 4 W/m², OM-EL-USB-2 sensors with an accuracy of ± 0.5 °C in temperature and ± 3 % in relative humidity, and anemometer of accuracy ± 0.5 m/s respectively. Distillates were collected in Pyrex Erlenmeyer flasks. Figures (36 (a), (b)) represent the set ups under operation at different times, while Figure (37) represents obvious and large water drops formed on the walls of the glass cover. Figures (38) represent the different sensors used in the experiment.



(a)



(b)

Figure 36: Set ups under operation



Figure 37: Water droplets formed of the walls of the cover



(a)



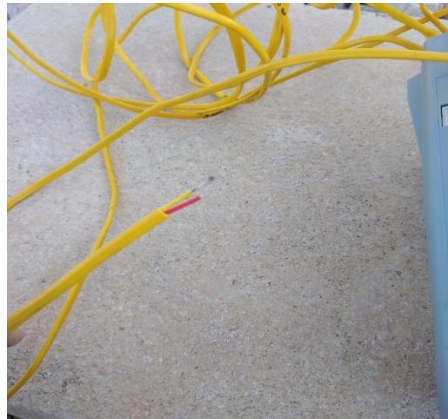
(b)



(c)



(d)



(e)



(f)

Figure 38: Sensors used in the experiment; (a) Anemometer, (b) Pyranometer, (c): Infrared thermometer, (d) OM-EL-USB-2, (e) K-Type thermocouple, (f) OM- DaqPro data logger

CHAPTER IV

VALIDATION OF THE SIMPLIFIED MODEL

First, the ability of the simplified model in predicting the solar still productivity and water temperature variation with time for the case of a drum with smooth surface was validated using the results of Malaeb et al. (5). Then, in order to validate the accuracy of the model in computing the effect of surface roughness experimental results were used.

A. Validation with Literature

Malaeb et al. (5) model results and the developed model results were compared for validation for a solar still characterized by: period: typical day of June, solar still base area = 1 m², drum radius = 30 cm, drum length = 140 cm corresponding to a drum's radius to length ratios = 0.214, contact angle = 170°, drum rotational speed = 0.25 rpm. Table 2 represents the hourly variation of the weather conditions including: the wind velocity (m/s), the dry and wet bulb temperatures (°C), the horizontal and vertical surface radiation (Wh/m²) and the humidity ratio for the month of June.

Table 2: Hourly variation of weather conditions

Hour	Wind Velocity (m/s)	Dry Bulb Temperature (°C)	Wet Bulb Temperature (°C)	Horizontal Surface Radiation (Wh/m ²)	Vertical Surface Radiation (Wh/m ²)	Humidity Ratio
1	1	26.7	19	0	0	0.0105
2	1.5	26.1	18.5	0	0	0.0101
3	2.1	26.7	18.6	0	0	0.0100
4	3.1	26.7	18.6	0	0	0.0100
5	3.6	26.7	19	0	0	0.0105
6	4.6	26.1	19.9	2.6	13.7	0.0120
7	5.7	26.7	21	91.6	269.9	0.0132
8	5.7	26.7	20.9	240	444.5	0.0131

9	5.1	27.2	20.8	382.6	525	0.0127
10	5.1	27.2	20.7	667.5	566.9	0.0126
11	5.7	27.8	20.7	794.4	590	0.0123
12	5.7	28.3	20.8	877	602.2	0.0123
13	6.2	28.3	20.6	909.6	606.5	0.0120
14	6.2	28.3	20.8	890.2	603.9	0.0123
15	5.1	29.4	20.9	820	594	0.0119
16	6.2	30	20.8	703.7	574.1	0.0116
17	5.7	29.4	20.8	416.3	538.2	0.0118
18	4.1	28.9	20.8	277.7	470.8	0.0120
19	4.1	28.3	20.6	129.2	330.5	0.0120
20	5.7	27.8	20.7	10.5	49.1	0.0123
21	5.7	28.9	20.5	0	0	0.0116
22	5.7	27.8	20.3	0	0	0.0118
23	5.7	27.8	20.5	0	0	0.0121
24	5.7	27.8	20.6	0	0	0.0122

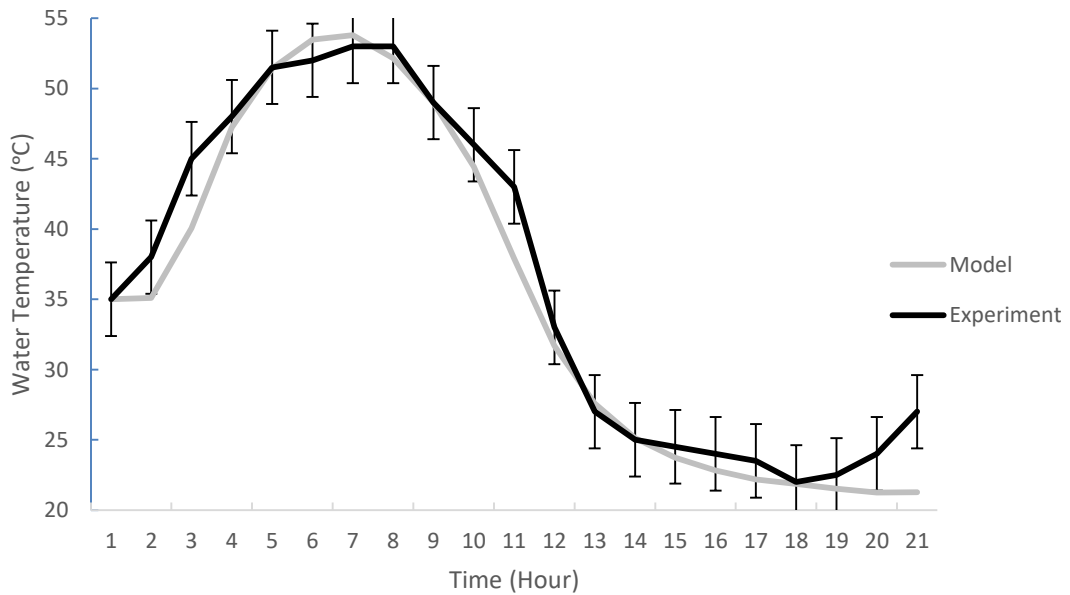
Figures (39.a) and (39.b) represent comparison of water temperature variation and solar still productivity with time respectively (Hour 0 corresponds to 12 noon). Good agreement was obtained between the compared results with a maximum relative error in the order of 10% validating the ability of the model in capturing the physics behind the operation of a solar still characterized by a drum with smooth surface, where the error was calculated using Equation (62) and a sample of the error calculation for a system with a rough drum is shown in Table 3.

$$\text{error}(\%) = (|(\text{experimental value} - \text{model value})|/\text{model value}) \times 100 \quad (62)$$

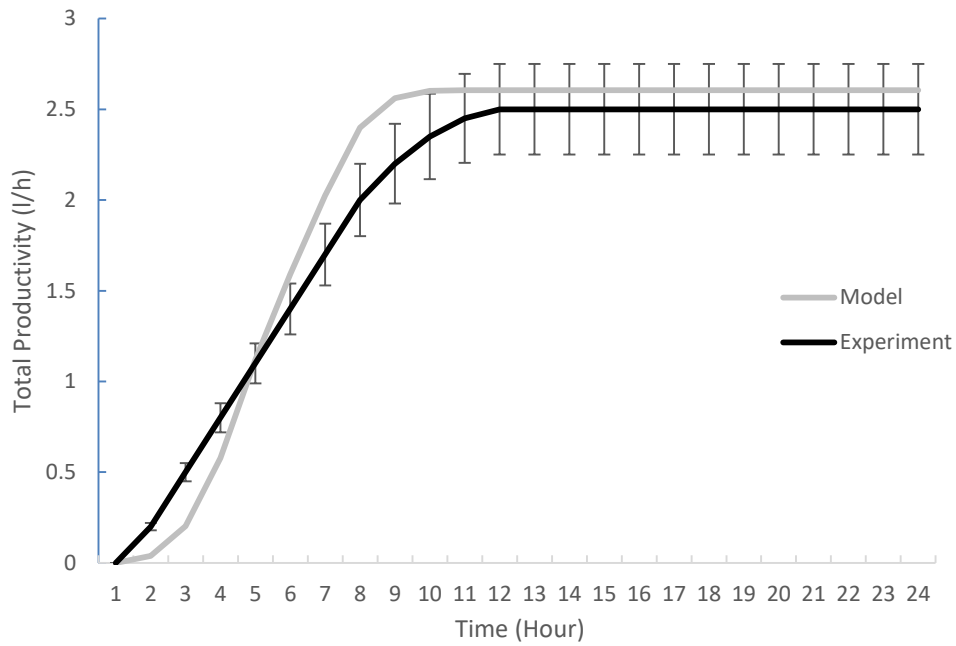
Table 3: Sample calculation of error for a system with rough drum

Hour	Td Model (°C)	Td Experiment (°C)	Error	Tg Model (°C)	Tg Experiment (°C)	Error	Tw Model (°C)	Tw Experiment (°C)	Error
1	13.84	14.76	6.61	19.03	17.21	9.60	11.37	12.39	9.017
2	15.41	16.56	7.46	20.77	18.82	9.36	11.79	12.88	9.23
3	17.01	18.71	9.96	21.55	19.48	9.61	12.11	13.25	9.39
4	21.42	19.31	9.85	23.16	21.22	8.37	14.21	15.56	9.44

5	25.42	24.02	5.51	25.51	22.98	9.93	16.53	17.31	4.70
6	26.94	25.14	6.67	26.55	24.37	8.20	18.72	19.9	6.27
7	28.73	26.40	8.09	28.65	26.06	9.05	20.72	21.87	5.53
8	29.68	27.87	6.09	30.87	27.98	9.36	22.37	22.98	2.69
9	30.99	28.01	9.60	31.45	28.36	9.84	23.58	24.03	1.89
10	31.30	28.54	8.82	31.71	28.54	9.96	24.32	24.79	1.94
11	31.78	28.75	9.53	32.03	28.88	9.81	24.48	25.05	2.32
12	31.97	29.9	6.49	32.26	29.87	7.42	24.73	27.09	9.53
13	29.03	28.36	2.31	31.88	29.38	7.84	23.80	25.9	8.78
14	25.80	26.40	2.32	31.51	28.39	9.88	21.98	23.71	7.84
15	23.21	24.27	4.54	31.06	27.98	9.92	19.66	21.35	8.56
16	21.00	19.06	9.23	27.18	24.65	9.31 4	17.67	19.06	7.87
17	19.06	18.78	1.45	24.07	22.15	7.98	15.92	17.14	7.59
18	17.33	18.50	6.72	21.83	19.69	9.77	14.63	15.87	8.41
19	15.98	16.98	6.23	20.12	18.55	7.80	13.73	14.9	8.49
20	14.99	15.87	5.81	18.97	17.80	6.15	12.89	13.76	6.72
21	14.10	14.55	3.18	17.99	17.03	5.32	12.24	13.16	7.51
22	13.37	14.09	5.43	17.16	16.65	3.00	11.25	12.23	8.71
23	12.12	12.98	7.09	17.43	16.40	5.92	11.16	11.99	7.37
24	12.39	13.55	9.36	17.65	16.68	5.49	11.27	12.06	7.05 4



(a)



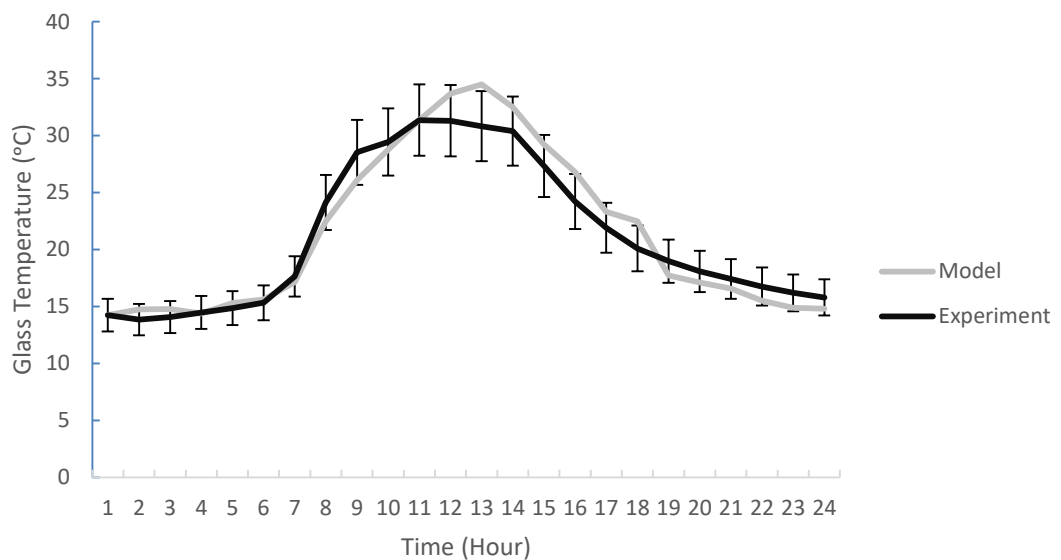
(b)

Figure 39: Comparison of the model results with experimental results of Malaeb et al. (5): a) water temperature variation with time; b) solar still productivity with time

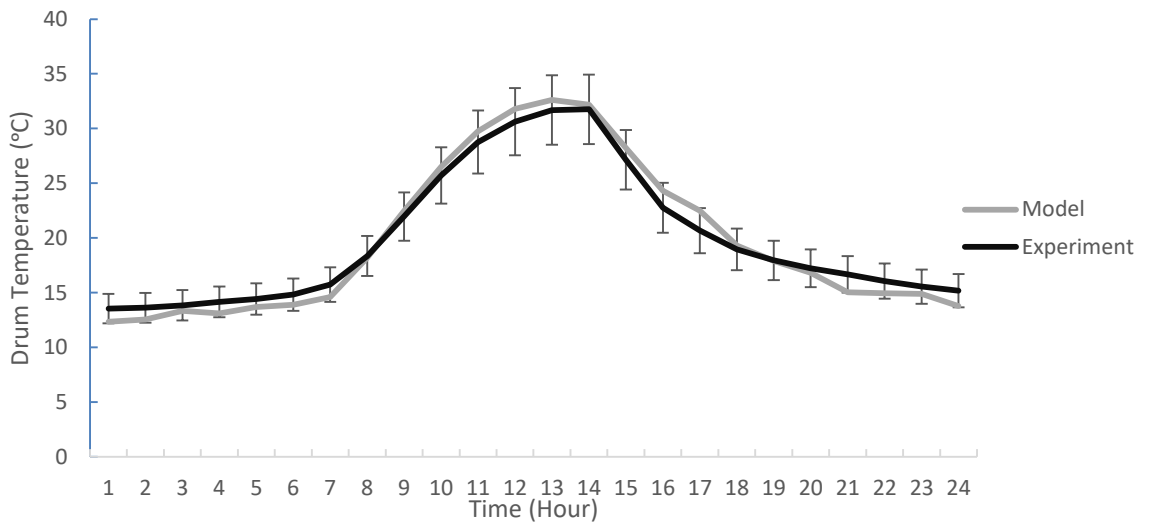
B. Validation with Experiments

The experimental set up was operated in order to validate the developed model. Three set ups were used, a set up without a drum, a setup with a smooth surface drum, and a third set up including a rough drum, where the area enhancement was found to be 2.2, compared with the smooth surface of an aluminum sheet of the same properties, based on the measurements of the DektakXT stylus profiler. The solar still set up is characterized by: period: typical day of March, solar still base area = 1 m^2 , drum radius = 30 cm, drum length = 140 cm corresponding to a drum's radius to length ratios = 0.214, contact angle = 170° , drum rotational speed = 0.25 rpm The temperatures of the glass cover, drum and water were continuously varying with the variation of the solar intensity and ambient temperature along the day. The systems were operated

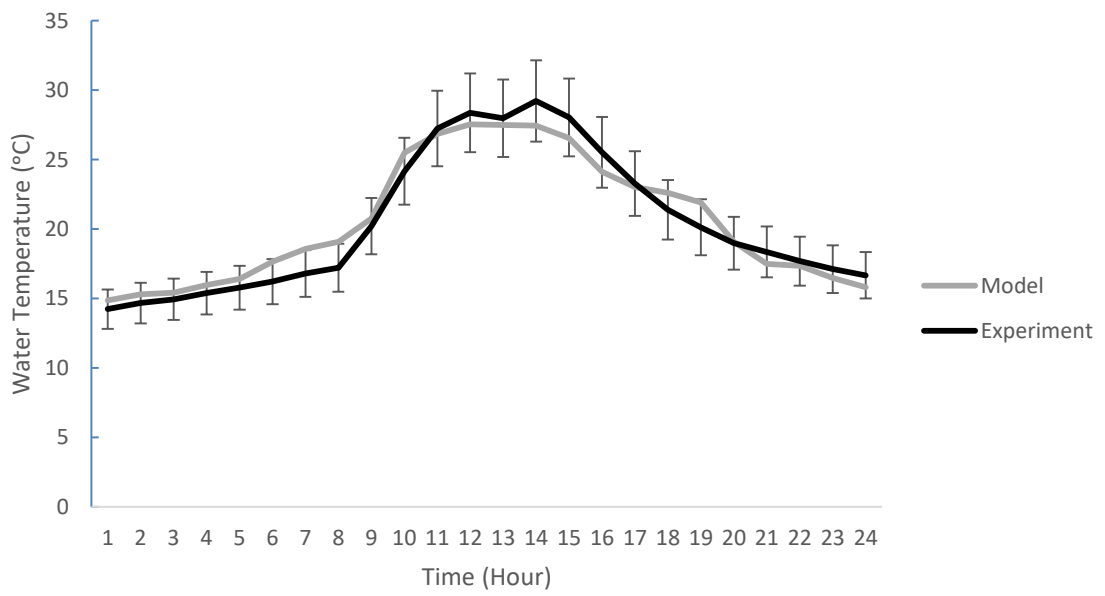
continuously for 24 hours and data were recorded accordingly. Figures (40. a, b, c, d) represent comparison of glass, drum and water temperatures variation in addition to the variation of the solar still productivity with time respectively for the set up with a smooth drum. Good agreement was obtained between the compared results with a maximum relative error in the order of 10%. On the other hand, Figures (41.a, b, c and d) represent comparison of glass, drum and water temperatures variation in addition to the variation of the solar still productivity with time respectively for the set up with a rough drum. Good agreement was obtained between the compared results with a maximum relative error in the order of 10%.



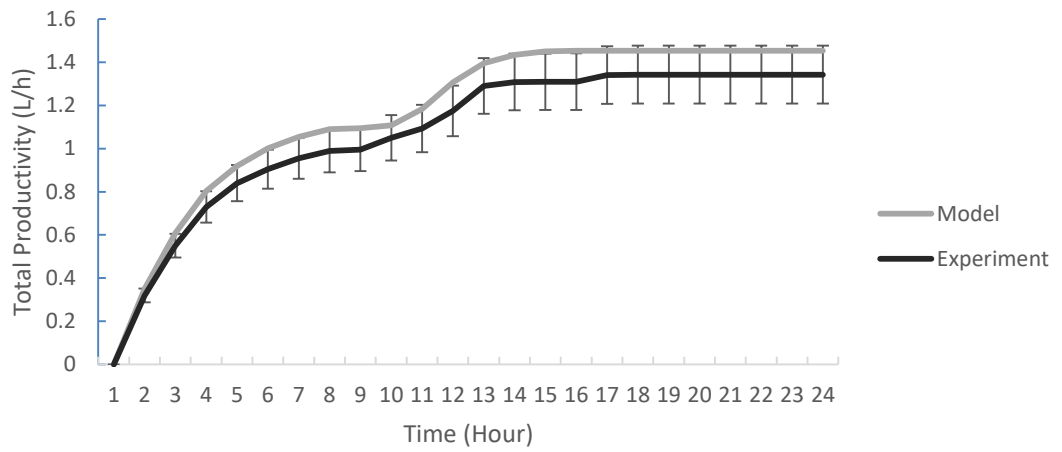
(a)



(b)

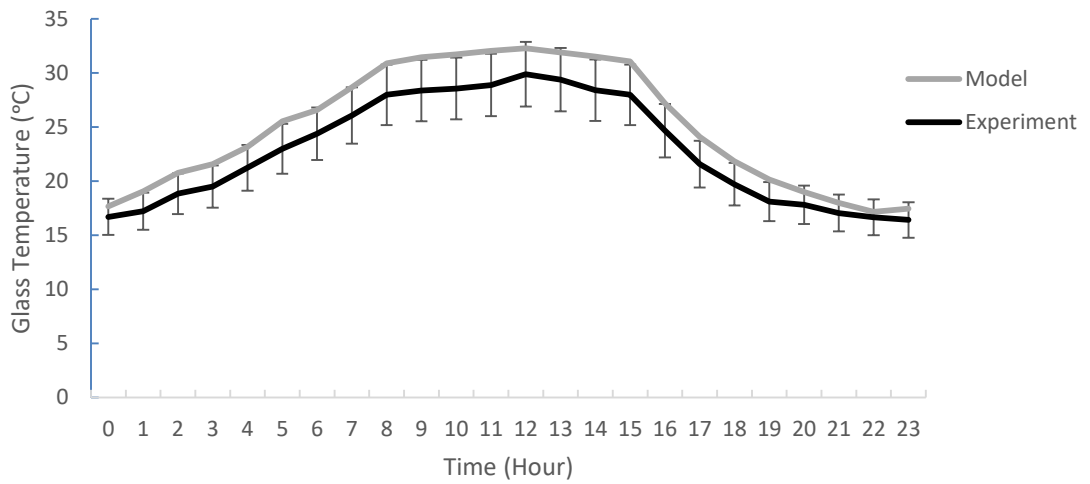


(c)

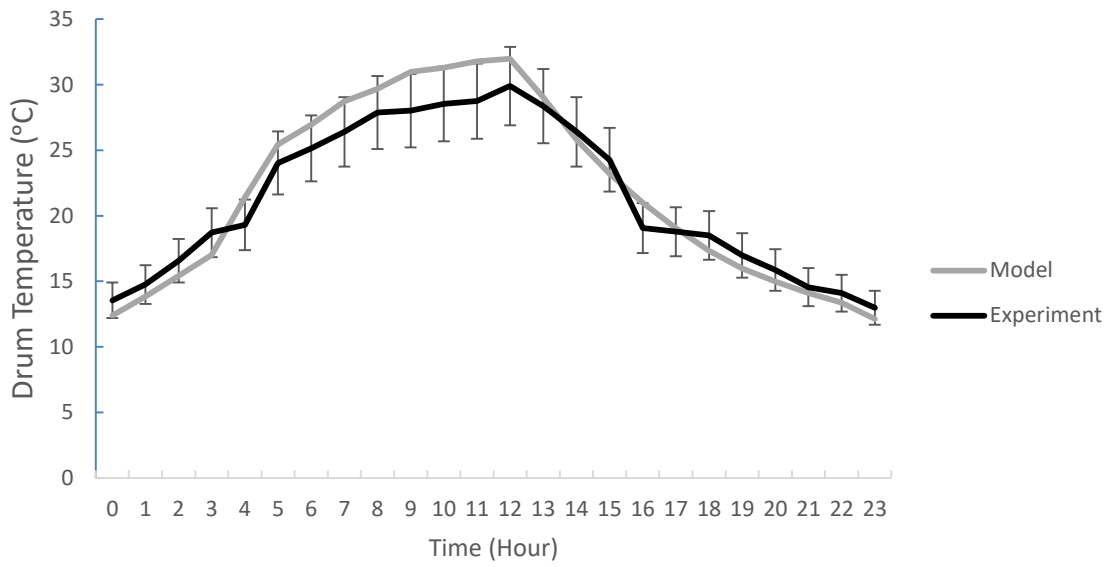


(d)

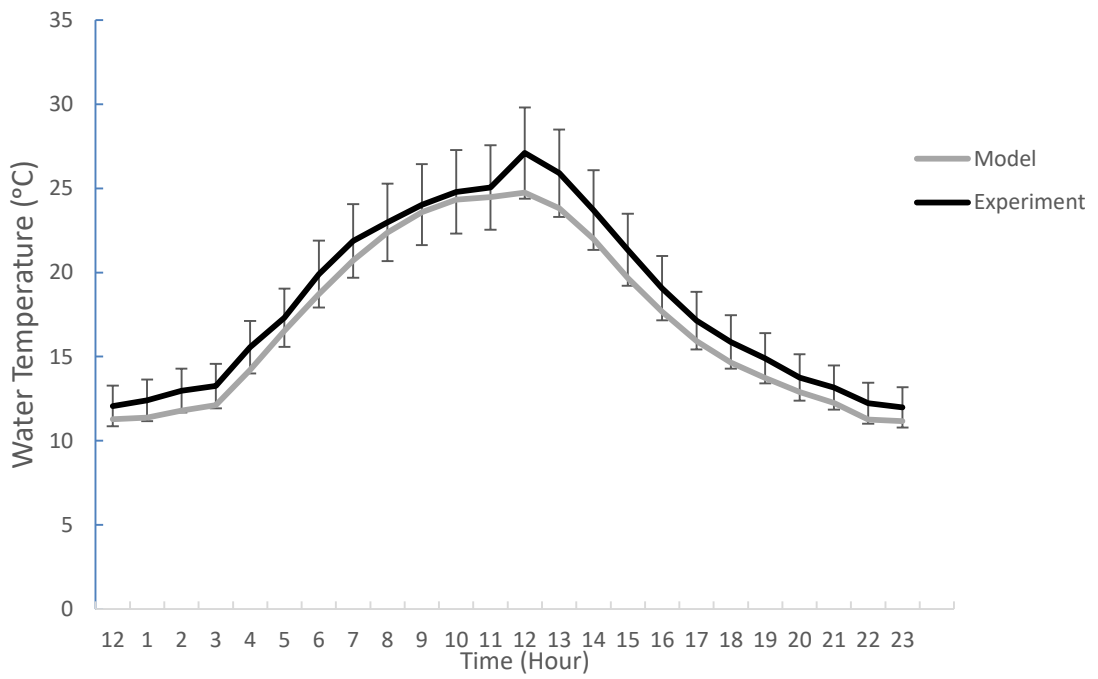
Figure 40: Comparison of model and experimental results of: (a): glass, (b): drum, (c): water temperatures and (d) hourly productivity with time for a set up with a drum with smooth surface



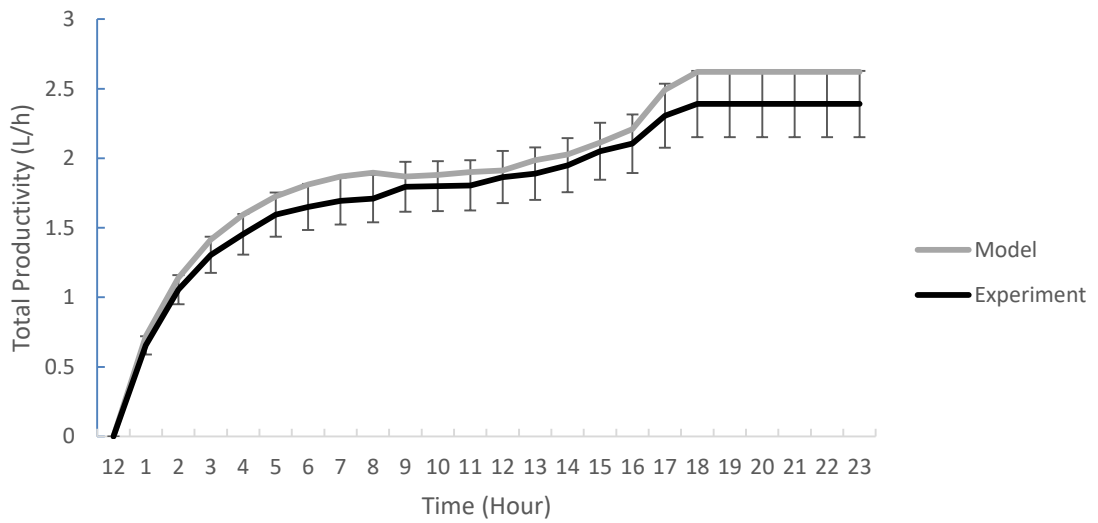
(a)



(b)



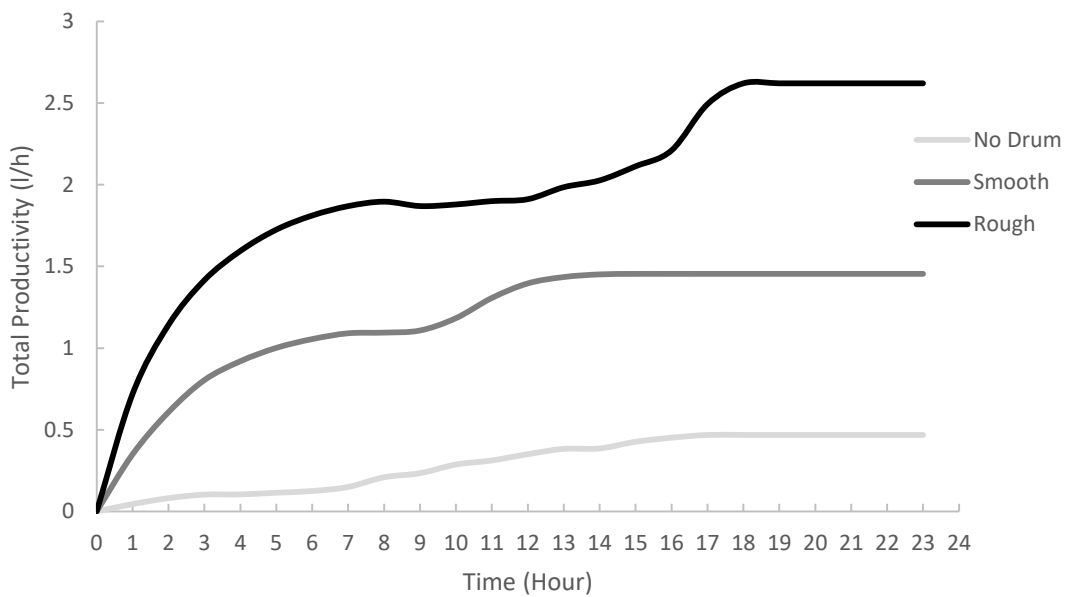
(c)



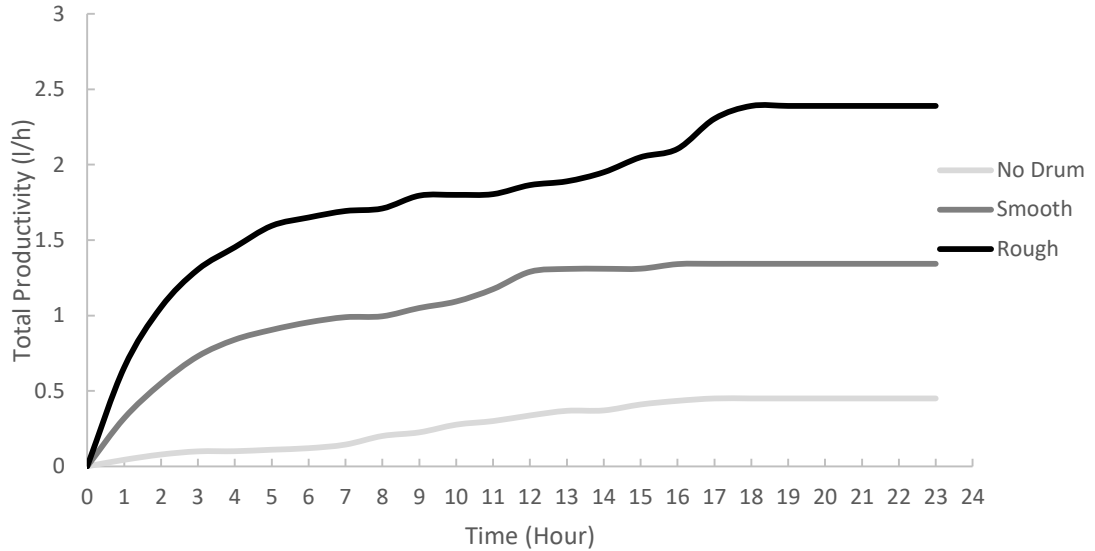
(d)

Figure 41: Comparison of model and experimental results of: (a): glass, (b): drum, (c): water temperatures and (d) hourly productivity with time for a set up with a drum with rough surface

Regarding the roughness effect, a comparison was done between the total water produced from the three set ups. The results are shown in Figures (42.a and b) for both model and experimental results respectively.



(a)



(b)

Figure 42: Comparison between no drum, smooth and rough systems productivity: (a): Model and (b): Experimental values

Based on the previous results, it is obvious that roughness largely increases the system's productivity. In fact, an increase of 78% was noticed between the system with a smooth drum and the system with a rough one. The system with the smooth drum under the mentioned operating conditions recorded a maximum value of 1.343 l/day/m² experimentally, while the system with a rough drum achieved a total water yield value of 2.39 l/day/m². This is directly related to that in the case of a rough surface, an increase of 2.2 in the area was created, in addition to that a higher temperature difference was obtained between the drum and the glass cover elements, which increased the heat transfer rate between the different components of the solar still. Therefore, the developed simplified model along with the experiment had the ability to show the effect of roughness in enhancing the system's performance and increasing the

system's productivity by 78%. Talking about the enhancement with respect to comparing the still without drum and the two other stills, an enhancement of 198 % was observed between the set up with no drum and the set up that includes a smooth drum, while an enhancement of 431.1 % was observed when comparing the set up without drum and the system including the rough drum.

C. Uncertainty Analysis

Experimental uncertainties occur mainly because of the reading procedure and weather conditions. In order to quantify the uncertainty of the experimental work, the method of Agrawal et al. (74) was followed in calculating the uncertainties in the experimental work that mainly divides the uncertainties into internal and external.

Regarding the internal uncertainty, the uncertainty of various parameters was estimated for the experimental readings. The percentage of uncertainty was calculated as follows:

$$\%Uncertainty = (U_i / B) \times 100 \quad (64)$$

where

$$U_i = \sqrt{(\sigma_1^2 + \sigma_2^2 + \dots + \sigma_s^2)} / S^2 \quad (65)$$

$$\sigma = \sqrt{\sum (X - \bar{X})^2 / S_0} \quad (66)$$

U_i is the internal uncertainty, B is the average of the total number of readings, σ is the standard deviation of one set of the readings, S is the total number of readings, $(X - \bar{X})$

is the deviation from the readings from the mean, S_0 is the number of readings in one set.

The results of 5 runs of the experiments are shown in Table (4.a, b) including the different temperatures (drum, cover, water and ambient) and solar intensity for the set up including a rough drum as examples.

Table 4: Sample calculation of internal uncertainty
(a)

Hour	Td Experiment (°C)					Tg Experiment (°C)				Tw Experiment (°C)					
	Run 1	Run 2	Run 3	Run 4	Run 5	Run 1	Run 2	Run 3	Run 4	Run 5	Run 1	Run 2	Run 3	Run 4	Run 5
1	14.76	14.86	14.96	14.96	14.96	17.21	17.31	17.10	17.42	17.15	12.32	12.54	12.1	12.3	12.1
2	16.56	16.71	16.85	16.76	16.76	18.82	18.92	18.71	19.03	18.76	12.88	13.02	12.58	12.78	12.67
3	18.71	18.96	19.21	18.91	18.91	19.48	19.58	19.37	19.69	19.42	13.25	13.39	12.95	13.15	13.0
4	19.31	19.21	19.11	19.51	19.51	21.22	21.32	21.11	21.43	21.16	15.56	15.70	15.26	15.46	15.35
5	24.02	23.92	23.81	24.22	24.22	22.98	23.08	22.87	23.19	22.92	17.31	17.46	17.01	17.21	17.10
6	25.14	25.43	25.39	25.34	25.34	24.37	24.47	24.26	24.58	24.31	19.9	20.04	19.60	19.80	19.69
7	26.40	24.65	26.65	26.60	26.60	26.06	26.16	25.95	26.27	26.00	21.87	22.01	21.57	21.77	21.6
8	27.87	27.64	28.12	28.07	28.07	27.98	28.08	27.87	28.19	27.92	22.98	23.12	22.68	22.88	22.77
9	28.01	28.11	28.26	28.21	28.21	28.36	28.46	28.25	28.57	28.30	24.03	24.17	23.73	23.93	23.82
10	28.54	28.44	28.79	28.74	28.74	28.54	28.64	28.43	28.75	28.49	24.79	24.94	24.49	24.69	24.58
11	28.75	28.56	29	28.95	28.95	28.88	28.98	28.77	29.09	28.82	25.05	25.19	24.75	24.95	24.84
12	29.9	30.15	30.15	30.05	30.15	29.87	29.97	29.76	30.08	29.81	27.09	27.24	26.84	27	26.88
13	28.36	28.46	28.61	28.56	28.56	29.38	29.48	29.27	29.59	29.32	25.9	26.04	25.60	25.80	25.69
14	26.40	26.50	26.65	26.60	26.54	28.39	28.49	28.28	28.60	28.33	23.71	23.85	23.41	23.61	23.50
15	24.27	24.45	24.52	24.03	24.47	27.98	28.08	27.87	28.19	27.92	21.35	21.49	21.05	21.25	21.14
16	19.06	18.98	19.31	19.26	19.15	24.65	24.75	24.54	24.86	24.59	19.06	19.21	18.76	18.96	18.85
17	18.78	18.88	19.03	18.9	18.98	21.57	21.67	21.46	21.78	21.51	17.14	17.28	16.84	17.04	16.93
18	18.50	18.35	18.67	18.70	18.70	19.69	19.79	19.58	19.90	19.64	15.87	16.01	15.57	15.77	15.66
19	16.98	16.68	17.05	17.18	17.18	18.09	18.19	17.98	18.30	18.04	14.9	15.04	14.60	14.80	14.69
20	15.87	15.97	16.01	16.07	16.07	17.80	17.90	17.69	18.01	17.74	13.74	13.98	13.46	13.66	13.55
21	14.55	14.65	14.45	14.75	14.75	17.03	17.13	16.92	17.24	16.97	13.16	13.30	12.86	13.06	12.95
22	14.09	14.19	14.15	14.29	14.30	16.65	16.75	16.54	16.86	16.59	12.29	12.33	11.93	12.13	12.02
23	12.98	13.08	13.23	13.18	13.18	16.40	16.50	16.29	16.61	16.34	11.99	12.13	11.69	11.89	11.78
24	13.55	13.65	13.8	13.75	13.75	16.68	16.78	16.57	16.89	16.62	12.06	12.20	11.76	11.96	11.85
Average	21.31	21.27	21.49	21.48	21.50	22.84	22.94	22.73	23.05	22.78	18.26	18.40	17.96	18.16	18.05
Standard Deviation	5.796	5.728	5.833	5.785	5.796	4.951	4.951	4.951	4.951	4.951	5.157	5.157	5.157	5.157	5.157
% Internal Uncertainty	4.244	4.248	4.226	4.227	4.225	4.100	4.091	4.110	4.081	4.105	4.585	4.567	4.623	4.597	4.612

(b)

Hour	Tambient (°C)					Solar Intensity (W/m ²)				
	Run 1	Run 2	Run 3	Run 4	Run 5	Run 1	Run 2	Run 3	Run 4	Run 5
1										
2	17.2	17.59	17.06	17.34	17.26	0	0	0	0	0
3	17.8	18.19	17.56	17.65	17.86	0	0	0	0	0
4	17.2	17.59	16.96	17.05	17.26	0	0	0	0	0
5	16.7	17.09	16.46	16.55	16.76	0	0	0	0	0
6	15.6	15.99	15.36	15.45	15.66	0	0	0	0	0
7	15	15.39	14.76	14.85	15.06	0	0	0	0	0
8	13.9	14.29	13.66	13.75	13.96	34.1	33.247	32.73	34.12	34.096
9	15.6	15.99	15.36	15.45	15.66	248	243.04	238.08	248.02	247.99
10	15	15.39	14.76	14.85	15.06	332.4	324.09	319.10	332.42	332.39
11	14.4	14.79	14.16	14.25	14.46	366.5	357.33	351.84	366.52	366.49
12	15	15.39	14.76	14.85	15.06	382.1	391.65	366.81	382.12	382.09
13	15	15.39	14.76	14.85	15.06	388.1	397.80	372.57	388.12	388.09
14	14.4	14.79	14.16	14.25	14.46	387.1	396.77	371.61	387.12	387.09
15	15	15.39	14.76	14.85	15.06	378.9	388.37	363.74	378.92	378.89
16	16.1	16.49	15.86	15.95	16.16	359.7	368.69	345.31	359.72	359.69
17	16.7	17.09	16.46	16.55	16.76	316.6	324.51	303.93	316.62	316.59
18	17.2	17.59	16.96	17.05	17.26	201.1	206.12	193.05	201.12	201.09
19	17.8	18.19	17.56	17.65	17.86	6	6.15	5.76	6.02	5.9963
20	17.8	18.19	17.56	17.65	17.86	0	0	0	0	0
21	18.3	18.69	18.06	18.15	18.36	0	0	0	0	0
22	18.3	18.69	18.06	18.15	18.36	0	0	0	0	0
23	18.3	18.69	18.06	18.15	18.36	0	0	0	0	0
24	18.3	18.69	18.06	18.15	18.36	0	0	0	0	0
Average	16.43	16.82	16.19	16.29	16.49	141.69	145.23	136.02	141.70	141.68
Standard Deviation	1.471	1.471	1.473	1.478	1.471	172.67	176.9	165.76	172.68	172.67
% Internal Uncertainty	4.833	4.777	4.869	4.853	4.825	1.646	1.687	1.680	1.646	1.646

On the other, the external uncertainty is mainly related to the measuring devices used during the experiment which can mainly affect the final accuracy of the results.

The measuring equipments used in the experiment are K- type thermocouples, infrared thermometer, pyranometer, anemometer, and OM-EL-USB-2 sensor for ambient temperature and humidity. The accuracy, range of reading and percent error values are represented in Table (5)

Table 5: Accuracy, range and % error of equipment

Instrument	Accuracy	Range	%Error
K- Type Thermocouple	± 0.5 °C	-200°C to +1250°C	± 1
Infrared Thermometer	± 0.1 °C	-30 to 500°C	± 1
Pyranometer	± 4 W/m ²	0 to 2000 W/ m ²	± 5
Anemometer	± 0.5 m/s	0 to 30.0 m/s	± 3
OM-EL-USB-2 Sensor	± 0.5 °C in temperature	-35 to +80°C	± 1
	± 3 % in relative humidity	0 to +100%RH	± 3.5

CHAPTER V

PARAMETRIC STUDY

A parametric study was conducted to assess the effect of the main factors affecting the solar still performance: roughness of the drum, angular velocity of the drum, and contact angle at which water is withdrawn from the solar still. This work is the first to introduce a drum characterized by a rough surface to a solar still which led to significant enhancement of the performance of solar stills studied in literature as demonstrated in the experimental section. In order to propose effective operational conditions, parametric and optimization studies were conducted to assess the effect of surface roughness, angular speed of the drum, contact angle between the drum and water, and drum's radius to length ratio and come up with optimal conditions with reduced energy consumption.

A. Effect of Surface Roughness

First from the derived model, surface roughness increases the driven flow rate. But this increase is not significant since the roughness effect is multiplied by the cube of the film thickness which is in the order of nanometers. On the other hand, the main contribution of roughness is to the increase of exposed area for heat and mass transfer. The test case used in model validation (period: typical day of June, solar still base area = 1 m², drum radius = 30 cm, drum length = 140 cm corresponding to a drum's radius to length ratios = 0.214, contact angle = 170°, drum rotational speed = 0.25 rpm) was considered with different roughness ratios. Figures (43) and (44) represent respectively the variation with time (Hour 0 corresponds to 12 noon) of temperature and water vapor

pressure difference between the drum and the glass cover for variable roughness ratios. It is observed that temperature and water vapor pressure difference between the drum and glass' cover increased with roughness ratio leading to higher potential for heat and mass transfer (Figure (43), Figure (44)). This explains the increase of hourly and total productivity of solar still with roughness ratio as shown in Figures (45) and (46) which illustrate the effect of roughness ratio on solar still hourly and total productivity respectively. It is clear that roughness largely enhances the solar still performance leading to significant increase in productivity. Peak in total solar still productivity at nearly 6 p.m. (Fig. 45) corresponds to a compromise between peak potential of heat and mass transfer.

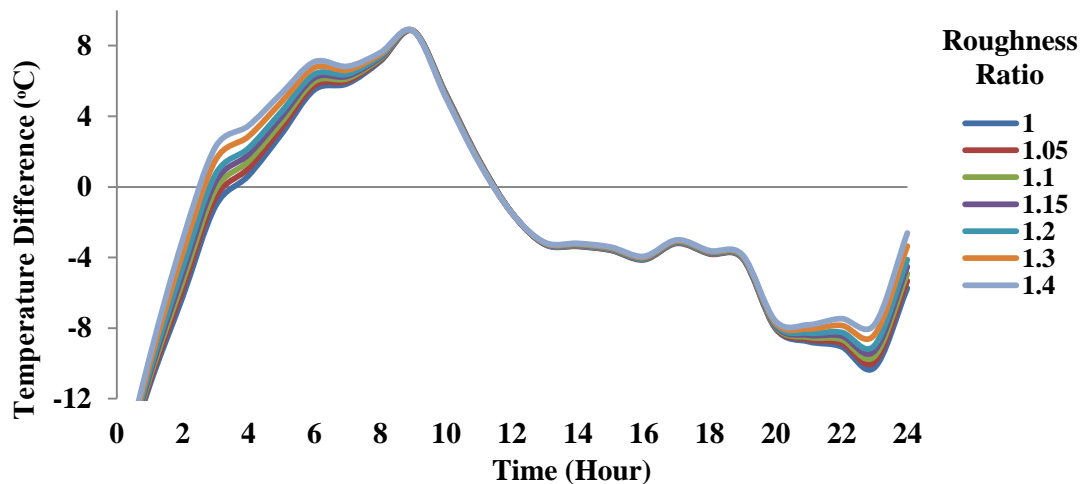


Figure 43: Variation with time of temperature difference between the drum and the glass cover for variable roughness ratios

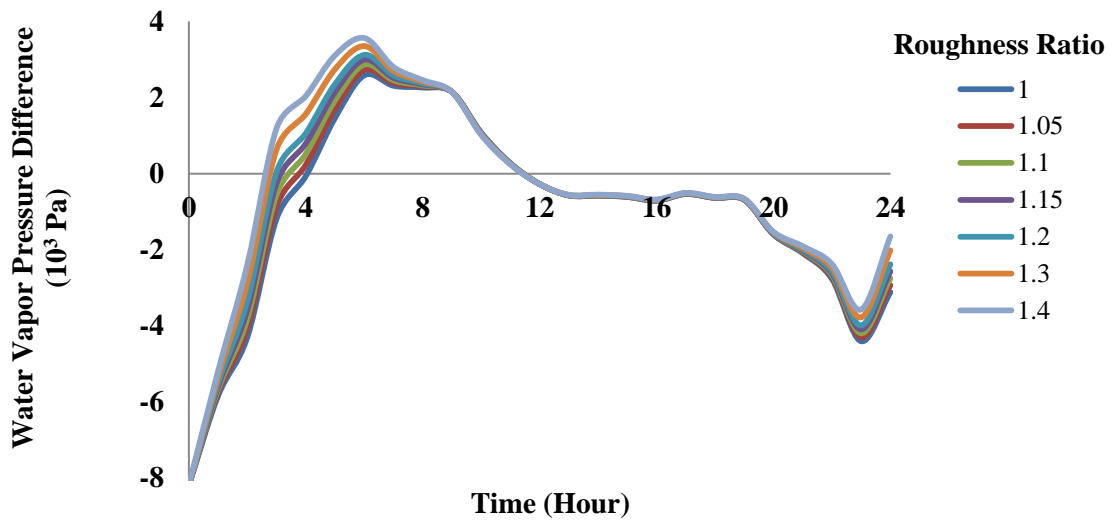


Figure 44: Variation with time of water vapor pressure difference between the drum and the glass cover for variable roughness ratios

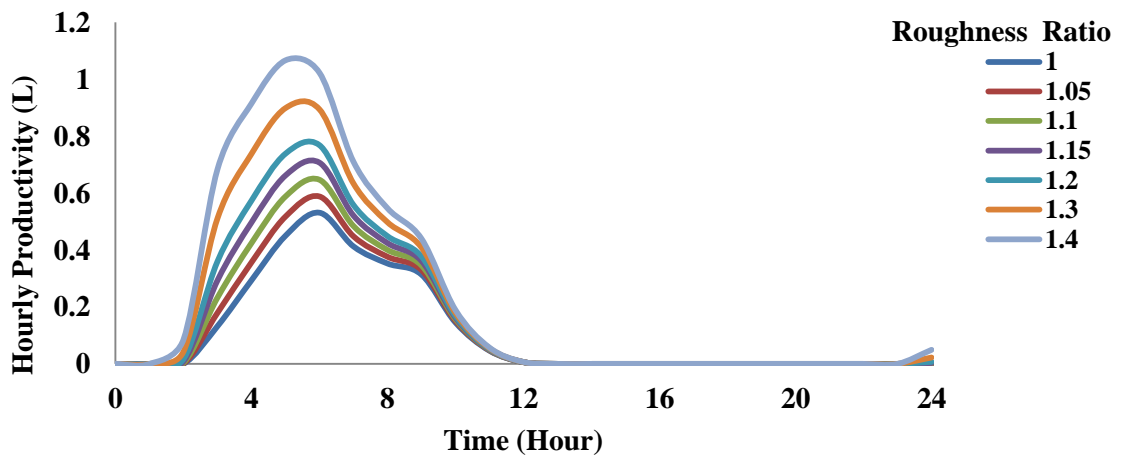


Figure 45: Variation with time of hourly productivity of the solar still for variable roughness ratios

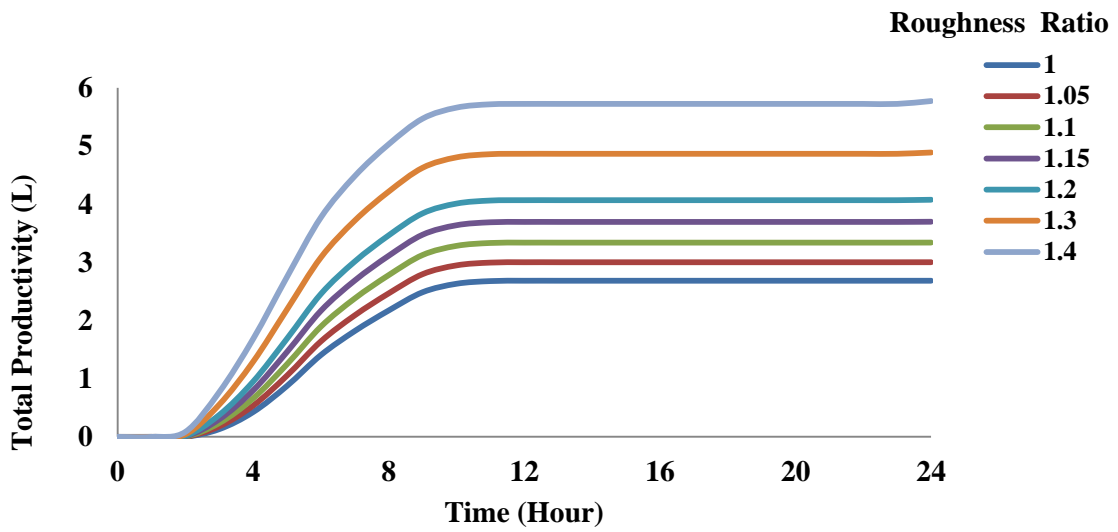


Figure 46: Variation with time of total productivity of the solar still for variable roughness ratios

B. Effect of Angular Speed

Higher the speed of rotation, lower is the time provided for heat and moisture exchange but higher is the driven flow rate. For this reason, for each set of conditions there is an optimal rotation angular velocity. To illustrate this, angular velocity was varied for the following set of conditions: period: typical day of June, solar still base area = 1 m^2 , drum radius = 30 cm, drum length = 140 cm corresponding to a drum's radius to length ratios = 0.214, contact angle = 170° , roughness ratio= 1. Figures (47) and (48) represent respectively variation with time (Hour 0 corresponds to 12 noon) of temperature and water vapor pressure difference between the drum and the glass cover for variable angular speeds. It is shown that temperature and water vapor pressure difference between the drum and glass' cover decreased with angular speed, leading to lower potential for heat and mass transfer (Figures (47) and (48)) since the exposure time is lower. This explains the increase of hourly and total productivity of solar still with angular speed decrease from 0.25 to 0.08 rpm as shown in Figures (49) and (50).

On the other hand, for angular speed lower than 0.08 rpm the rate of increase of productivity for first few hours is higher due to increased potential for heat and mass transfer but vanish for the remaining time. This observation is mainly because quantity of water is not enough due to decreased flow rate. Therefore, for the studied case, the optimal angular velocity is 0.08 rpm. For lower speed of rotation the driven water from the solar still is not enough, reducing the productivity of the solar still. On the other hand, for higher speed of rotation, the mass flow rate of water is more than needed but no enough time is provided for water evaporation, decreasing by that the solar still productivity.

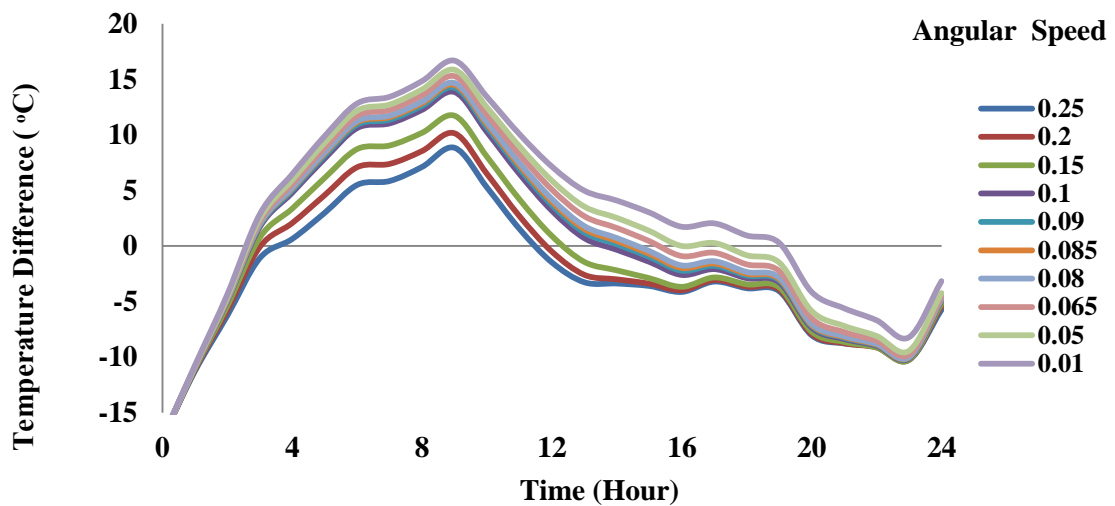


Figure 47: Variation with time of temperature difference between the drum and the glass cover for variable angular speeds

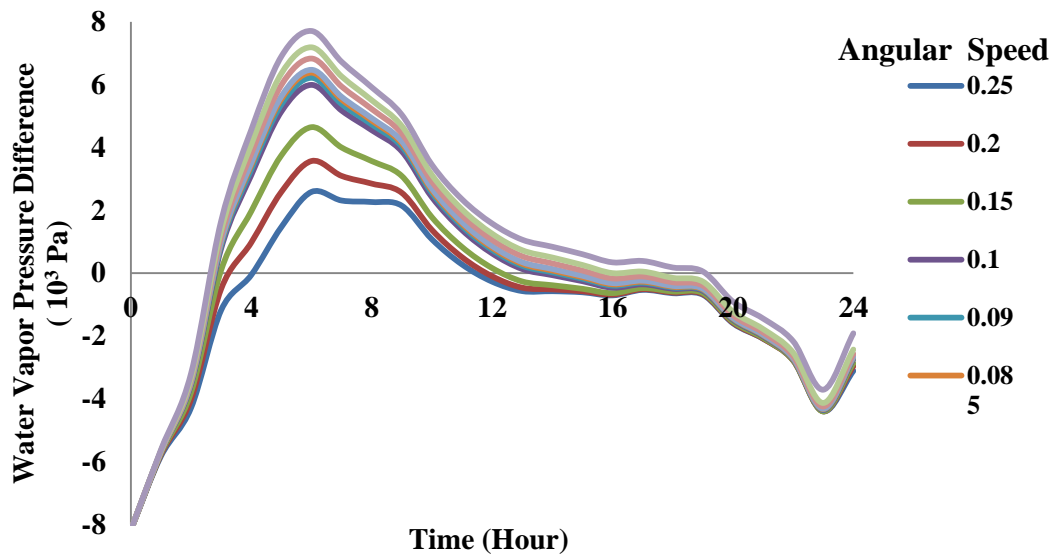


Figure 48: Variation with time of water vapor pressure difference between the drum and the glass cover for variable angular speeds

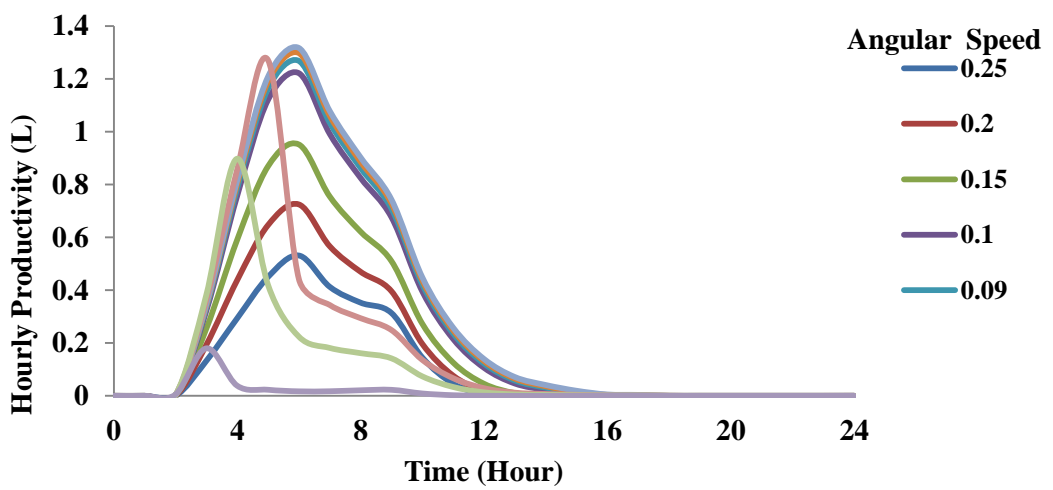


Figure 49: Variation with time of hourly productivity for variable angular speeds

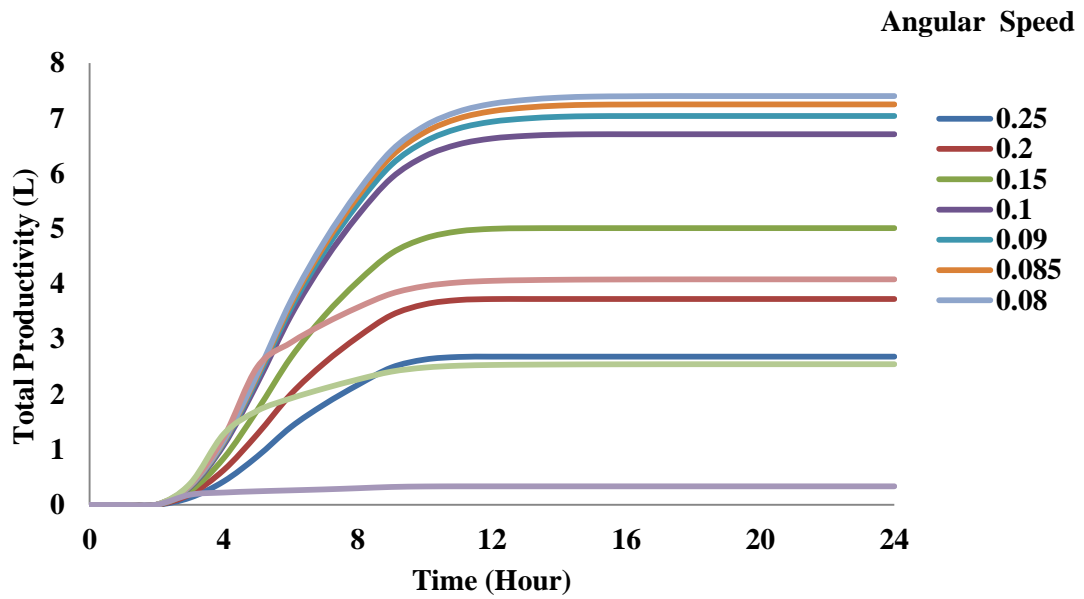


Figure 50: Variation with time of total productivity for variable angular speeds

C. Effect of Contact Angle

The level of water in the solar still affects the contact angle at which water is driven by the rotating drum (Figure (20)). By decreasing the water level, the contact angle is higher, leading to decreased driven flow rate but increased portion of the drum outside water. These two factors have opposing effects on the still performance. To investigate this, contact angle was varied for the following set of conditions: period: typical day of June, solar still base area = 1 m², drum radius = 30 cm, drum length = 140 cm corresponding to a drum's radius to length ratios = 0.214, roughness ratio= 1, drum rotational speed = 0.08 rpm). Figures (51) and (52) represent respectively variation with time (Hour 0 corresponds to 12 noon) of temperature and water vapor pressure difference between the drum and the glass cover for variable contact angles. It is shown that average temperature and water vapor pressure difference between the drum and glass' cover increased with contact angle leading to higher potential for heat and mass

transfer (Figures (53) and (54) since the exposed area of the drum outside water is higher. This explains increase of hourly and total productivity of solar still with contact angle increase from 150° to 170° as shown in Figures (53) and (54). On the other hand, for contact angle higher than 170° the rate of increase of productivity for first few hours is higher due to increased potential for heat and mass transfer but vanish for the remaining time. This observation is mainly because quantity of water is not enough due to decreased flow rate. Therefore, for the studied case, the optimal contact angle is 170° . Hence, we conclude that we can talk about optimal couples of angular speed and contact angle. For the set of conditions: drum radius = 30 cm, roughness ratio= 1, period: typical day of June one of the optimal couples is (0.08 rpm; 170°).

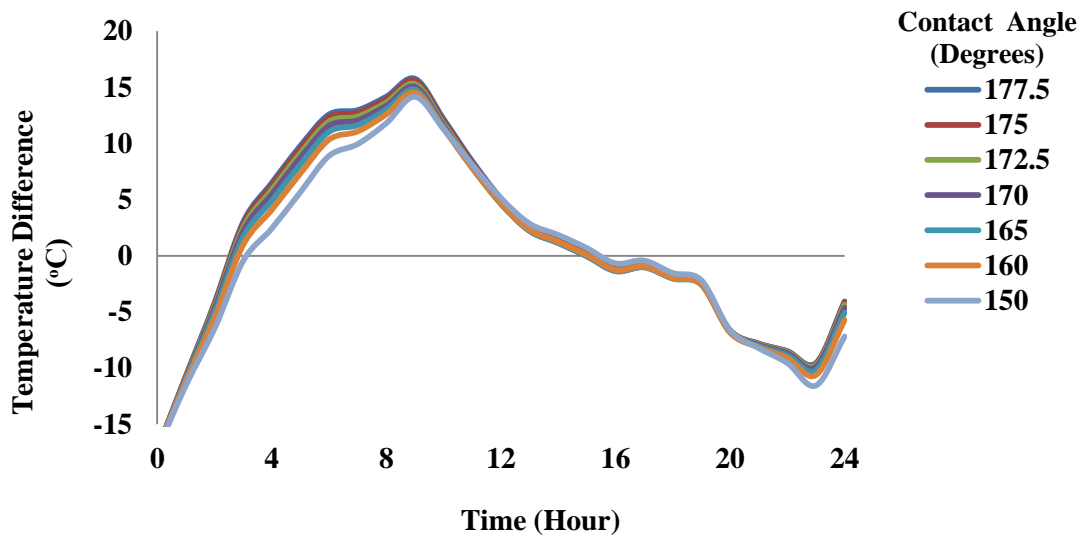


Figure 51: Variation with time of temperature difference between the drum and the glass cover for variable contact angles.

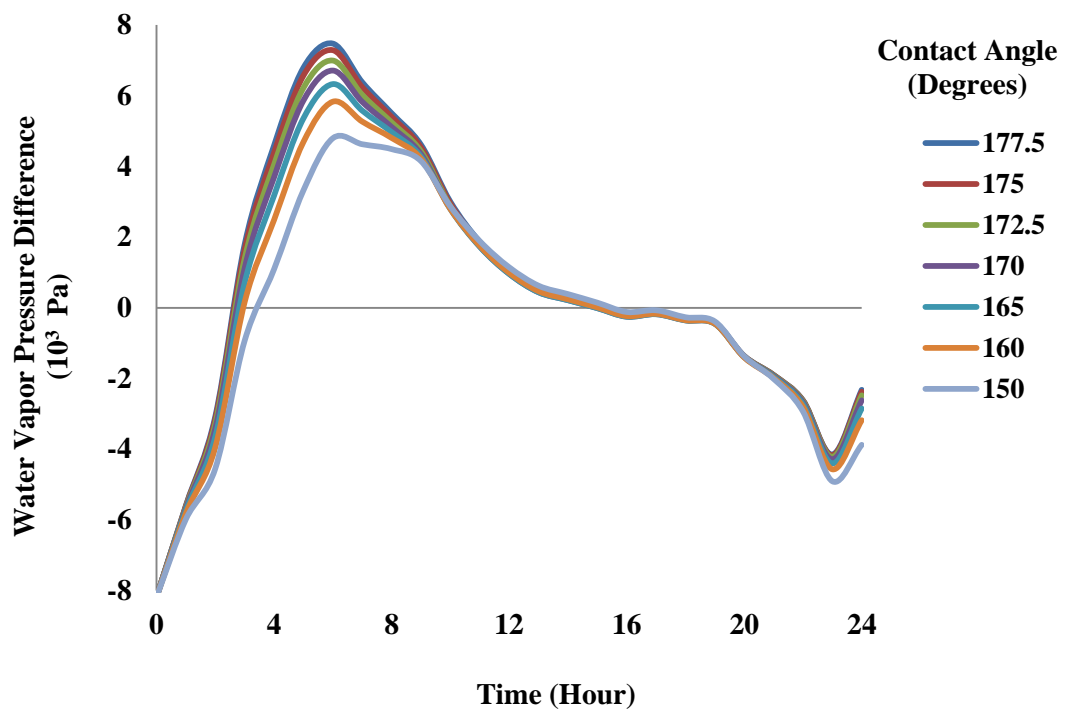


Figure 52: Variation with time of water vapor difference between the drum and the glass cover for variable contact angles.

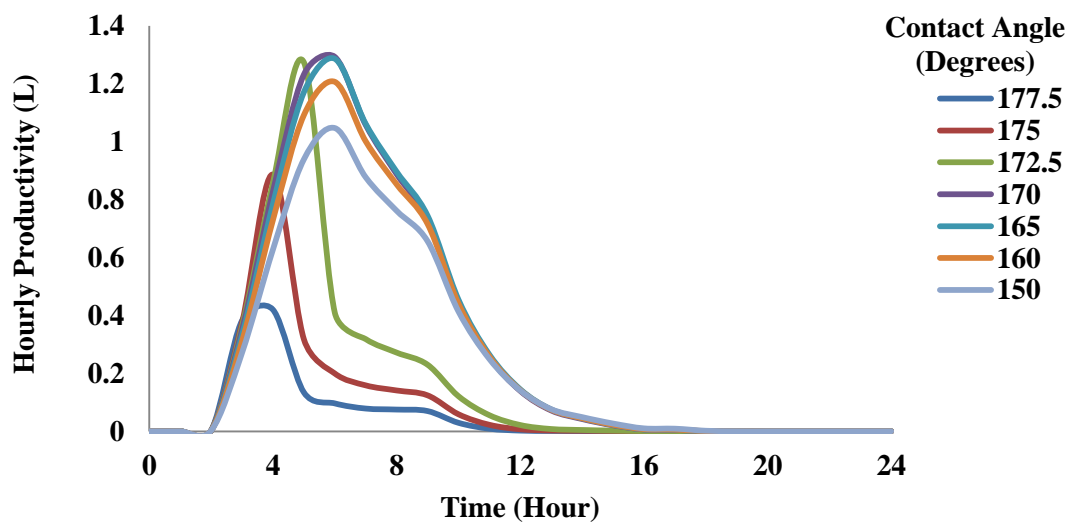


Figure 53: Variation with time of hourly productivity for variable contact angles.

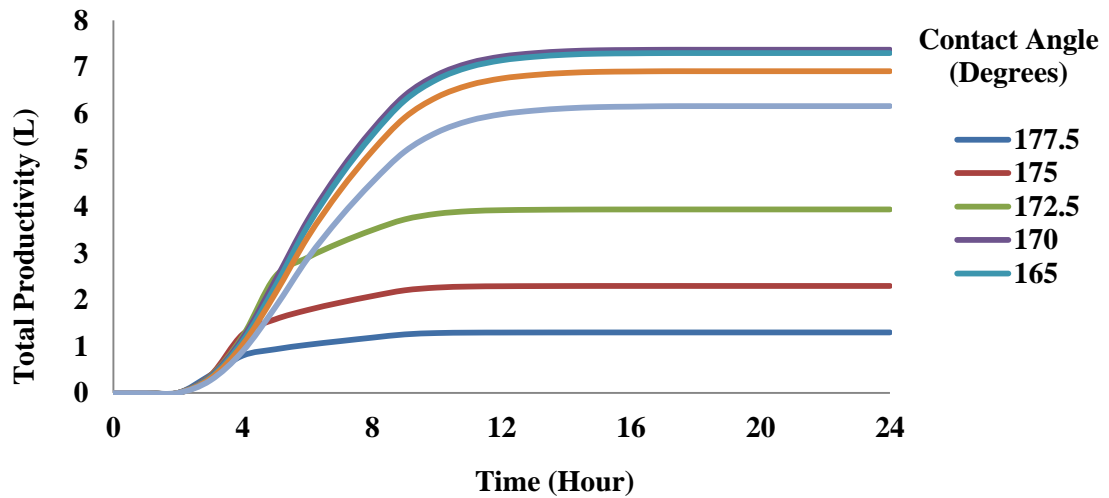


Figure 54: Variation with time of total productivity for variable contact angles.

D. Effect of Drum's Radius to Length Ratio

For the same peripheral area of the drum and solar still base area, the drum's radius to length ratio can be varied. Increasing this ratio presents a potential for improvement of still performance due to the fact that conductive and convective transfer processes take place over a larger circular circumference length. On the other hand, for the same angular velocity and therefore same exposure time for one drum rotation, radius increase leads to higher velocity at which water is driven by the rotating drum which presents opposing effects on still performance. The positive effect is the increase of driven flow rate of water available for evaporation and enhanced convective transfer while the negative one is the increase of linear velocity that might not provide enough time for the heat and mass transfer. From here the drum's radius to length ratio can be optimized. To inspect this issue, the drum's radius to length ratio was varied for the following set of conditions: period: typical day of June, solar still base area = 1 m², roughness ratio= 1, drum rotational speed = 0.08 rpm. Figures (55) and (56) represent respectively variation with time (Hour 0 corresponds to 12 noon) of average drum

temperature and average difference between the drum and the glass cover for variable drum's radius to length ratios. It is shown that average drum temperature and temperature difference between the drum and glass' cover increased with radius to length ratio leading to higher potential for heat and mass transfer for drum's radius to length ratio increase from 0.214 to 24.5. In fact, length increases between the two drum elements entering and leaving water leading to higher variation in drum temperature and thus higher average drum temperature and better heat and mass transfer. This explains the increase of hourly and total productivity of solar still with drum's radius to length ratios from 0.214 to 24.5 as shown in Figures (57) and (58). On the other hand, for drum's radius to length ratio higher than 24.5, the negative effect of linear velocity increase becomes dominant hindering heat and mass transfer processes, leading to delay in increase of average drum temperature and therefore delay in increase of solar still productivity (Figures (57) and (58)). But it is to be noted that the increase of radius to length ratio for the same solar still base area lead to significant increase of the volume due to increased height resulting from higher drum diameter. A ratio of 24.5 corresponds to a radius of 3.25 m which is not practical due to space constraints. For this reason, the optimization study will be limited for ratios below 2 corresponding to a maximum drum radius of 0.95 m.

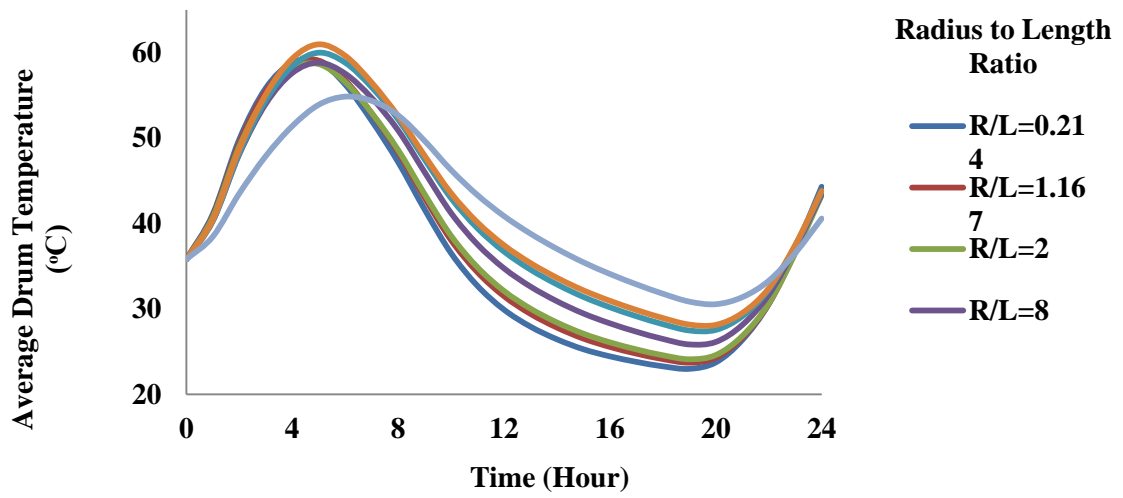


Figure 55: Variation with time of average drum temperature for variable drum's radius to length ratios.

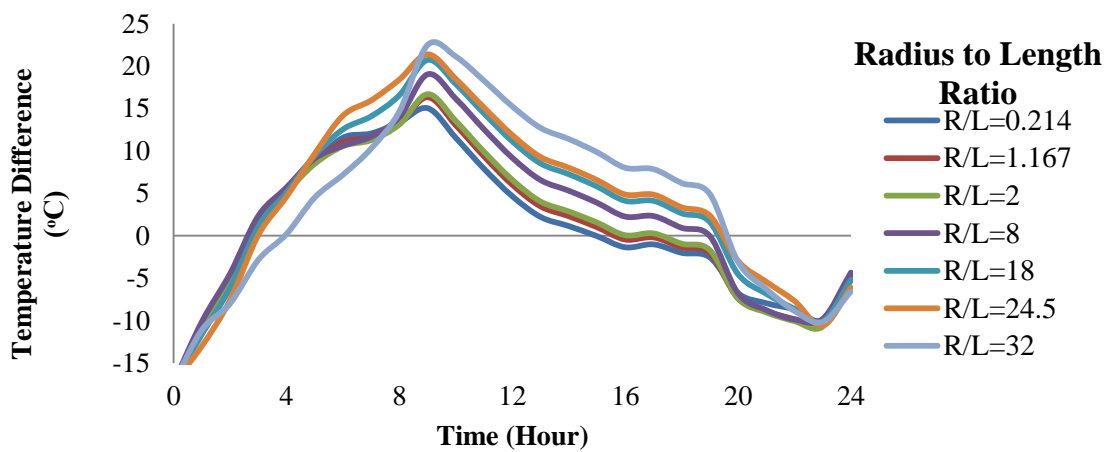


Figure 56: Variation with time of temperature difference between the drum and the glass cover for variable drum's radius to length ratios.

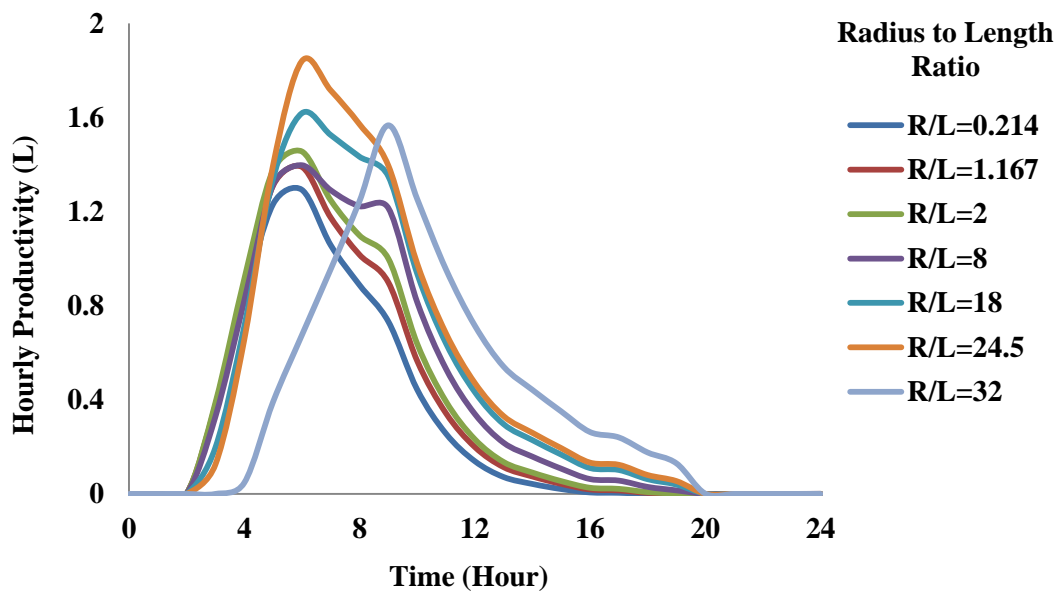


Figure 57: Variation with time of hourly productivity for variable drum's radius to length ratios.

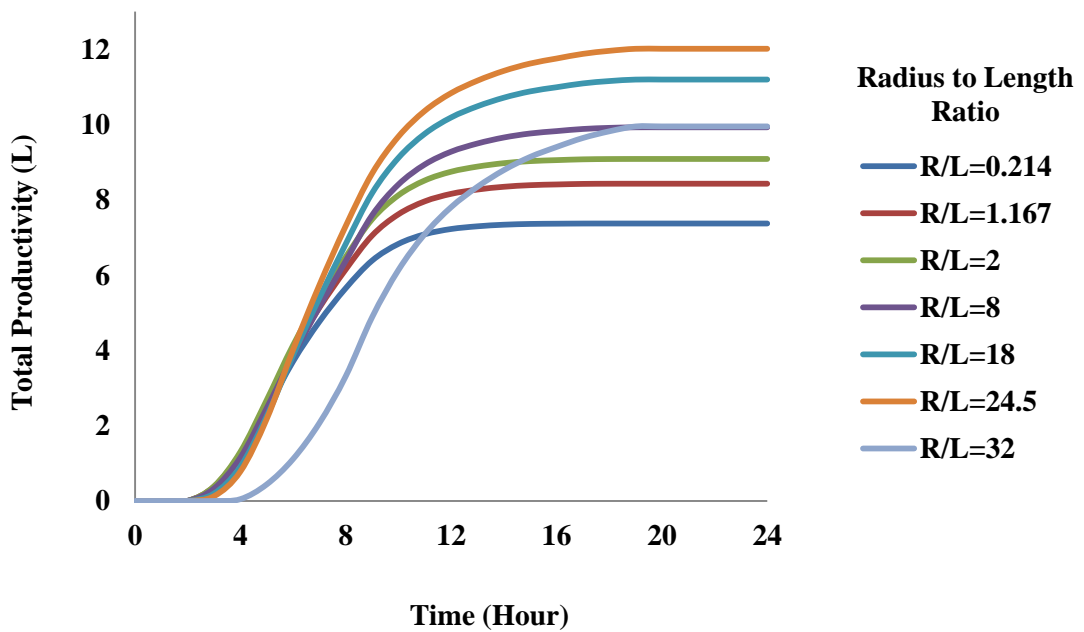


Figure 58: Variation with time of total productivity for variable drum's radius to length ratios.

CHAPTER VI

OPTIMIZATION OF THE DESIGN PARAMETERS

The objective of the optimization study is to maximize the daily total yield production constituting the objective function. The optimization variables are the surface roughness, the angular speed, the contact angle and the drum's radius to length ratio. The Mesh Adapted Direct Search (MADS) algorithm, which is a direct search optimization method, was used since the objective function which is the daily total yield production is non-continuous. In fact, the variation of the objective function is computed by numerical techniques resulting in non-continuous values. Therefore, a direct search method was adopted in this work because it does not require any information about the gradient of the objective function. The selected algorithm searches a set of points around a current point, looking for a point where the value of the objective function is higher than the value at the current point. The parametric study has already shown that optimums of the objective function are obtained for variation of angular speed and contact angle, while the objective function represents an increased trend with surface roughness and drum's radius to length ratio. For this reason, the optimization study was conducted to determine optimal couples of angular speed and contact angle for different surface roughness and drum's radius to length ratio.

As demonstrated in the previous analysis, there are optimal couples of angular speed and contact angle. For each contact angle corresponds an optimal angular speed. Figure (52) shows the variation of the optimal angular speed with the contact angle for different roughness ratios. As shown in Figure (52), the optimum couples of contact angle and angular speed are independent of roughness ratio. This is explained by the

fact that the flow rate per unit length is not significantly affected by the roughness ratio as shown in Equation (55). For all roughness ratios, higher is the contact angle, lower is the driven flow rate which explains the increase of optimal angular speed. A significant increase of the optimal angular speed is observed for contact angles higher than 150 degrees which leads to higher operational cost. For the same angular speed, higher the roughness ratio, better is the productivity.

Once the optimal couples were determined, variation of productivity with these couples was illustrated for variable roughness ratios as shown in Figure (59). It is observed that the optimum angle is independent of roughness ratio and is nearly 160 degrees (Figure (60)) which corresponds to the optimal couple (0.05 rpm; 160°) (Figure (59)). A good compromise between cost and productivity is a contact angle of 150 degrees (Figure (59)) which corresponds to the optimal couple (0.03 rpm; 150°) (Figure (59)). In fact, by increasing the rotation speed from 0.03 to 0.05 rpm, the energy input for rotation is increased by 66.67% while the productivity is nearly 6.5%.

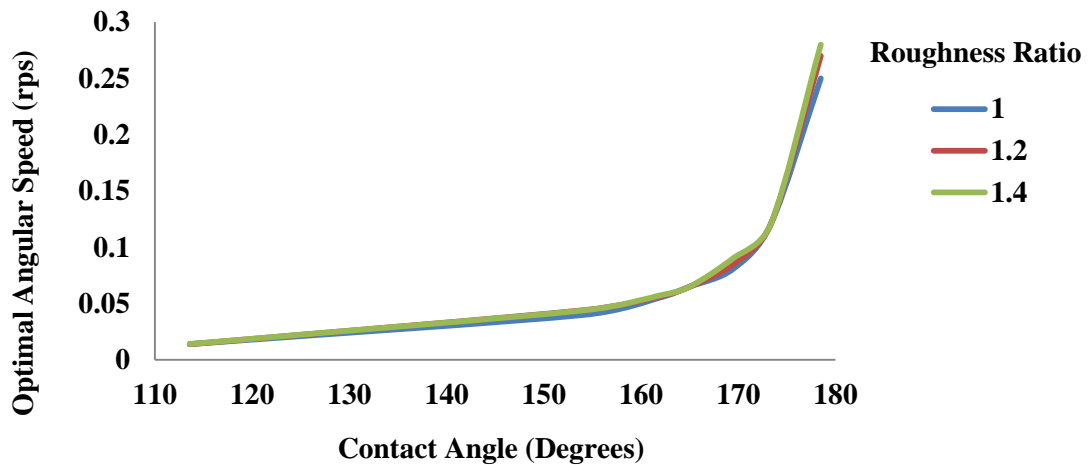


Figure 59: Optimization of the angular speed (using the MADS algorithm which is a direct search optimization method) for different contact angles and different roughness ratios

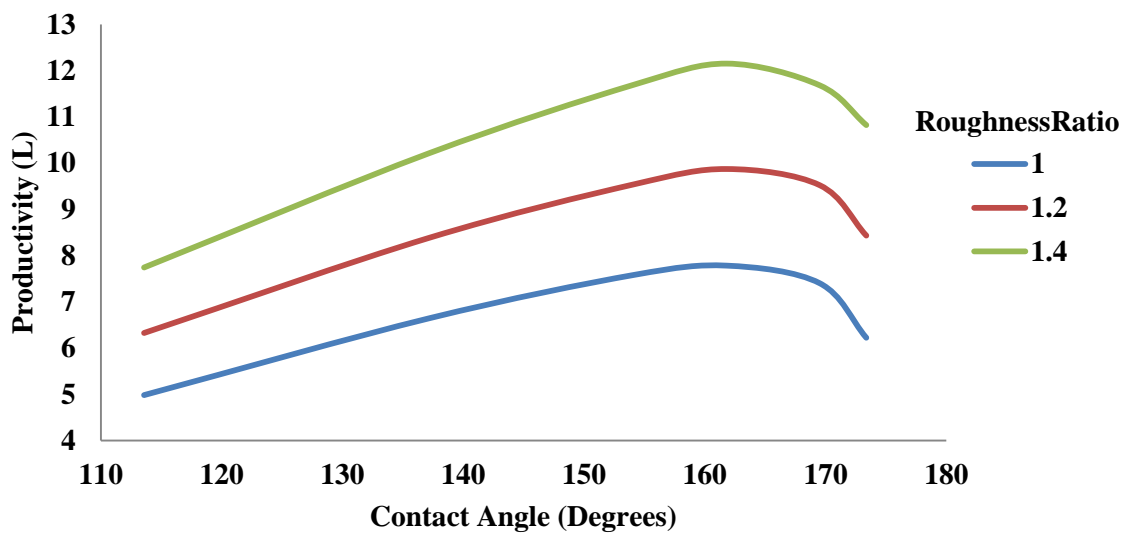


Figure 60: Variation of productivity (computed from Equation 5) with contact angle for variable roughness ratios for optimal angular speed

Higher the radius to length ratio, better is the performance of the solar still, but as mentioned previously, higher are the space constraints and the initial cost. Figure (61) represents the optimization of the angular speed for variable contact angles for different radius to length ratios, while Figure (62) illustrates variation of productivity

with contact angle for variable radius to length ratios for optimal angular speed. It is observed that for the same contact angle, higher is the radius to length ration, and lower is the optimal angular speed which saves energy (Figure (59)). Furthermore, the optimal couple for total productivity is characterized by the highest contact angle (Figure (60)). This is due to the fact that increased drum radius leads to significant increase in flow rate, which allows reaching optimal operation condition with lower angular speed and higher contact angle.

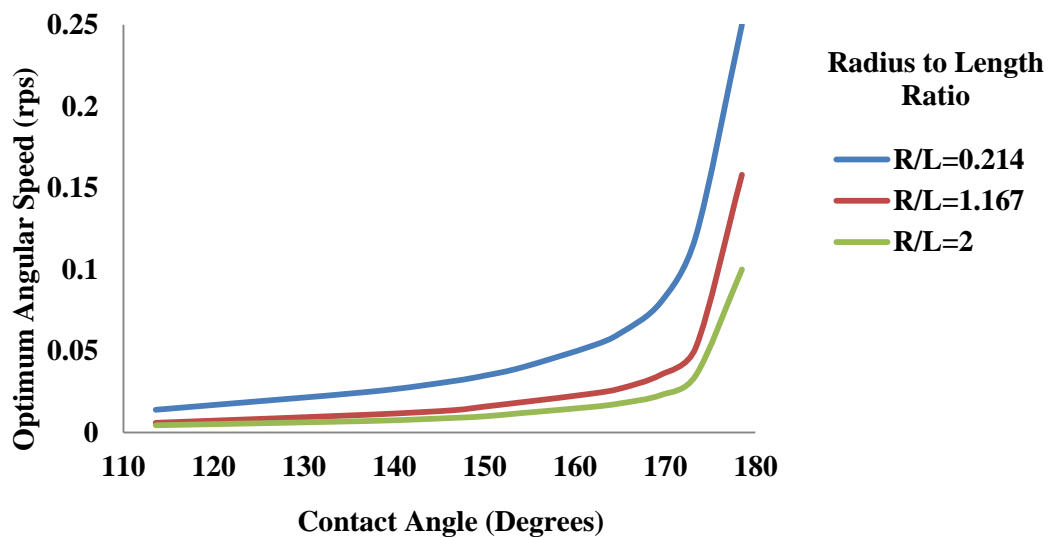


Figure 61: Optimization of the angular speed (using the MADS algorithm which is a direct search optimization method)for variable contact angles for different radius to length ratios

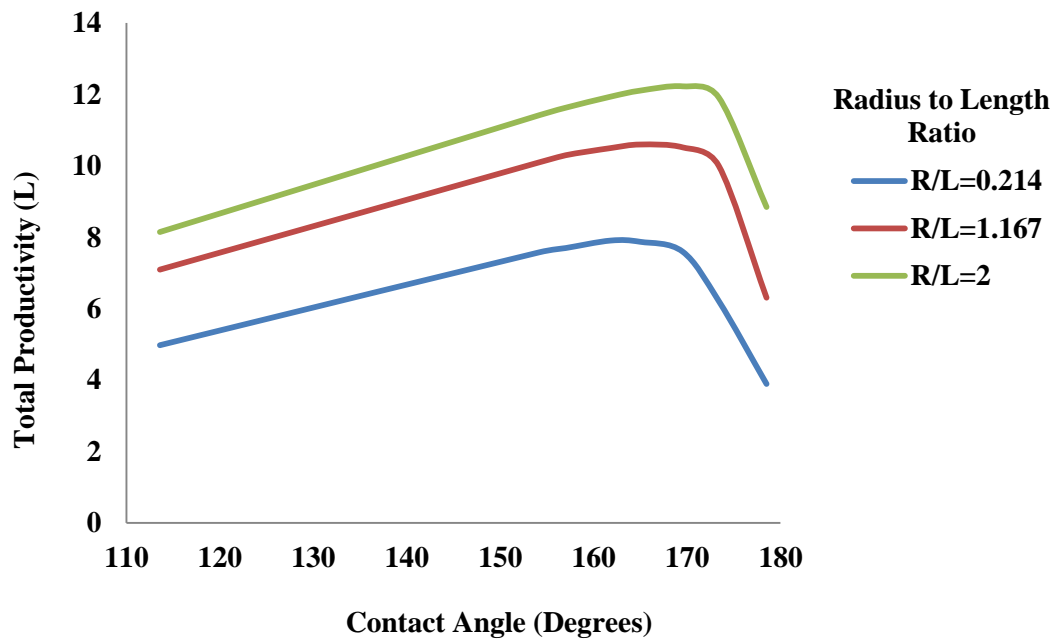


Figure 62: Variation of productivity (computed from Equation 5) with contact angle for variable radius to length ratios for optimal angular speed

CHAPTER VII

CONCLUSION

This work introduced for the first time a solar still assisted by a drum characterized by a rough surface. The roughness of the surface largely increased the water yield due to increased area that is exposed to water evaporation and enhanced heat and mass transfer.

A simplified model was developed to study the effect of roughness on the formation of the film thickness over a rotating drum assisting a solar still and the resulting driven flow rate by the rotating drum. Heat and mass transfer processes between the components of the solar system were considered by solving heat and mass balance equations computing temperatures of the system components and water evaporation rates. Literature experimental data were used for validation of the simplified model and good agreement was obtained with a relative error of the order of 10%.

In addition, the developed model was validated experimentally, where also good agreement was found between modeled and experimental data, where a maximum of 10% error was obtained between the modeled and experimental results. An enhancement value of 78% was found upon increasing the roughness ratio from 1 in the case of smooth surface to 2.2 in the case of rough surface. Meanwhile an enhancement of 198% was obtained when comparing a no drum system with a system with a smooth surface, and 431.1% when comparing a no drum system to a solar still system with a rough drum. .

The validated model was used to conduct a parametric study investigating the main factors affecting the solar still productivity. It was shown that increased roughness ratio enhances heat and mass transfer leading to increase of hourly and total productivity of solar still. Higher the speed of rotation, lower is the time provided for heat and moisture exchange but higher is the driven flow rate. Hence, for each set of conditions there is an optimal angular speed. Furthermore, lower the water level, the contact angle is higher leading to decreased driven flow rate but increased portion of the drum outside water. In addition, the drum's radius to length ratio presents a potential for improvement of still performance due to the fact that conductive and convective transfer processes take place over a larger circular circumference length but linear velocity increased which requires optimization.

For all roughness ratios, higher is the contact angle lower is the driven flow rate which explains the increase of optimal angular speed. A significant increase of the optimal angular speed is observed for contact angles higher than 150 degrees which leads to higher operational cost for variable roughness ratios. For the same angular speed, higher the roughness ratio better is the productivity. It was found that a good compromise between cost and productivity is a contact angle of 150 degrees which corresponds to the optimal couple (0.03 rpm; 150°). In fact, by increasing the rotation speed from 0.03 to 0.05 rpm the energy input for rotation is increased by 66.67% while the productivity is nearly 6.5%. Finally, for the same contact angle, higher is the radius to length ration lower is the optimal angular speed which saves energy.

It should be noted that for future work, it is worth to investigate along with the rough rotating drums, different cover shapes along with different weather conditions, and investigate extensively how forced convection (related to induced air speed over the

covers) can enhance the productivity of the systems. Also, many modifications investigated in literature can be coupled with this system, like using PCMs to enhance thermal storage.

BIBLIOGRAPHY

1. Gao CJ, Chen GH. Handbook for desalination technology and engineering. China. s.l. : Chemical Industry Press, 2004. p. 1.
2. Solar thermal utilization. ZN., He. 2009, Press of University of Science and Technology of China, Vol. 404, pp. 48–52.
3. An overview of solar desalination for domestic and agriculture water needs in remote arid areas. Chaibi, M.T. 2, s.l. : Desalination, 2000, Vol. 127, pp. 119-133.
4. The effects of design parameters on productivity performance of a solar still for seawater desalination: A review. Desalination. Abujazar, M.S.S., et al. s.l. : Desalination, 2016. 385, Vol. 385, pp. 178-193.
5. Developments in Solar Still Desalination Systems: A Critical Review. . Ayoub, G.M. and L. Malaeb. 19, s.l. : Critical Reviews in Environmental Science and Technology, 2012, Vol. 42, pp. 2078-2112.
6. Improving the performance of solar desalination systems. Abdel-Rehim, Z.S. and A. Lasheen. 13, s.l. : Renewable Energy, 2005, Vol. 30, pp. 1955-1971.
7. Sharshir, S.W., et al., Factors affecting solar stills productivity and improvement techniques: A detailed review. Sharshir, S.W., et al. s.l. : Applied Thermal Engineering, 2016, Vol. 100.
8. http://eponline.com/Forms/Search-Results.aspx?query=desalination&collection=EP_Web. [Online]

9. A review on solar stills for brine desalination. Gang Xiao, Xihui Wang, Mingjiang Ni, Fei Wang, Weijun Zhu, Zhongyang Luo, Kefa Cen. 2013 , Applied Energy, Vol. 103, pp. 642–652.
10. Mortada, Adel. Mediterranean Solar (hot) Spot, Preparation Phase, Lebanon Fact Sheet. WWF, for a Living Planet. Beirut : s.n., 2011. pp. 1-40.
11. Optimization of number of collectors for integrated PV/T hybrid active solar still. . Gaur MK, Tiwari GN. 2010, Applied Energy, Vol. 87, pp. 1763–1772.
12. Life cycle cost analysis of single slope hybrid (PV/T) active solar still. Kumar S, Tiwari GN. s.l. : Applied Energy, 2009, Vol. 86, pp. 1995–2004.
13. Parameters influencing the productivity of solar stills – A review. . Prakash, P. and V. Velmurugan. s.l. : Renewable and Sustainable Energy Reviews, 2015, Vol. 49, pp. 585-609.
14. Modeling of a modified solar still system with enhanced productivity. . Malaeb, L., K. Aboughali, and G.M. Ayoub. 2016, Solar Energy, Vol. 125, pp. 360-372.
15. Application of alternative energy integration technology in seawater desalination. . He, T.-x. and L.-j. Yan. 1, 2009, Desalination, Vol. 249, pp. 104-108.
16. Experimental study of a basin type solar still with internal and external reflectors in winter. H, Tanaka. s.l. : Desalination, 2009, Vol. 249, pp. 30–4.
17. Theoretical analysis of a basin type solar still with internal and external reflectors. Tanaka H, Nakatake Y. 2006, Desalination, Vol. 197, pp. 205–16.
18. Improvement of the tilted wick solar still by using a flat plate collector. Tanaka H, Nakatake Y. 2007, Desalination, Vol. 216, pp. 139-46.

19. Effect of water depths on heat and mass transfer in a passive solar still in summer climatic condition. Tiwari AK, Tiwari GN. 2006, *Desalination*, Vol. 195, pp. 78-94.
20. Performance study of the inverted absorber solar still with water depth and total dissolved solid. Dev R, Abdul-Wahab SA, Tiwari GN. 2011, *Applied Energy*, Vol. 88, pp. 252-64.
21. Experimental study on conventional solar still integrated with inclined solar still under different water depth. . Abd Elnaby Kabeel, Yazan Taamneh, Ravishankar Sathyamurthy, Padmanabhan Naveen Kumar, Athikesavan Muthu Manokar, Thirugnanasambantham Arunkumar. 2019, Vol. 48, pp. 100-114.
22. Comparative study of an inclined solar panel basin solar still in passive and active mode. . Manokar, A., et al. 2018, Vol. 169, pp. 206-216.
23. A solar still augmented with flat pate collector. Badran AA, Al-Hallaq AA, Eyal Salman IA, Odat MZ. 2005, *Desalination*, Vol. 172, pp. 227-34.
24. Analysis of double effect active solar distillation. Prasad B, Tiwari GN. 1996, *Energy Conversion and Management*, Vol. 37, pp. 1647-56.
25. Tilted wick solar still with flat plate bottom reflector. H., Tanaka. 2011, *Desalination*, Vol. 273, pp. 405–13.
26. Experimental investigation of a solar still coupled with solar collectors. Voropoulos K, Mathioulakis E, Belessiotis V. 2001, *Desalination*, Vol. 138, pp. 103-10.
27. Numerical study of a passive solar still with separate condenser. Madhlopa A, Johnstone C. 2009, *Renewable Energy*, Vol. 34, pp. 1668-77.

28. A solar still with minimum inclination, coupled to an outside condenser. E1-Bahi A, Inan D. 1999, *Desalination*, Vol. 123, pp. 79-83.
29. Performance study on solar still with enhanced condensation. Kumar KV, Bai RK. 2008, *Desalination*, Vol. 230, pp. 51-61.
30. Software to analyze solar stills and an experimental study on the effects of the cover. Ghoneyem A, Ileri A. 1997, *Desalination*, Vol. 114, pp. 37-44.
31. Effect of condensing cover material on yield of an active solar still: an experimental validation. Dimri V, Sarkar B, Singh U, Tiwari GN. 2008, *Desalination*, Vol. 227, pp. 178-89.
32. Enhanced solar still performance using water film cooling of the glass cover. AK., Abu-Hijleh Bassam. 1996, *Desalination*, Vol. 107, pp. 235-44.
33. Utilization of a forced condensing technique in a moving film inclined solar desalination still. NHA., Rahim. 1995, *Desalination*, Vol. 101, pp. 255-62.
34. Single basin solar still with fin for enhancing productivity. Velmurugan V, Gopalakrishnan M, Raghu R, Sritha K. 2008, *Energy Conversion and Management*, Vol. 49, pp. 2602-8.
35. Desalination of effluent using fin type solar still. Velmurugan V, Deenadayalan CK, Vinod H, Srithar K. 2008, *Energy*, Vol. 33, pp. 1719-27.
36. Experimental study of a solar still with sponge cubes in basin. Abu-Hijleh Bassam AK, Himzeh MR. 2003, *Energy Conversion and Management*, Vol. 44, pp. 1411-8.

37. Enhancement of solar still productivity using floating perforated black plate. Nafey AS, Abdelkader M, Abdelmotalip A, Mabrouk AA. 2002, *Energy Conversion and Management*, Vol. 43, pp. 937-46.
38. Performance of floating cum tilted wick typed solar still with the effect of water flowing over the glass cover. Janarthanan B, Chandrasekaran J, Kumar S. 2006, *Desalination*, Vol. 190, pp. 51-62.
39. Thermal modeling of a double condensing chamber solar still: an experimental validation. Aggarwal S, Tiwari GN. 1999, *Energy Conversion and Management*, Vol. 40, pp. 97-114.
40. Theory and experimental investigation of a weir-type inclined solar still. . Sadineni SB, Hurt R, Halford CK, Boehm RF. 2008, *Energy*, Vol. 33, pp. 71–80.
41. Effect of water flow rate on internal heat and mass transfer and daily productivity of a weir-type cascade solar still. Tabrizi FF, Dashtban M, Moghaddam H, Razzaghi K. 2010, *Desalination* , Vol. 160, pp. 239–47.
42. Performance of floating cum tilted wick typed solar still with the effect of water flowing over the glass cover. Janarthanan B, Chandrasekaran J, Kumar S. 2006, *Desalination*, Vol. 190, pp. 51-62.
43. A highly productive basin-type-multiple-effect coupled solar still. Tanaka H, Nosoko T, Nagata T. A. 2000, *Desalination*, Vol. 130, pp. 279-93.
44. A vertical multiple-effect diffusion-type solar still coupled with a heat-pipe solar collector. Tanaka H, Nakatake Y. 2004, *Desalination*, Vol. 160, pp. 195-205.

45. Indoor experiments of the vertical multiple effect diffusion-type solar still coupled with a heat-pipe solar collector. Tanaka H, Nakatake Y, Tanaka M. 2005, *Desalination*, Vol. 177, pp. 291-302.
46. Experimental study of vertical multiple-effect diffusion solar coupled with a flat plate reflector. H., Tanaka. 2009, *Desalination* , Vol. 249, pp. 34–40.
47. Parametric investigation of a double-effect solar still in comparison with a single-effect solar still. Al-Hinai, H., M.S. Al-Nassri, and B.A. Jubran. 1, 2002, *Desalination*, Vol. 150, pp. 75-83.
48. Solar thermal desalination system with heat recovery. Schwarzer K, Vieira ME, Faber C, Miiller C. 2001, *Desalination* , Vol. 137, pp. 23–9.
49. Low temperature desalination using solar collectors augmented by thermal energy storage. Gude VG, Nirmalakhandan N, Deng SG, Maganti A. 2012, *Appl Energy*, Vol. 91, pp. 466–74.
50. Experimental study of an integrated basin solar still with a sandy heat reservoir. Tabrizi FF, Sharak AZ. 2010, *Desalination*, Vol. 253, pp. 195-9.
51. Thermal performance of a single basin solar still with PCM as a storage medium. El-Sebaili AA, Al-Ghamdi AA, AL-Hazmi FS, Faidah AS. 2009, *Applied Energy*, Vol. 86, pp. 1187-95.
52. Thermal performance of a single-basin solar still integrated with a shallow solar pond. El-Sebaili AA, Ramadan MRI, Aboul-Enein S, Salem N. 2008, *Energy Conversion and Management*, Vol. 49, pp. 2839-48.

53. Effect of energy storage medium (black granite gravel) on the performance of a solar still. . Sakthivel, M. and S. Shanmugasundaram. 1, 2008, International Journal of Energy Research, Vol. 32, pp. 68-82.
54. Enhancement of modified solar still integrated with external condenser using nanofluids: An experimental approach. Kabeel, A.E., Z.M. Omara, and F.A. Essa. 2014, Kabeel, A.E., Z.M. Omara, and F.A. Essa, Enhancement of modified Energy Conversion and Management, Vol. 78, pp. 493-498.
55. Single basin double slope solar still with minimum basin depth and energy storing materials. Murugavel KK, Sivakumar S, Ahamed JR, Chockalingam KKSK, Srithar K. 2010, Applied Energy, Vol. 87, pp. 514-23.
56. Critical variables in the performance of a productivity-enhanced solar still. Ayoub, G., L. Malaeb, and P. Saikaly. 2013, Vol. 98.
57. The Effect of Cover Geometry on the Productivity of a Modified Solar Still Desalination Unit. Malaeb, L., G.M. Ayoub, and M. Al-Hindi. 2014, Energy Procedia, Vol. 50, pp. 406-413.
58. Solar Thermal Processes, in Seawater Desalination: Conventional and Renewable Energ Processes. Chaibi, M.T. and A.M. El-Nashar. Berlin : s.n., 2009, Springer Berlin Heidelberg, pp. 131-163.
59. Performance Analysis of Solar Air Heater with Jet Impingement on Corrugated Absorber Plate. M.Aboghrara, A., et al. 2017, Vol. 10.
60. PHYSICS OF FLUID SPREADING ON ROUGH SURFACES. DRAGILA, K.M.H.A.M.I. 2008, INTERNATIONAL JOURNAL OF NUMERICAL ANALYSIS AND MODELING, Vol. 5, pp. 85-92.

61. Complete Wetting on Rough Surfaces: Statics. . Andelman, D., J.F. Joanny, and M.O. Robbins. 8, 1988, Europhysics Letters (EPL), Vol. 7, pp. 731-736.
62. Does surface roughness amplify wetting? Malijevský, A. 18, s.l. : The Journal of Chemical Physics, 2014, Vol. 141.
63. Influence of roughness on capillary forces between hydrophilic surfaces. . van Zwol, P.J., G. Palasantzas, and J.T.M. De Hosson. 3, s.l. : Physical Review E, 2008, Vol. 78.
64. Film thickness of free falling water flow on a large-scale ellipsoidal surface. Du, W.-F., et al. s.l. : Progress in Nuclear Energy, 2018, Vol. 105, pp. 1-7.
65. Theoretical model for the wetting of a rough surface. Hay, K.M., M.I. Dragila, and J. Liburdy. 2, 2008, Journal of Colloid and Interface Science, Vol. 325, pp. 472-477.
66. Theory of drag out of liquids on flat plates. TALLMADGE, D. A. WHITE and J. A. Oxford : Pergamon Press Ltd, 1965, Chemical Engineering Science, Vol. 20, pp. 33-37.
67. Thermophysical and transport properties of humid air at temperature range between 0 and 100°C . Tsilingiris, P.T. 5, 2008, Energy Conversion and Management, Vol. 49, pp. 1098-1110.
68. Fabrication of three-dimensional microstructures by soft molding. Y. S. Kim, K. Y. Suh, and Hong H. Lee. 2285, 2001, Applied Physics, Vol. 79.
69. Laser Texturing of Rolled Surfaces. HE Yunfeng, DU Dong, LIU Ying, SUI Bo, XIONG Lijuan. 1007-0214, Beijing : s.n., 2003, TSINGHUA SCIENCE AND TECHNOLOGY, Vol. 8, pp. 236-240. 2.
70. https://en.wikipedia.org/wiki/Abrasive_blasting. [Online]

71. Use of a blast coating process to promote adhesion between aluminium surfaces for the automotive industry. Joe Flanagan, Paul Schütze, Conor Dunne, Kenneth T Stanton, Barry Twomey. 16, s.l. : The Journal of Adhesion Science and Technology, February 2018, Vol. 33.
72. Surface Morphology and Wettability of Sandblasted PEEK and its Composites. R. OURAHMOUNE, M. Salvia, T.G. Mathia, N. Mesrati. s.l. : SCANNING, 2014, Vol. 36, pp. 64-75.
73. Pre-sintered Y-TZP sandblasting: effect on surface roughness, phase transformation, and Y-TZP/veneer bond strength. Carla Müller Ramos-Tonello, Bruno Freitas Trevizo, Raphaela Farias Rodrigues, Ana Paula Rodrigues Magalhães, Adilson Yoshio Furuse, Paulo Noronha Lisboa, Filho, Americo Sheitiro Tabata, and Ana Flávia Sanches Borges. 6, 2017, Journal of Applied Oral Science, Vol. 25, pp. 666-673.
74. Theoretical and experimental performance evaluation of single-slope single-basin solar still with multiple V-shaped floating wicks. Abhay Agrawal, R. S. Rana. 2019, Helion.
75. Wilson, A. Moisture Control in Buildings: Putting Building Science in Green Building. [Online] 2003.
<http://www.buildinggreen.com/auth/article.cfm/2003/7/1/Moisture-Control-in-Buildings-Putting-Building-Science-in-Green-Building/>.
76. Incropera, Dewitt and Bergman, Lavine. Fundamentals of Heat and Mass Transfer.
77. Parametric Study of a Packed Bed Dehumidification/Regenerator Using CaCl₂ Liquid Desiccant. Radhwan, A.M., Gari, H.N. and Elsayed, M.M. 1993, Renewable Energy, pp. 49-60.

78. Dougherty, Elizabeth. WHY DO WE SWEAT MORE IN HIGH HUMIDITY?
[Online] 2011. <http://engineering.mit.edu/ask/why-do-we-sweat-more-high-humidity>.
79. Use of desiccant dehumidification to improve energy utilization in air-conditioning systems in Beirut. Ghaddar, Nesreen, Ghali, Kamel and Najm, Antoine. 2004.
80. Moisture in Buildings. Straube, John. s.l. : ASHRAE Journal, 2002, ASHRAE Journal.
81. A computationally effective formulation of the thermodynamic properties of LiBr–H₂O solutions from 273 to 500 K over full composition range. Pa'tek*, J. and Klomfar, J. 2006.
82. Duffie, John A. and Beckman, William A. Solar Engineering and of Thermal Processes. s.l. : JOHN WILEY & SONS, INC.
83. A Preliminary Evaluation of Alternative Liquid Desiccants for a Hybrid Desiccant Air Conditioner. Studak, J. W. and Peterson, J. L. 1988. Proceedings of the Fifth Symposium on Improving Building Systems in Hot and Humid Climates.
84. HACH Water Analysis Handbook Procedures. 5th. 2008.
85. What's New in ASHRAE's Standard on Comfort. Turner, Stephen C. 2011, ASHRAE Journal.
86. Bradshaw, Vaugh. The Building Environment: Active and Passive Controls. Third. s.l. : John Wiley & Sons, Inc., 2006.
87. Causes and Effects of High Humidity in South Florida Schools. Morse, Roger G., Haas, Paul E. and Zehnter, Dean A. 2007. ASHRAE Building X International Conference.

88. Modeling of the effect of hygroscopic curtains on relative humidity for spaces air conditioned by DX split air conditioning system. Ghali, K., Katanani, O. and Al-Hindi, M. 2011, *Energy and Buildings*, Vol. 43, pp. 2093-2100.
89. Review Article: Passive Design for Thermal Comfort in Hot Humid Climates. Chenvidyakarn, Torwong. 2007, *Journal of Architectural/Planning Research and Studies*, Vol. 5.
90. Technical development of rotary desiccant dehumidification and air conditioning: A review. La, D., et al. 2010, *Renewable and Sustainable Energy Reviews*, Vol. 14, pp. 130-147.
91. Tests of a Novel Ceiling Panel for Maintaining Space Relative Humidity by Moisture Transfer from an Aqueous Salt Solution. Fauchoux, M.T., Simonson, C.J. and Torvi, D.A. 2009, *ASTM International*, Vol. 6.
92. Applicability of a heat and moisture transfer panel (HAMP) for maintaining space relative humidity in an office building using TRNSYS. Eldeeb, Radia, Fauchoux, Melanie and Simonson, Carey J. 2013, *Energy and Buildings*, Vol. 66, pp. 338-345.
93. Historical review of liquid desiccant evaporation cooling technology. Mohammad, Abdulrahman Th., et al. 2013, *Energy and Buildings*, Vol. 67, pp. 22-33.
94. Performance testing of a counter-cross-flow run-around membrane energy exchanger (RAMEE) system for HVAC applications. Mahmud, Khizir, et al. 2010, *Energy and Building*, Vol. 42, pp. 1139-1147.
95. Steady-state performance of a run-around membrane energy exchanger(RAMEE) for a range of outdoor air conditions. Hemingson, Howard B., Simonson, Carey J. and

- Besant, Robert W. 2011, *International Journal of Heat and Mass Transfer*, Vol. 54, pp. 1814-1824.
96. Optimized solar-powered liquid desiccant system to supply building fresh. Audah, N., Ghaddar, N. and Ghali, K. 2011, *Applied Energy*, Vol. 88, pp. 3726-3736.
97. Testing and modelling of a novel ceiling panel for maintaining space relative humidity by moisture transfer. Fauchoux, Melanie, et al. 2010, *International Journal of Heat and Mass Transfer*, Volume 53, Issues 19–20, Vol. 53, pp. 3961-3968.
98. Steady-State Performance of a Small-Scale Liquid-to-Air Membrane Energy Exchanger for Different Heat and Mass transfer Directions, and Liquid Desiccant Types and Concentrations: Experimental and Numerical Data. Moghaddam, Davood Ghadiri, et al. 2013, *Journal of Heat Transfer*, Vol. 135.
99. Experimental and theoretical analysis of air, humidification/dehumidification process using hydrophobic capillary contractors. Bergero, Stefano and Chiari, Anna. 2001, *Applied Thermal Engineering*, Vol. 21, pp. 1119-1135.
100. Effectiveness of heat and Mass transfer in packed beds of liquid desiccant system. Elsayed, M.M., Gari, H. N. and Radhwan, A.M. 1993, *Renewable Energy*, Vol. 3, pp. 661-668.
101. Study of an aqueous lithium chloride desiccant system: air dehumidification and desiccant regeneration. Fumo, Nelso and Goswami, D.Y. 2002, *Solar Energy*, Vol. 72, pp. 351-361.
102. Performance of a Run-Around system for HVAC Heat and Moisture Transfer Applications Using Cross-Flow Plate Exchangers Coupled with Aqueous Lithium

- Bromide. Fan, Haisheng, Carey j. Simonson, Robert W. Besant and Shang, Wei. 2, 2006, HVAC & R Research, Vol. 12, pp. 313-336.
103. Properties of aqueous solutions of lithium and calcium chloride: formulations for use in air conditioning equipment design. Conde, Manuel R. 2004, International Journal of Thermal Sciences, Vol. 43, pp. 367-382.
104. Larson, Michael David. The performance of membranes in a newly proposed runaround heat and moisture exchanger. 2006. Masters Thesis.
105. A numerical modeling approach to evaluate energy-efficient mechanical. Yassine, Bilal, et al. 2012, Energy and Buildings, Vol. 55, pp. 618-630.
106. Numerical studies for performance evaluation evaluation of a permeable ceiling panel for regulation of indoor humidity. Vashistha, Vaibhav and Talukdar, Prabal. 2013, Energy and Buildings, Vol. 62, pp. 158-165.
107. Modeling of a flat plate membrane-distillation system for liquid desiccant regeneration in air-conditioning applications. Rattner, Alexander S., et al. 2011, International Journal of Heat and Mass Transfer, Vol. 54, pp. 3650-3660.
108. Annual evaluation of energy, environmental and economic performances of a membrane liquid desiccant air conditioning system with/without ERV. Abdel-Salam, Ahmed H. and Simonson, Carey J. 2014, Applied Energy, Vol. 116, pp. 134-148.
109. Desalination in Middle East set to grow. Matthews, S. s.l. : H.U.M. East, 2009.
110. Advanced designs of solar desalination systems: A review. El-Sebaili, A.A. and E. El-Bialy. s.l. : Renewable and Sustainable Energy Reviews, 2015, Renewable and Sustainable Energy Reviews, Vol. 49, pp. 1198-1212.

111. Single basin solar still with fin for enhancing productivity. . Velmurugan, V., et al. 10, s.l. : Energy Conversion and Management, 2008, Vol. 49, pp. 2602-2608.
112. Çengel, Y.A. Thermodynamics : an engineering approach. . 6. Boston : : McGraw-Hill Higher Education, 2008.

